2015

Investigation on the Mechanical, Microstructural, and Electrical Properties of Graphene Oxide-Cement Composite

Baig Abdullah Al Muhit
University of Central Florida

STARS Citation

Al Muhit, Baig Abdullah, "Investigation on the Mechanical, Microstructural, and Electrical Properties of Graphene Oxide-Cement Composite" (2015). *Electronic Theses and Dissertations, 2004-2019*. 643.
https://stars.library.ucf.edu/etd/643

INVESTIGATION ON THE MECHANICAL, MICROSTRUCTURAL, AND ELECTRICAL PROPERTIES OF GRAPHENE OXIDE-CEMENT COMPOSITE

by

BAIG ABDULLAH AL MUHIT
B.S. Bangladesh University of Engineering & Technology, Bangladesh, 2007
M.S. University of Malaya, Malaysia, 2012

A thesis submitted in partial fulfillment of the requirements
for the degree of Master of Science
in the Department of Civil, Environmental, and Construction Engineering
in the College of Engineering and Computer Sciences
at the University of Central Florida
Orlando, Florida

Summer Term
2015

Major Professor: BooHyun Nam

ABSTRACT

Nanotechnology refers to the use of the materials or particles ranging from a few nanometers (nm) to 100 nanometers (nm) in a wide range of applications. Use of nanomaterials in cement composite to enhance the mechanical properties, fracture toughness and other functionalities has been studied for decades. In this regard, one of the carbon-based nanomaterials, Graphene Oxide (GO), has received attentions from researchers for its superior mechanical properties (e.g. tensile strength, yield strength, and Young's modulus). Although GO is not lucrative in increasing electrical conductivity (EC) of cement paste compared to that of graphene- another derivative of GO, reduced graphene oxide (rGO), might be a solution to increase EC. Another derivative of GO is the solution to the problem.

In this research, the compressive strength and flexural strength of GO-cement composite (GOCC) and rGO-cement composite (rGOCC) have been investigated with 0.01% and 0.05% GO and rGO content. GOCC-0.05% showed 27% increase in compressive strength compared to the control cement paste after 28 days (d) of hydration. GOCC-0.01% showed only 3.4% increase in compressive strength compared to the control. rGOCC-0.05% showed 21% increase in compressive strength and 15.5% increase in Modulus of Rupture (MOR) compared to the control cement paste after 28 d of hydration. On the other hand, rGOCC-0.01% showed 7% increase in compressive strength and 0.35% increase in MOR after 28 d. GOCC-0.05% showed increasing trends in compressive strength after 28 d indicating continuation of hydration. Similarly, rGOCC-0.05% also showed increasing trends in compressive and flexural strength after 28 d, possibly due to the reason described earlier.

Microstructural investigation on GOCC-0.05% and GOCC-0.01% by X-ray Diffraction (XRD) illustrated that the crystallite sizes of tobermorite-9Å and jennite, which are

mineralogical counterpart of disordered Calcium-Silicate-Hydrate (C-S-H), increases from 3 d to 28 d, representing the crystallite growth due to continued hydration. However, the crystallite size of GOCC-0.05% was smaller than that of GOCC-0.01% at both 3 d and 28 d, indicating finer nucleated grains. According to Hall-Petch equation, mechanical strength increases with decreasing particle size. Finer particles or grains can increase the strength in cement composites in several other ways: (1) GO acted as heterogeneous nucleation sites because of reactive functional groups. Activation energy was decreased by these “defects” in the cement paste, and consequently, numerous nuclei of C-S-H. with high surface area were formed, (2) because of finer grains, cracks are forced to move along a tortuous path, which makes the structure difficult to fail, and strength increased consequently (3) Finer grains of GOCC-0.05% created compacted hydration products decreasing porosity which can indirectly increase the strength. The above reasons, separately or in conjunction, might increase the strength of GOCC-0.05% and proved that GO is responsible for increasing heterogeneous nucleation sites during cement hydration.

Early age hydration (EAH) characteristics were investigated for rGOCC specimens with 0.1% and 0.5% rGO content. Scanning Electron Microscope (SEM), Energy Dispersive X-ray analysis (EDX), and X-ray Diffraction (XRD) were employed to study the EAH characteristics. SEM/EDX, and XRD analysis were performed after 15 min, 1 h, 3 h and 24 h of hydration. (EAH) study on rGOCC-0.1% showed that at 15 min hydration, numerous precipitates of, possibly, C-S-H formed along the grain boundary (GB) of unhydrated cement grains. This served as visual confirmation of Thomas and Scherer’s Boundary Nucleation and Growth (BNG) model that hydration of cement grains was initiated by the short burst of nucleation of C-S-H embryos along GB. EDX on rGOCC-0.1% and rGOCC-0.5% showed that Ca/Si ratio in C-S-H was ~2.0. This finding indicated that C-S-H structure in this study was concurrent with that of impure jennite. XRD analysis also evidently showed that jennite was present, possibly possessing a short range ordered (SRO) structure, referring to local crystalline structure in a very short area. After consulting Chen's work, it would be appropriate to say that C-S-H found in this study resembled more as C-S-H (II), which is disordered jennite. It was also observed that as expected with cement with nanomaterials, with continuing hydration, pore spaces were filled with hydration products such as C-S-H, ettringite, CH, sulfoaluminates etc,.

Lastly, Electrical resistivity (ER) testing on 9 sets of rGOCC specimens was conducted. The specimen includes 0.5%, 1%, 5% rGO content, and the control conditioned in both oven dry (OD) and saturated surface dry (SSD). ER increased with the increase of rGO content from 0.5% and 1% compared to that of the control. However, the ER of rGOCC-5% was significantly decreased, showing 93% reduction compared to the control, which can be interpreted as a threshold value for sensing applications to be explored. As expected, large reduction of ER value occurred on the specimens with the SSD condition. This reduction can be attributed to the ionic conduction though the pore solution of the composites. As the rGO content increased, so did the potential nucleation sites for hydration (as can be seen in SEM images), which might block the number of contact points among the rGO, resulting in low conduction and high resistivity. However, as rGO content increased to 5%, the contact areas/points increased to a degree that could trump the nucleation seeding sites, resulting in decreased ER. The ER measured with the rGOCC specimens was comparable to that of cement composites incorporating carbon fibers (CF), and steel fibers, but higher content of rGO are required to have a similar ER range of those fiber cement composites. This might be due to smaller sizes of rGO sheets and lower aspect ratio compared to other nanofibers causing drastic reduction of electron tunneling mechanism compared to other fibers.

Dedicated to Kazi Tasneem

ACKNOWLEDGMENTS

Firstly, I pay my deepest gratitude to Almighty Allah for His graciousness, benevolence and unlimited blessing upon me.

My sincere thanks go to my adviser Dr. BooHyun Nam, Assistant Professor, Department of Civil, Environmental, and Construction Engineering, University of Central Florida (UCF), for his invaluable suggestion and guidance throughout this research work. I genuinely acknowledge the intellectual support and academic guidance of Dr. Lei Zhai, Associate Professor, Nanoscience Technology Center and the Department of Chemistry, UCF, for my experimental works at Nanoscience Technology Center, UCF. I solemnly convey my gratitude to Joseph Zuyus, PhD student in the Department of Chemistry, UCF, for assisting with performing electrical property measurement experiments for this research effort. I also want to acknowledge my graduate course instructor Dr. Suryanarayana Challapalli, whose teaching in the relevant area of my research allowed me to explain the findings of research in nuance nature.

My very special thanks and gratefulness goes to my wife Kazi Mahmuda Tasneem and my colleagues for their cordial cooperation and support. Each one related directly or indirectly to this thesis work deserves thanks for their assistance without which it would not be possible.

TABLE OF CONTENTS

LIST OF FIGURES

LIST OF TABLES

LIST OF ABBREVIATION

AFM - Atomic Force Microscopy
ASTM - American Society For Testing And Materials
BNG - Boundary Nucleation and Growth
CF - Carbon Fiber
CI - Confidence Interval
CNT - Carbon Nanotube
DFT - Density Function Theory
EAH - Early Age Hydration
EDX - Energy Dispersive X-ray
ER/ρ - Electrical Resistivity
FA - Fly Ash
FESEM - Field Emission Scanning Electron Microscopy
FWHM - Full-Width-Half-Maximum
GB - Grain Boundary
GGBFS - Ground Granulated Blast Furnace Slag
GO - Graphene Oxide
GOCC - Graphene Oxide Cement Composite
MD - Molecular Dynamics
MOR - Modulus Of Rupture
OD - Oven Dry
OPC - Ordinary Portland Cement
PP - Polypropylene
PVA - Polyvinyl Alcohol
rGO - Reduced Graphene Oxide
rGOCC - Reduced Graphene Oxide Cement Composite
SEM - Scanning Electron Microscopy
SF - Silica Fume
SRO - Short Range Order
SSD - Saturated Surface Dry
TEM - Transmission Electron Microscopy

WD - Working Distance

XPS - X-Ray Photoelectron Spectroscopy

XRD - X-Ray Diffraction

ΔG - Free Energy Change

ΔG^* - Critical Free Energy Change

ΔG_{homo} - Free Energy of Homogeneous Nucleation

ΔG_{hetero} - Free Energy of Heterogeneous Nucleation

r - Radius of Nucleus/Nuclei

r^* - Critical Radius

F - Structure Factor

f - Atomic Scattering Factor

f_i - Atomic Scattering Factor of Atom i

I - Intensity of Peak

a, b, c - Lattice Parameter of Unit Cell

α, β, γ - Lattice Angle of Unit Cell

X,Y,Z - Cartesian Coordinates

P - Load Imposed on The Specimen

L - Span Length For Flexure Specimen

b - Average Width at Breaking Load

d - Average Depth at Breaking Load

r - Loading Rate

S - Rate of Increasing In Loading Rate On Tension Face

f_{cu} - Compressive Strength Of Cubic Specimen

T - Temperature

T_m - Melting Temperature

ΔT - Undercooling

n - Order of Reflection

λ - Wavelength

d_{hkl} - Interplanar Spacing Between Planes

θ - Angle of Reflection/Angle between Spherical Cap and Mold Wall

θ_B - Bragg Angle

2θ	-	Diffraction Angle
nm	-	Nanometer
m	-	Meter
psi	-	Pound Per Square Inch
Ω.m	-	Ohm.Meter
0D	-	Zero Dimension/al
1D	-	One Dimension/al
2D	-	Two Dimension/al
3D	-	Three Dimension/al

CHAPTER 1 INTRODUCTION

1.1 Problem Statement

Recent advancement in the field of nanotechnology have initiated the development of innovative nanoscale fibers which led to the origin of multifunctional materials (Lines, 2008) with advanced sensing, high performance cement based nanocomposite (Konsta-Gdoutos and Aza, 2014). In this regard, carbon based nanomaterials, prominently CNTs, was the forerunner for the application in cement based composites. Another 2D form of carbon based material, Graphene Oxide (GO), recently captured the attention of researchers as viable alternatives to other nanomaterials. Mechanical properties and microstructural aspects of GO-based cement composites have been investigated by the researchers thus far. But the behavior of cement hydration with the incorporation of GO is still not thoroughly investigated by the researchers. Another motive of using a nanomaterial in cement composite is due to its multi-functionality. GO falls short in this regard due to its inferior electrical conductivity compared to its parental origin, pristine graphene. As a result, researchers tend to lean towards thermally reduced or chemically reduced graphene oxide (rGO), which, being reduced from its' "-O-" components, possesses superior electrical properties compared to GO, and can be used to increase the conductivity of cement paste, which itself is slightly conductive in saturated condition.

1.2 Objectives and Overview

In this study, GO based cement composite (GOCC), and rGO based cement composite (rGOCC) were taken under consideration for the investigation of mechanical and electrical properties. Microstructural investigation using Scanning Electron Microscope (SEM), Energy

Dispersive X-ray (EDX), and X-ray Diffraction (XRD) techniques have been employed to understand the underlying behavior of mechanical and electrical characteristics of the composites. Early age hydration (EAH) of rGOCC was also investigated to relate the properties of composites with rGO concentration. This thesis consists of: (1) a comprehensive overview of historical background of toughening mechanism of cement composites, (2) mechanical, microstructural and electrical properties of GOCC thus far researched, (3) mechanical, microstructural and electrical resistivity of GOCC and rGOCC, (4) EAH of rGOCC for different concentrations of rGO to understand the mechanisms of cement hydration employing nanomaterials, (5) employment of SEM, XRD in this study and summary on data interpretation of XRD. The outcomes of this research are:

1. Compressive and flexural strength of GOCC and rGOCC incorporating different concentrations of GO and rGO, respectively
2. Electrical resistivity of rGOCC in oven-dry and saturated surface dry condition for 9 specimens
3. Nucleation mechanism of cement hydration for both GOCC and rGOCC using SEM and XRD
4. Comprehensive study of GOCC and rGOCC specimens with SEM/EDX and XRD

1.3 Organization of the Thesis

This thesis consists of five chapters. The first chapter provides a brief introduction of this research work. This chapter states the problem statement and research objective.

The second chapter provides a comprehensive literature review on the topics related to this research. These topics include the mechanical and electrical properties of GO, Hydration characteristics of cement, mechanical and electrical properties of GOCC, EAH characteristics of rGOCC, overview of application of SEM and XRD, data interpretation with XRD, determination of crystal structure with XRD, homogeneous and heterogeneous nucleation, and finally, the research gap and objective of this research study.

Chapter three represents the elaborate experimental procedure which includes the casting, the specimen preparation for mechanical and electrical tests, characterization techniques with SEM and XRD, the test setup and the collection of data.

Chapter four of this dissertation reports the results obtained from the mechanical tests for GOCC and rGOCC, microstructural results of the composites in relation to the macroscale properties, nucleation of C-S-H, and the comparison of the test results with the existing published works are also reported.

Finally, chapter five presents the major conclusions of the study and also provides recommendations for the further study.

CHAPTER 2 LITERATURE REVIEW

2.1 Introduction

Literature review on molecular structure electrical conductivities and mechanical properties of carbon based materials primarily, graphene, graphene-oxide, reduced graphene oxide and carbon nanotube are discussed in this chapter. Hydration characteristics of pristine cement and cement composites are presented in a nutshell. Mechanical Properties and electrical conductivities of carbon nanotube based cement composite are reviewed in lieu of microstructural characterization techniques such as Field Emission Scanning Electron Microscope (FESEM), Energy Dispersive Spectroscopy (EDX) and X-ray Diffraction (XRD). The supporting theory underlying FESEM, EDX and XRD methods are also discussed. Lastly, based on the literature review, research gap of current studies are discussed and research focus of this study is proposed.

2.2 Historical Background on Toughening Mechanisms of Cement Composites

Concrete is an essential material to meet our society's growing needs for housing, shelter, infrastructure etc. even in the foreseeable future. Annually, 2.3 billion tons of concrete are produced on a global basis (Ulm et al., 2010). However, Concrete is facing a downside even though it is the most preferred building material for the coherent increment of C-footprint. To reduce environmental impact of C-footprint, researchers have chosen to alter the chemistry of cement by "bottom-up" approach in contrast to the more conventional empirical approach. Bottom-up approach is defined as the nanoengineering of material from the building block starting at the electronic or atomic scale, and reflecting the behavior of the atomic scale to the macro scale (Ulm et al., 2010).

Cement, upon hydration, produces a range of products which evolves their structure depending on age and temperature and various other parameters. Cement is a non-metallic, non-crystalline/semi-crystalline material that comprises of four different phases. Cement composite is a highly brittle material, associated with self-destructive stresses originated due to plastic shrinkage, without any external loads. The addition of fillers, in the form of sand or aggregates, reduces shrinkage stresses, and at the same time enhances the fracture toughness of the resulting mortar or concrete (Shannag et al., 1997).

Enhancement of mechanical behavior of cement based composite is important, these are associated with inherent weakness in resisting tension (Chandler et al., 2000, Li and Maalej, 1996a). They are known to crack under low levels of tensile strain. Fracture behavior of brittle ceramic, such as concrete can be altered by manipulation of their microstructures. It has long been recognized that the behavior of such materials can be dramatically improved by the addition of discontinuous fibers. The improvement in composite properties is largely attributed to the bond between the fiber and matrix. The resistance to crack propagation provided by the fibers depends on the mechanical properties of the matrix, the fibers, and the fiber-matrix interface; as well as the fiber length, orientation, volume content, and spacing (Shah and Ouyang, 1991, Hsueh, 1991, Li and Maalej, 1996b). Microfibers can interact with the fracture evolution by arresting the growth of microcracks and can delay the propagation of microcracks which will coalesce to form the first macrocrack (Banthia and Nandakumar, 2003, Banthia and Sheng, 1996, Sivakumar and Santhanam, 2007), preventing of which can significantly improve the tensile strength of the composites (Lawler et al., 2003). Thus, historically cement based composite was started to be designed to enhance strength by incorporating microfiber.

In case of polyolefin fibers insufficient bonding is a problem and extreme slippage from matrix occurs at the stage of loading (Tosun-Felekoglu and Felekoglu, 2013). On the other hand, comparatively reactive nylon and polyvinyl alcohol (PVA) based fibers are susceptible to high bonding with matrix due to water affinity of fiber surface. Study reported that single fiber pull-out test results, embedded PP fibers tend to slip from cement–matrix when subjected to tensile loading, however, PVA fibers usually rupture before slipping (Li and Fischer, 2002).

Shannag et al. used densified small particle system (DSP) as high strength cement composite with mortar mix, fiber embedment length and fiber volume fraction as variables (Shannag et al., 1997). With the increase in fiber embedment length and volume fraction, the probability of fiber interlocking with the matrix increases, and so does the pullout load. Interground fiber cement is a new process where fibers are ground in with the cement clinker during the dry cement manufacturing process (Ostertag et al., 2001). A considerable increase in strength can be achieved for cement composite even at low fiber content due to homogeneous fiber dispersion and fiber modification during the milling process.

One of the effective means of achieving improved properties of cement based composite is the restriction of propagation and coalescence of cracks at microscopic level by incorporating $CaCO_3$ whisker (Cao et al., 2013), an inorganic single. Microscopic reinforcement is intended to strengthen and toughen the materials at µm and nm scale size by delaying the formation and propagation of microcracks which also can be accomplished by fibers. $CaCO_3$ whiskers can act as the fillers of the voids and the addition of whiskers can refine the large pores (Cao et al., 2013).

Incorporating 1 wt. % Boron Nitride (BN) in cement composite increases the toughness by 95%. Compressive strength of BN-cement composite is also increased by 75%

compared with pristine cement paste. In general, different types of mechanisms can be observed in BN- cement composite. According to Rafie et al. the multilevel toughening mechanism in BN-cement composite such as crack deflection, pull out of matrix sheets etc. can be attributed to the enhanced toughness property of the composite as seen (Rafiee et al., 2013b). GO sheets is used as a bridging material in cement paste to increase the mechanical properties. It has been reported that GO is used to hold together the tobermorite sheets of cement paste. The GO sheets pull the silicate layers closer together which can act as crack bridging zone (Rafiee et al., 2013b).

From the above discussion, it is well understood that, trends in incorporation of additional cementitious materials have been shifted from filler materials to nanomaterials started an era of domination of nanoengineering in cement research.

2.3 Molecular Structure, Physical and Mechanical Property of Carbon-based Materials

2.3.1 Graphene

Carbon was first discovered by Lavoisier around 220 years ago and coined by him as the elementary component of both diamond and graphite (Soldano et al., 2010). Since then more allotropes of carbon have been reported by the scientific community such as graphene (2D), graphite (3D), nanotubes (1D), or fullerenes (0D). Among these structures, graphite only possesses a different structure than those whereas graphene, nanotube and fullerene can be considered as different forms of same crystal structure originated from hexagonal array of sp^2 bonded carbon. Here C atoms are densely packed in a honeycomb crystal lattice with bond length of 1.41Å. Thickness of graphene tends to drift within 3.5Å to 10Å.

The breaking strength of graphene was reported to be 200 times stronger than that of steel making it the strongest material available to date (Kuila et al., 2012, Terrones et al.,

2010) with the Young's modulus of 1TPa. The strength of graphene is found to be depends on the number and types of defects present within the sheet (Terrones et al., 2010).

2.3.2 Graphene Oxide (GO)

Highly crystalline sheet of graphene typically is chemically inert. The surfaces of these sheets typically react with other atoms/molecules via physical adsorption originated by π-π bonding interactions. In this scenario, several chemical groups such as carboxyl (-COOH), carbonyl (-NH_2), hydroxyl groups (-OH) could be anchored (Terrones et al., 2010) as surface defects at the edges of the nanosheets, making the graphene surface chemically more reactive, which leads to the generic name graphene oxide (GO).

GO is a layered, mostly sp^3 (Mkhoyan et al., 2009, Liu et al., 2012) (C-O) bonded C-based compound that can be readily dispersed as individual sheets in a good solvent. Mechanical properties of GO polymer composites have been observed to increase with an addition of only a few weight percentage (Forati et al., 2014). The presence of different functional species such as carboxylates (–COOH) and carbonyl (-C=O) groups at the edges of the sheets on sp^2 hybridized C and hydroxyl (-OH), and epoxides (-O-) groups (Mkhoyan et al., 2009, Liu et al., 2012, Suk et al., 2010) (Figure 2.1 (a) and (b)) on the sp^3 hybridized C (Singh et al., 2011b, Compton and Nguyen, 2010), which enhances the bonding between GO nanosheets and cement matrix (Singh et al., 2011a). These functional groups provide reactive sites for various surface modification reactions to develop GO-based materials, (Singh et al., 2011b) i.e., GO-cement composites.

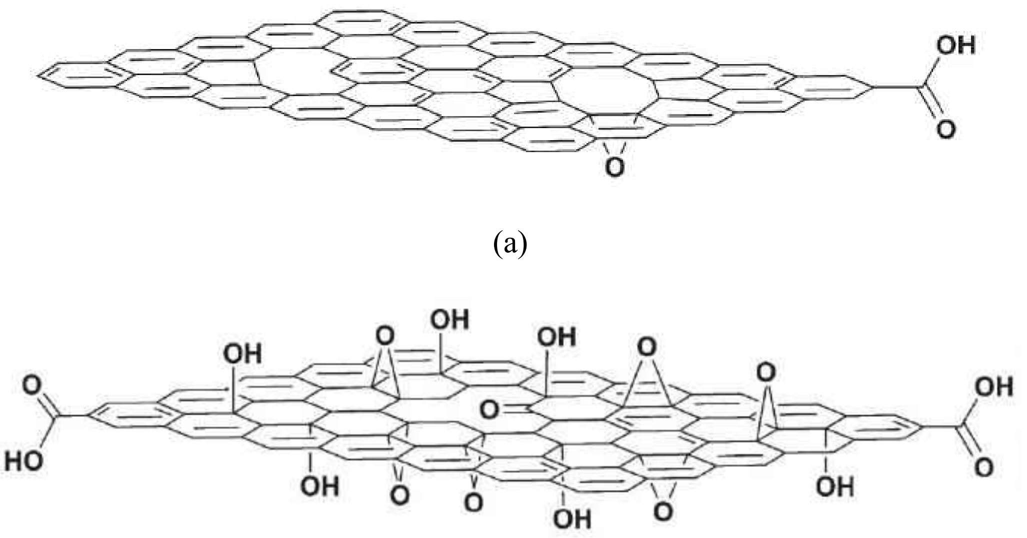

(a)

(b)

Figure 2.1: A schematic diagram of (a) graphene with sp^2 C-C bond, (b) graphene oxide (GO) sheet associated with the functional groups. Courtesy of Compton and Nguyen (Compton and Nguyen, 2010)

2.4 Characteristics of Cement

2.4.1 Hydration of Cement Phases

Portland cement (PC) is named after Portland stone found in Dorset, Leeds of UK due to the resemblance in color and quality with the latter. The raw materials used in the manufacturing of Portland cements consist primarily of alumina, silica, lime and iron oxide. Four compounds are considered to be the major constituents of Portland cement. They are tabulated in the Table 2.1 below along with their abbreviations. The calculation of the composition of Portland cement compounds is based on the works of R.H. Bogue and others, and often termed as Bogue Composition (Neville, 2011).

In addition to the main constituents of Portland cement listed in Table 2.1, minor constituents also exist such as MgO, TiO_2, Mn_2O_3, K_2O and Na_2O. These compounds actually consist about a few percent of the mass of cement. C_2S is known to have up to four forms. α-C_2S converts to β-C_2S at about 1450℃ which undergoes further conversion to γ-C_2S at about 670℃. But in commercial cement, β-C_2S is the prevalent form of C_2S in the clinker (Neville, 2011). C_3A and C_4AF are rectangular crystals and solid solutions respectively. The reactions between the compounds of Portland cement partake inside the cement paste. In the presence of water, the silicates and aluminates present in Portland cement reacts and forms hydrated products, which in time, produce firm and hard mass called as hydrated cement paste. Le Chatelier was the first to observe some 100 years ago that the hydrated products of cement are the same as the products showed the individual compounds (Neville, 2011). The two silicate compounds are prominent in cement, and the physical behavior of cement is similar to that of demonstrated by these two compounds individually. The other two compounds C_3A and C_4AF acts as flux in the cement. They add no strength in the hydrated cement paste but are required for the cement manufacturing process.

The progress of hydration of cement can be observed by various means such as: (a) the amount of $Ca\ (OH)_2$ in the paste; (b) the heat evolve during hydration; (c) the amount of unhydrated cement paste; and (d) indirectly from the strength of hydrated paste. Continuous X-ray diffraction (XRD) scanning of cement paste undergoing hydration can be used to study early hydration products. Scanning electron microscopy (SEM) can also be undertaken to observe the microstructure of hydration products.

Table 2.1: Main constituents of Portland cement

Name of the constituent	Oxide composition	Abbreviation
Tricalcium silicate	$3CaO.SiO_2$	C_3S
Dicalcium silicate	$2CaO.SiO_2$	C_2S
Tricalcium aluminate	$3CaO.Al_2O_3$	C_3A
Tetracalcium aluminoferrite	$4CaO.\ Al_2O_3.Fe_2O_3$	C_4AF

2.4.2 Early Age Hydration Characteristics depending on Temperature

Although characteristics of OPC have been studied for centuries, the complex hydration properties are still under considerable scrutiny (Kumar et al., 2012b). Hydration of cement undergoes considerable amount of phase changes including dissolution and precipitation (Jansen et al., 2012) during the process upon coming into contact with water for the first time. Hydration of cement is a complex and exothermic process where up to 500 J/g of cement of heat is evolved during hydration (Kumar et al., 2012b) and most of the heat evolution ensue during the early age of hydration (EAH) of OPC, during the first 24 h.

Due to the large amount of heat evolution because of exothermic reactions coupled with the insulating behavior of cement, the temperature build up in cement paste leads to the cracking of cement blocks/concrete during the cooling period. In this scenario, mineral admixtures or other nanomaterials are used in cement/concrete in order to reduce the early heat evolution during hydration of cement (Liu et al., 2015).

Historically, mineral admixtures such as SF, FA, GGBFS, metakaolin etc. have been used to diminish the heat evolution of cement pastes (Langan et al., 2002). More recently, researchers started incorporating nanomaterials such as nano-SiO_2, nano-TiO_2, nano-Fe_2O_3, nano-Al_2O_3 etc. as nanomaterials in the cement pastes for various functional factors, one of which is to reduce the early heat evolution of cement (Land and Stephan, 2015). These nanomaterials provide large reactive surfaces which catalyzes the nuclei of hydration products on the surfaces of cement grains and onto themselves (Land and Stephan, 2015).

The EAH period of OPC is subdivided into distinct four periods or durations. These periods are called: (I) the initial period, (II) the induction period, (III) the acceleration period, and (IV) the retardation period (Jansen et al., 2012) (Figure 2.2). However, some researchers further divide the retardation period to two more periods (Kumar et al., 2012b) naming, deceleratory period and retardation period ensuing five total periods for EAH of OPC.

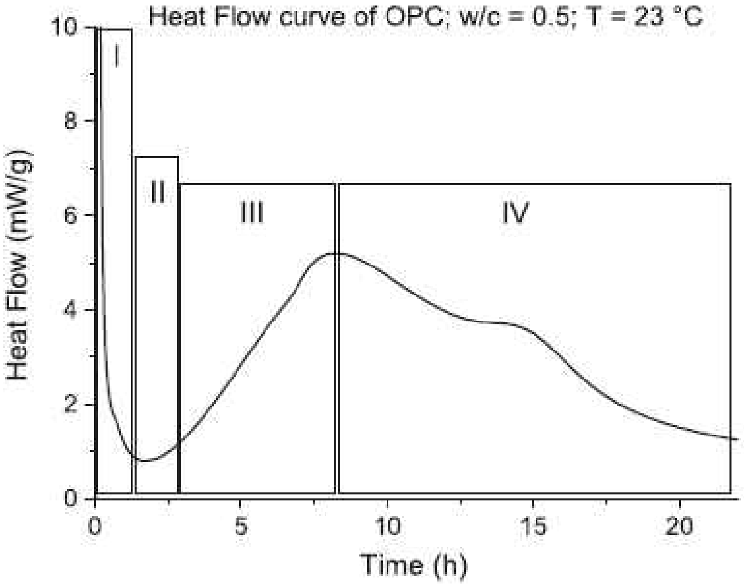

Figure 2.2: Heat flow diagram of OPC (Courtesy of Jansen et al. (Jansen et al., 2012))

The quantity of heat along with the rate at which the heat is evolved depends on the mineralogical and morphological characteristics of the produced cement clinker which depends on number of factors including: (1) water/binder ratio, (2) the fineness of cement clinker, (3) particle size distribution, (4) specific surface area, (5) curing temperature (Tydlitát et al., 2014), (6) presence of mineral (Langan et al., 2002) and chemical admixtures (Kumar et al., 2012b), (7) presence of nanomaterials (Land and Stephan, 2015).

During the EAH, two reactions, particularly, silicate reaction and aluminate reaction, as shown in Equations 2.1 and 2.2, respectively, commandeer the hydration reactions and resulting heat flow according to Jansen et al. (Jansen et al., 2012):

$\mathrm{C_3S + 3.9H \rightarrow\ C_{1.7}SH_{2.6}{+}1.3H}$ (silicate reaction) (2.1)

$\mathrm{C_3A + 3CS + 32H \rightarrow C_3A * 3CS * H_{32}}$ (aluminate reaction) (2.2)

During the initial period (I), a rapid heat evolution occurs due to the wetting of cement grains upon receiving water, dissolution of several ions consisting the cement phases, and the hydration of hemihydrate ($CaSO_4$. $0.5H_2O$) and aluminate (C_3A) phases. The heat evolution rate plummets to a very low value within 5 min followed by a constant progression <2 h, which is called induction period (II), alternatively dormant period. During the dormant period, formation and disintegration of embryos or clusters continue until the critical radius for nuclei is attained (Kumar et al., 2012b). After the initial period, the hydration accelerates and the rate of heat evolution reaches to a maximum at around 6 h of hydration. The responsible catalyst for this period is alite. After the maximum peak of accelerating period (III), deceleratory period starts to follow. Not long after the maximum peak, another maxima appears around 12 h of hydration which is described by Lerch (Lerch, 1946) as "sulfate depletion peak" because of the higher rate of C_3A dissolution and ettringite precipitation. The heat evolution continually decreases after the surface depletion peak and the reaction is thought to become diffusion controlled due to the formation of large amount of hydration products which is also visually evident from the microstructural characterization of the cement pastes. With the decrease of the heat flow curve, the hydration rate also decreases and the retardation period (IV) ends. It's been evident during the EAH that C_3S and C_3A plays prominent role in the hydration process along with several other factors already described above.

In this research, temperature evolution during the hydration of cement composites will be regard as primary data to evaluate the EAH process alongside microstructural characterization techniques to buttress the temperature data.

2.5 Graphene Based Cement Composite

2.5.1 Physical, Mechanical and Microstructural Property

GO, emerging from the chemical exfoliation of graphite, is a good candidate for cement-composite due to its' high aspect ratio, excellent dispensability in water and enhanced mechanical property. Pan et al. showed that, the incorporation of 0.05 wt. % GO can increase the compressive strength of GOCC up to 15-33% and flexural strength up to 41-59% respectively (Pan et al., 2015). Elastic modulus increased to 3.70 GPa from 3.48 GPa (Pan et al., 2015) from cement paste indicating slight increased only probably due to the forming of low number of cracks by the crack arresting of GO. SEM image (Pan et al., 2015) showed that compared to other nano-fillers, GO exhibit unique 2D structure which can deflect, tilt or twist around the crack ensuing higher mechanical strength. Moreover, the pore volume and pore diameter comparison by Pan et al. (Pan et al., 2015) between cement paste and GO incorporated cement paste showed that they are quite similar in this aspect. Lv et al. reported that the mechanical properties of GO-cement paste composite (Lv et al., 2013) depend upon the GO content as well as the shape of the nucleated crystal (Lv et al., 2014) upon hydration. Rafiee et al., (Rafiee et al., 2013a) reported that GO can enhance the mechanical properties by inhibiting the propagation of cracks microstructurally. GO can also be used as oil adsorption material in underwater construction structures (Rafiee et al., 2013a). Babak et al., (Babak et al., 2014) reported that the GO-cement composite exhibited 48% increase in the tensile strength because of the non-agglomeration of GO in the matrix and nucleation of C-S-H around GO platelets. Han et al. have used CNT in concrete pavement as a stress sensor by measuring electrical resistance upon traffic flow on the pavement (Han et al., 2009).

Horszczaruk et al. (Horszczaruk et al., 2015) showed that Young's modulus of GOCC hover between 5-20 GPa depending on the GO content. He concluded from the comparison of nanosilica cement composite with GO cement composite that the latter has similar effect on the hydration process resulting in an emerging nanomaterial on the verge. Extending the research on GO cement composite, Mohammed et al. (Mohammed et al., 2015) reported that the total porosity increased with the incorporation of GO in the cement mix. However, with the addition of more GO content, the porosity decreased eventually. He concluded that GO has the capability of folding and twisting because of its irregular wrinkly shape which may lead to the higher porosity because of different arrangement of C-S-H and other hydration products. But as GO content increases, their capability of twisting and bending are diminishes, and as a result, porosity decreases (Mohammed et al., 2015). Contrary to the porosity test, chloride penetration also decreased with the incorporation of GO in the cement paste followed by increasing trend with the addition of more GO content.

Li et al. (Li et al., 2015) reported that fracture strength of GOCC increased steadily to ~13 MPa (an increase of 51% compared to the control cement paste) at 1.5 wt% GO content followed by a reduction at 2 wt % GO. TEM, XPS and XRD analyses were also performed by these researchers.

2.5.2 Electrical Property

The electrical resistivity of cement paste has been an attractive subject among the cement researchers (Topçu et al., 2012). Electrical conductivity (EC) occurs primarily due to ion transport through the pore solution in the cement based system and it is an important parameter to study the hydration process at early stages (Topçu et al., 2012). During hydration, the capillary pores in the cement are gradually filled up with hydration products such as C-S-H, CH, ettringite and the conductivity decreases over time. It is to be noted that conductivity $\propto \frac{1}{\text{Resistivity}}$.

The EC for various blended cement pastes found to be decreasing with increasing hydration time (Morsy, 1999). The decrease may be attributed to the formation of layer of hydration products on the surface of cement grains and higher level of consumption of ions (Salem, 2002, Morsy, 1999). As a result, fewer ions are available for ionic conduction and also these ions have to find out tortuous path through the capillary pores to carry charge (Morsy, 1999). Salem also reported a sharp decrease in conductivity value after 30 min of hydration (Salem, 2002).

Graphite oxide based composites are not appropriate candidates for conductive materials because of the turbulence in the crystal lattice. For the application of graphene and its' derivatives as conductive materials, rGO is an viable alternative (Thinh et al., 2012). In this research, most of the specimens tested were OD to avoid the ionic conduction. As a result, the conduction that was observed probably was due to the electronic conduction.

2.6 Field Emission Scanning Electron Microscope (FESEM) and Energy Dispersive X-ray Spectroscopy (EDX) (Schematic Diagram of SEM and EDX)

The scanning electron microscope (SEM) uses a focused beam of high-energy electrons to generate a variety of signals at the surface of solid specimens. The signals that derive from electron-specimen interactions reveal information about the specimen including topographic structure, chemical composition, and crystalline/amorphous structure and orientation of the crystals comprising the specimens. The typical electron-specimen interactions depict the following variations (Figure 2.3):

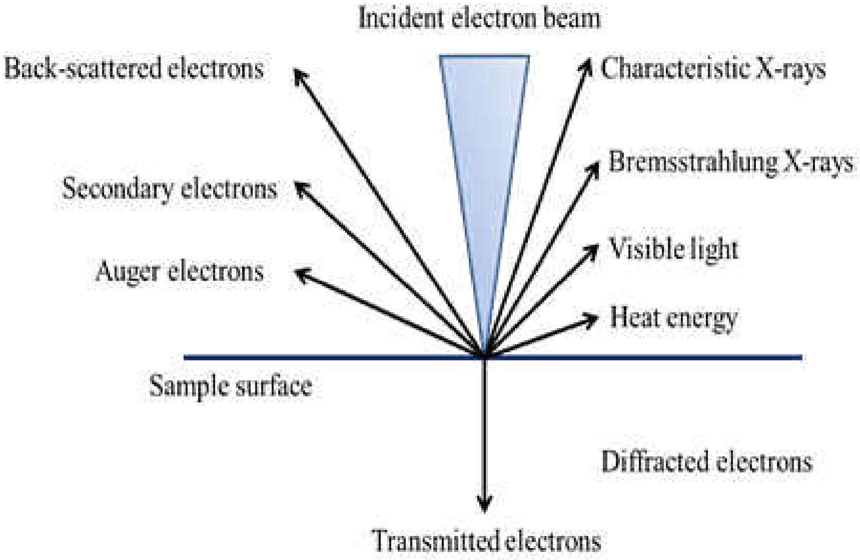

Figure 2.3: Electron-Matter interaction inside a generic SEM chamber

As we can see from the Figure 2.3, electrons entering the sample can result in a number of interactions with the atoms comprising the samples. Accelerated electrons can pass through the material without any interaction, i.e. elastic scattering or, it can experience inelastic scattering where the electrons undergo loss-of-energy. Elastic and inelastic scattering originates number of signals as described above.

On the impinging point of electron and the sample, there develops a volume related to electron scattering, photon and X-ray production. These include:

- The energy of the incident electron beam increases the interaction volume, but decreases the elastic scattering
- The interaction volume decreases as a function of mean atomic weight

Each of the signals used are generated from different location on the interaction volumes, and as a result, each of the signal has different image resolution. From these discussions, it can be explained that secondary electrons possess the best image resolution along with auger electron. Figure 2.4 shows typical arrangement of an SEM.

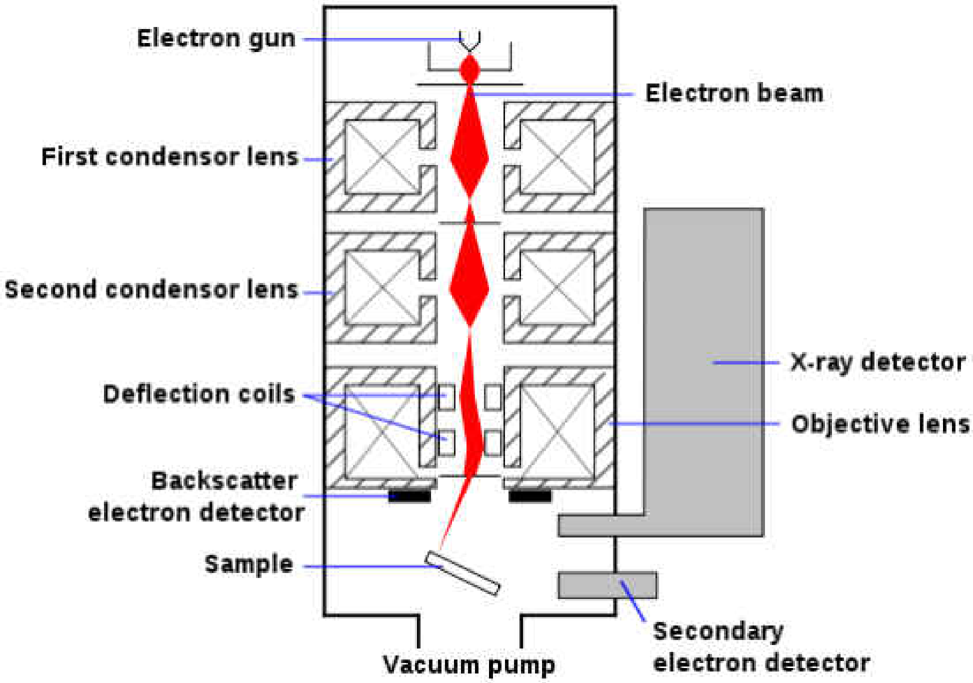

Figure 2.4: Schematic diagram of SEM

Other advantages of SEM over optical microscopy include:

- SEM benefits from a large depth of field so most of the specimen surface is simultaneously in focus whatever the surface roughness is.
- Much higher magnification can be obtained with SEM with an ultimate resolution of 1 nm.
- SEM permits non-destructive evaluation of the specimen.
- Large specimen can be tested.

FESEM actually include all of the above advantages of SEM and moreover, it demonstrates:

- The ability to examine smaller-area contamination spots at electron accelerating voltages compatible with energy dispersive X-ray (EDX).

- Reduced penetration of low-kinetic-energy electrons probes closer to the immediate material surface
- High-quality, low-voltage images with negligible electrical charging of samples (accelerating voltages ranging from 0.5 to 30 kilovolts).
- Essentially no need for placing conducting coatings on insulating materials.

EDX analysis in SEM is the most common application of X-ray microanalysis. From this analysis, it is possible to get very useful quantitative results from a wide range of materials. But, it should be noted that the data not be misinterpreted. It is needed to have a clear knowledge of the technique for quality microanalysis (Bell and Garratt-Reed, 2003).

Energy Dispersive X-ray analysis (EDX), also refer to as EDS or EDAX, is an X-ray technique used to identify the elemental composition of a specimen. Application includes materials and product research, trouble shooting, de-formulation etc.

EDX systems are additional attachments to SEM instruments where the imaging capability of the microscope is used to identify the specimen of interest. The data generated by EDX analysis consist of spectra showing peaks corresponding to the elements making up the true composition of the sample being analyzed.

In a multi technique approach EDX becomes very powerful, particularly in contamination analysis and concrete characterization. The technique can be qualitative, semi-quantitative, quantitative, and also provide spatial distribution of elements. The EDX technique is non-destructive and specimens of interest can be examined with little or no sample preparation.

2.7 X-ray Diffraction

2.7.1 Bragg's Law

The first ever crystal structure reported was that of NaCl by father and son W. H. and W. L. Bragg in 1913. By 1957, the theory of crystal diffraction was advanced sufficiently and the structure of penicillin was published. In 1958, the first ever three dimensional model of a complex protein called myoglobin was determined (Tilley, 2006).

The underlying theory behind this attribute of diffraction is a beam of radiation will only be diffracted if it impinges upon a set of planes in a crystal defined by the Miller indices (hkl). If the geometry of the situation fulfils specific conditions, the Bragg's law is defined in Equation 2.3 as:

$$n\lambda = 2d_{hkl}\sin\theta \qquad (2.3)$$

where n is the order of reflection, λ is the wavelength of the radiation, d_{hkl} is the interplanar spacing between the (hkl) planes of atoms in a crystal and θ is the diffracted angle of Bragg angle, as shown in Figure 2.5. Alternatively, it can be said that the planes of atoms will diffract radiation only when illuminated at an angle $\theta_B=\sin^{-1}(n\lambda/2d_{hkl})$. Here, θ_B is termed as Bragg angle. The angle between the direction of incident beam and diffracted beam is equal to 2θ. Bragg's law gives the situation under which the diffraction occurs and the position of the diffracted beam.

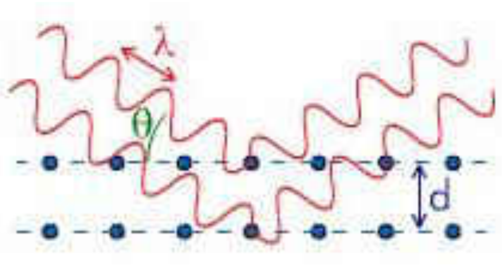

Figure 2.5: Incident and Scattered Electron beam on a particular lattice plane of a crystal

Bragg's law applies to all the infinite number of sets of atomic planes inside a crystal. Thus, if a crystal is rotated in a beam of radiation, each set of planes will diffract the radiation when the value of sinθ becomes appropriate. This is the principle by which diffraction data is collected for the whole crystal in powder format which means no preferred orientation. The arrangement of the diffraction beam, when taken together, is the diffraction pattern of a crystal.

2.7.2 Bravais Lattice and Determination of Crystal Structure (Table of Bravais lattice)

All the materials fall under seven crystal systems and 14 crystal lattices (Callister and Rethwisch, 2013) which are depicted in Table 2. The axial relationships between the unit cells of the crystals are also shown in the Table 2.2.

Table 2.2: Lattice parameter relationships showing seven crystal systems

Crystal System	Axial Relationships	Interaxial Angles	Bravais Lattice
Cubic	$a = b = c$	$\alpha = \beta = \gamma = 90^0$	3
Hexagonal	$a = b \neq c$	$\alpha = \beta = 90^0, \gamma = 120^0$	1
Tetragonal	$a = b \neq c$	$\alpha = \beta = \gamma = 90^0$	2
Rhombohedral	$a = b = c$	$\alpha = \beta = \gamma \neq 90^0$	1
Orthorhombic	$a \neq b \neq c$	$\alpha = \beta = \gamma = 90^0$	4
Monoclinic	$a \neq b \neq c$	$\alpha = \gamma = 90^0 \neq \beta$	2
Triclinic	$a \neq b \neq c$	$\alpha \neq \beta \neq \gamma \neq 90^0$	1

The In the Table, a,b,c are lattice parameters in X,Y,Z directions and α,β, and λ are angles between y-z, x-z and x-y axes, respectively.

The most common phases found in cement are summarized in the Appendix B according to ASTM C1365 (ASTMC1365, 2011) specification. For the convenience, the common phases and their alternative nomenclature are summarized in a separate Table (Table 2.3).

Table 2.3: Common phases and formulas of cement phases before and after hydration

Common phases		Chemical Formula	Cement Chemists' Notation	Alternative Name
Before Hydration	Tricalcium silicate	$3CaO.SiO_2$	C_3S	Alite
	Dicalcium silicate	$2CaO.SiO_2$	C_2S	Belite/ Larnite
	Tricalcium aluminate	$3CaO.Al_2O_3$	C_3A	Celite
	Tetracalcium alumino-ferrite	$4CaO.(Al,Fe)_2O_3$	C_4AF	Brownmillerite
	Gypsum	$CaSO_4.2H_2O$	CS	
After Hydration	Calcium hydroxide	$Ca(OH)_2$	CH	Portlandite
	Ettringite	$Ca_6Al_2(SO_4)_3(OH)_{12}.26(H_2O)$	---	AFt
	Jennite	---	---	---
	Tobermorite	---	---	---
	Calcium carbonate	$CaCO_3$	---	Calcite

It can be seen that mostly the unit cells found in the crystalline phases of cements are hexagonal, monoclinic, orthorhombic and triclinic which also demonstrates that there are not much symmetry in the cement phases.

2.7.3 Calculation of Interplanar Spacings and Miller Indices

The peak positions alternatively known as Bragg angle in XRD patterns reveals the interplanar spacings between the diffracting planes, from which crystal structure determination is possible. On the other hand, the diffracting miller indices of planes lead to the structure factor calculation, which can be used to calculate the peak intensity. Peak intensities of XRD patterns determine the atomic coordinates of the atoms in the unit cell (Cullity, 1956). A simple example for determination of interplanar spacings and structure factor calculation of a face centered cubic (FCC) crystal is described in the following section.

Structure Factor can be determined from the Equation 2.4,

$$F = \sum_{i=1}^{N} f_i e^{2\pi i(hu+kv+lw)} \qquad (2.4)$$

Assuming, Intensity of the diffraction spot, $I \propto F^2$

Here,

f_i = Atomic scattering factor of atom i

h,k,l = miller indices

u,v,w = fractional coordinates of atom i

Coordinates of atoms in FCC: $[0,0,0]$ $\left[\frac{1}{2},\frac{1}{2},0\right]$ $\left[\frac{1}{2},0,\frac{1}{2}\right]$ $\left[0,\frac{1}{2},\frac{1}{2}\right]$

As a result the structure factor reveals in Equation 2.5 as,

$$F = f\left(1 + e^{\pi i(h+k)} + e^{\pi i(k+l)} + e^{\pi i(h+l)}\right) \qquad (2.5)$$

So, if (hkl) is mixed (i.e., odd and even), F is present, and for unmixed (hkl), F=0, consequentially I is also 0.

The extinction rules for diffraction spots of FCC crystals and the only permissible diffraction spots are clearly shown in Tables 2.4 and 2.5.

Table 2.4: Extinction rules for FCC material

h,k,l	F	I
Mixed (even and odd)	0	0
Unmixed (either all odd or all even)	4f	$\lvert 4f\rvert^2$

The (hkl) values can be calculated from the Equation 2.6 for cubic crystals.

$$\frac{1}{d^2} = \frac{h^2+k^2+l^2}{a^2} \qquad (2.6)$$

If the F is calculated for different (hkl) values starting from (100), the diffraction pattern will be comprised of the following peaks.

Table 2.5: Theoretical diffraction pattern of a FCC crystal for several (hkl) value

hkl	$h^2+k^2+l^2$	Status of peak
100	1	✓
110	2	✗
111	3	✓
200	4	✓
210	5	✗
211	6	✗
220	8	✓
221/300	9	✗
310	10	✗
311	11	✓
222	12	✓

The diffraction pattern for pure Co (an FCC crystal) should resemble as the following graph in Figure 2.6.

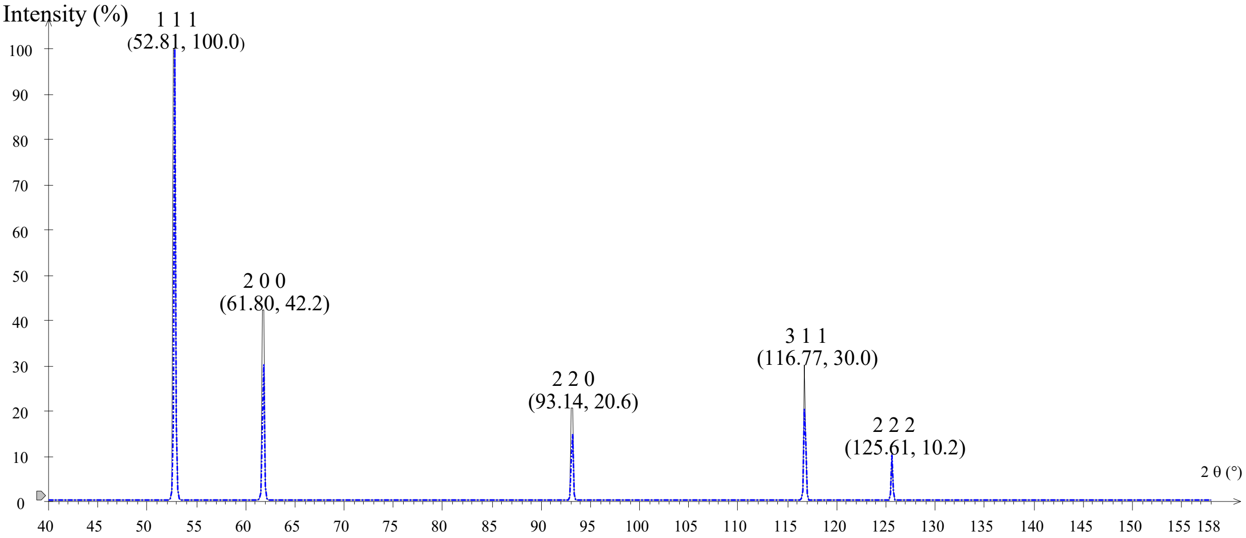

Figure 2.6: Typical X-ray diffraction pattern of a pure FCC metal

From this above Figure (Figure 2.6), it is evident that the theoretical calculation depicts only the mixed indices for an FCC crystal. Details of the calculation of interplanar spacings are given in Appendix A.

2.8 Theory of Nucleation and Growth of Phases

2.8.1 Homogeneous Nucleation

If a given volume of liquid is at a temperature ΔT below melting temperature T_m with a free energy G_l and some of the atoms clustered together to form a small sphere of solid as in Figure 2.7, the free energy change can be calculated by the following formula (Equation 2.7) (Porter et al., 2009):

$$\Delta G = \frac{L_V \Delta T}{T_m} \tag{2.7}$$

Here, ΔG is free energy change due to the formation of solid from liquid, and L_v is the latent heat of fusion per unit volume. The excess free energy associated with the solid particle can be minimized with carful approximation of particle shape as shown in Equation 2.8:

$$\Delta G_r = -\frac{4}{3}\pi r^3 \Delta G_V + 4\pi r^2 \gamma_{SL} \tag{2.8}$$

Here, r is radius of spherical particle, and γ_{SL} is interfacial surface between solid and liquid.

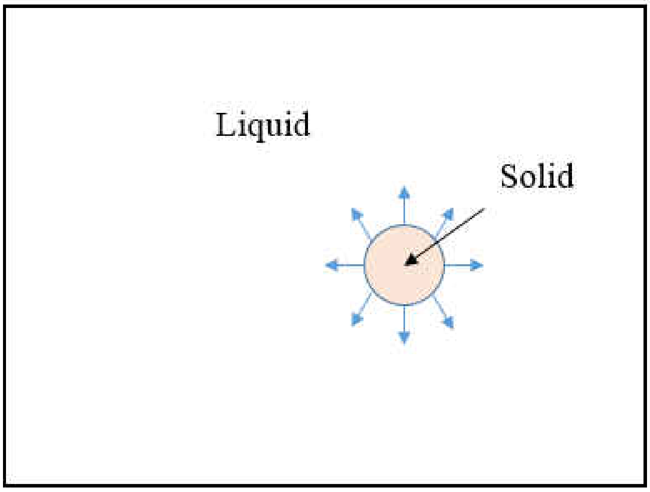

Figure 2.7: Homogeneous nucleation

If r<r* (r*=critical nucleus size/radius), the system can lower its' free energy by dissolution of solid, whereas, when, r>r*, the free energy of the system increases, when solid grows. Solid particles with r<r*, are knowns as clusters because they are unsTable. On the other hand, r>r* is known as nuclei. When, dG= 0, r=r*, and as a result, the cluster is in equilibrium with its' surroundings. The critical nucleus size and critical free energy, can be obtained by the Equations 2.9 and 2.10,

$$r^* = \frac{2\gamma_{SL}}{\Delta G_V} \tag{2.9}$$

$$\Delta G^* = \frac{16\pi\gamma_{SL}^3}{3(\Delta G_V)^2} \tag{2.10}$$

2.8.2 Heterogeneous Nucleation

The formation of an embryo on the surface of a mold or defect can be shown schematically by the following Figure 2.8.

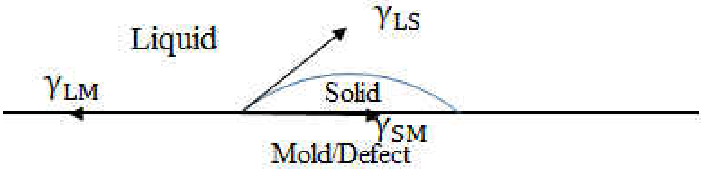

Figure 2.8: Heterogeneous nucleation

Excess free energy (shown in Equation 2.11) associated with the formation of the embryo is,

$$\Delta G_{het} = -V_S\Delta G_v + A_{LS}\gamma_{LS} + A_{SM}\gamma_{SM} - A_{SM}\gamma_{ML} \tag{2.11}$$

Here, V_S is the volume of the spherical formation, A_{LS} and A_{SM} are solid/liquid and solid/mold interfaces, γ_{LS}, γ_{SM}, and γ_{ML} are liquid/solid, solid/mold and mold/liquid interfacial energies, respectively. ΔG_{het} can be written in terms of cap radius r and wetting angle θ as in Equation 2.12,

$$\Delta G_{het} = \left\{-\frac{1}{3}\pi r^3\Delta G_v + 4\pi r^2\gamma_{LS}\right\}S(\theta) \tag{2.12}$$

Here, $S(\theta)$ is shape factor of particles.

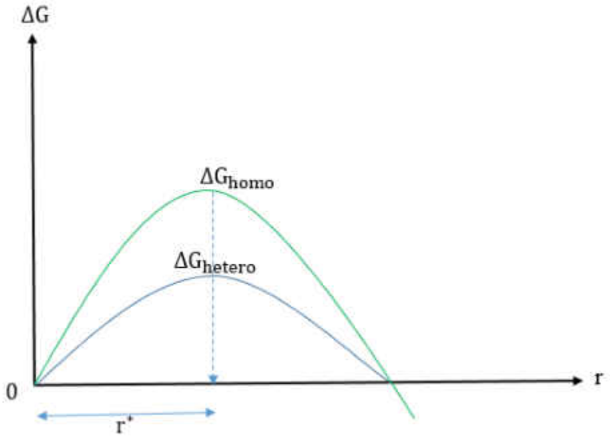

Figure 2.9: Variation of free energy for homogeneous and heterogeneous nucleation with the radius of nuclei

As $S(\theta)$ will always be ≤ 1, hence, $\Delta G_{\text{het}} \leq \Delta G_{\text{hom}}$ as shown in the Figure 2.9. Because, activation energy for heterogeneous nucleation is actually lower than that of homogeneous nucleation, the rate of occurrence of the former is much higher. Depending on the defect present, the rate of heterogeneous nucleation varies. Different kinds of defects include:

- Vacancies (0D defect:. both substitutional and interstitial)
- Dislocations (1D defect: edge and screw or mixed)
- Grain boundaries (2D defect)
- Twin boundaries (2D defect)
- Surfaces (2D defect)
- Antiphase boundaries (2D defect)
- Pores, voids (3D defect)
- Second phase particles (3D defect)

2.8.3 Nucleation and Growth Processes of Cement Grains

It is well established that the nucleation and growth process control the mechanism of cement hydration (Kumar et al., 2012a).Early age hydration (EAH) is progressed by the mechanism of nucleation and growth of hydration products, most importantly from C_3S and C_2S. These experimental results are also supported by plethora of analytical models and simulation results, among which the model presented by Johnson-Mehl-Avrami-Kolmogorov (JMAK) model is the preeminent (Scherer et al., 2012, Bishnoi, 2013). A simplified form of the Avrami Equation (Equation 2.13) is as follows:

$$-\ln(1-V) = kt^n \tag{2.13}$$

Here, V is the fraction of volume transformed, k is a constant depending on the rate of nucleation and growth, and t is time.

JMAK model assumes that nucleation occurs randomly throughout the hydration space but in fact employing Cahn's model of transformation of polycrystalline materials, Thomas (Thomas, 2007) showed that, nucleation occurs along grain boundary (GB). His research actually gave a better fit to the calorimetric data compared to the JMAK model although it assumed that the rate of nucleation was constant throughout the process. However, computer simulations indicated that there are sudden bursts of nucleation in the early few minutes of hydration and then growth continued from the sTable nuclei (Scherer et al., 2012). Scherer et al. (Scherer et al., 2012) concluded that the Cahn's model is only valid for the nucleation and growth kinetics of EAH, especially when single phase is reacting (namely, C_3S).

From the literature review, it is well known that energy barrier will dictate the occurrence of homogenous or heterogeneous nucleation. Zeng et al. (Zeng et al., 2015) was, to the best of knowledge, first reported that strong heterogeneous nucleation are responsible for the formation of ice embryo from NaCl solutions that were confined within cement paste.

So far, no reports are available about the involvement of homogenous and heterogeneous nucleation on GO/rGO cement composite.

2.9 Research Gap and Focus of this Research

Although, researchers discussed above have studied the mechanical and microstructural properties of GO-contained cement paste in the recent years the studies focused mostly around the mechanical properties and microstructural behavior of the GOCC. The cause of increase in strength from the nanoscale standpoint due to the incorporation of GO in cement paste is overlooked.

Cement phases react with water to form C-S-H gel (Neville, 1995). It was observed experimentally that when GO is incorporated in the cement and water, it tends to hold the microcracks together resulting in higher strength (Lv et al., 2013). On the other hand, it is believed that the functional groups (Kuila et al., 2012) associated with GO can act potential seeding sites for the nucleation of C-S-H. As GO content increases, so does the number of these nucleation sites, resulting in a formation of large number of C-S-H nuclei. Moreover, the activation energy for formation of stable nucleus are lowered due to the heterogeneous nucleation (Callister and Rethwisch, 2013), resulting in fewer atoms to form a nucleus which leads to finer particles. It is established by extensive experiments on metals and ceramics that strength of a material somewhat increases with decrease in square root of (Abbaschian et al., 2008) grain size, which can be quantitatively determined by the famous Hall-Petch relationship.

For example, Bullard (Bullard, 2008) and Livingston (Livingston et al., 2001) reported that heterogeneous nucleation of C-S-H on C_3S surfaces could account for the evolution of degree of hydration. Luc suggested that the degree of hydration also depends on the number of seeding sites (Nicoleau, 2010). Wu and Young (Wu and Young, 1984) attributed the accelerated rate of hydration of C_3S on colloidal silica to C-S-H nucleating on the surface of silica particles. They observed that if the C_3S paste has no seeding, the normal nucleation and growth process does not provide enough C-S-H surfaces for appreciable growth rates to occur. They concluded that the accelerate hydration rates are characterized by nucleation and growth of C-S-H which must have enough growing regions, i.e. nucleation sites.

To prove our hypothesis, AFM, XPS, SEM/EDX and XRD material characterization techniques are employed alongside compressive strength tests for the primary measure of strength. AFM determines the thickness of the GO sheets and XPS evaluates the presence of functional groups of GO. SEM and EDX provide information about the different forms of C-S-H that play critical role in proving the occurrence of heterogeneous nucleation in GO-cement paste system. XRD was used to prove the presence of actual hydration products and their crystallite sizes alongside with their tentative quantity from corresponding peak areas which are essential to prove our hypothesis of heterogeneous nucleation due to GO.

After extensive literature review of GO-based, several research gaps come into view. These research gaps and focus of this current research are discussed below.

Although GO-cement composite research is at its' infancy compared to the CNT-cement research, there have been some establishments of some good papers and researchers. However, the results reported revolve around the mechanical properties of GO-cement composite and their microstructural evolution with hydration periods. But few attempts have been made to describe the hydration properties of GO cement composite in fundamental approach of phase transformation- nucleation and growth process. In this research, SEM and XRD techniques were employed to understand the nucleation procedure of GO-cement composite.

Mechanical properties of rGO-cement paste are investigated. rGO is on the order of interest because of its' proximity to the graphene in behavior.

EAH hydration characteristics of rGO-cement composite are also investigated. Nucleation behavior of rGO-cement paste in lieu of EAH hydration is investigated.

Lastly, electrical resistivity of rGO-cement composite is studied and compared with existing data from other composites.

CHAPTER 3 METHODOLOGY AND EXPERIMENTAL TECHNIQUES

3.1 Introduction

This chapter explains the materials and methods used for carrying out numerous mechanical properties, microstructural and electrical conductivity tests. Specimens for GOCC and rGOCC are prepared with 0.01 wt. % and 0.05 wt. % concentration of GO. 0.5%, 1%, and 5% rGO were chosen as the regimented concentration for rGOCC for ER tests. Microstructural property tests were conducted on stipulated specimens of GOCC and rGOCC on different test days using FESEM/EDX and XRD techniques. Early age hydration characteristics of rGOCC were evaluated with FESEM/EDX and XRD techniques. Moreover, heat evolutions during the hydration of the specimens are determined using indirect temperature measurement techniques on different GOCC and rGOCC specimens.

3.2 Materials Used for Graphene-Oxide Cement Composite (GOCC) Specimen

3.2.1 Materials and Tests

3.2.1.1 Cement

Ordinary Portland cement (OPC) confirming to ASTM C150 (Type II) is used as primary binding material in casting of cement composite. Water/cement (w/c) ratio for casting of cement composite is 0.50 by the weight of cement.

3.2.1.2 Graphene Oxide (GO)

Graphene oxide was prepared from natural purified graphite by modified Hummers method from natural graphite powder purchased from Dixon Graphite (Microfyne). 10 mg of

GO was dispersed in 10 mL of deionized water (DI water) using cup-horn ultrasonication to generate a homogeneous brown solution.

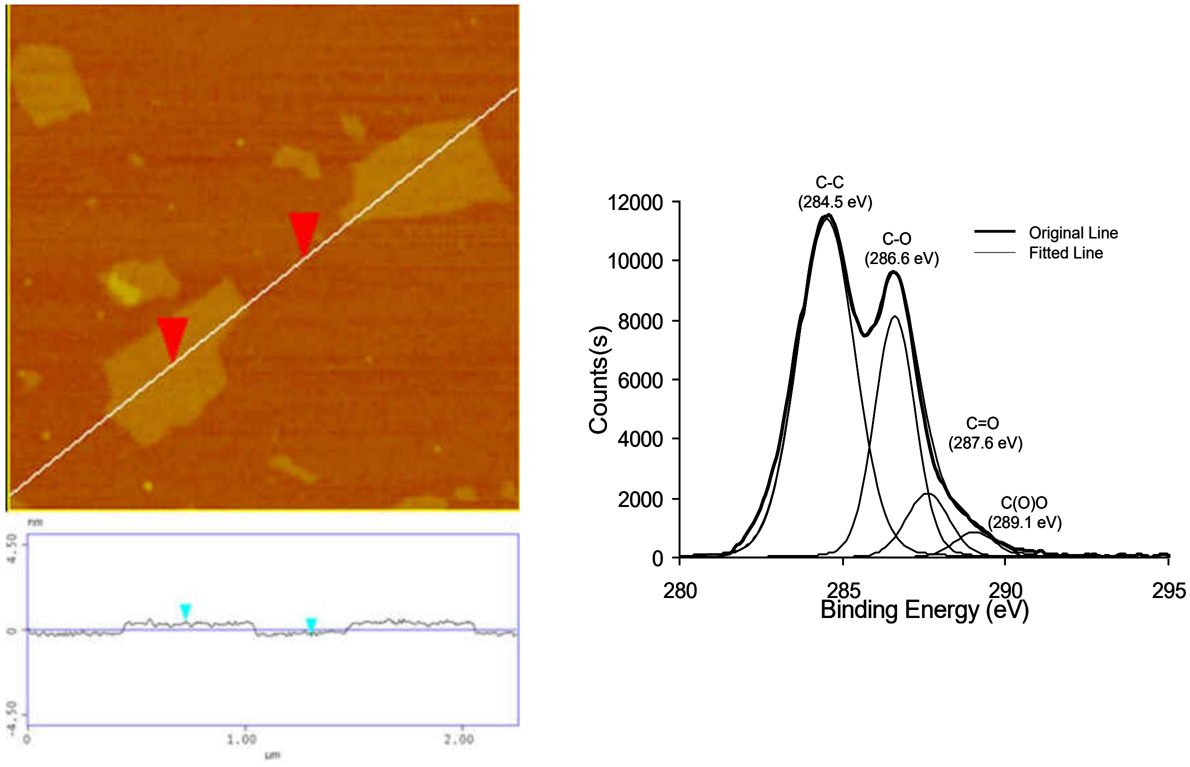

(a) (b)

Figure 3.1 (a) AFM image of GO monolayers with the thickness of 1 nm (b) XPS spectrum of GO

The chemical composition of GO was examine using XPS (Kratos Axis 165 Manchester, UK) in Figure 3.1 (b). The XPS spectrum of GO indicated considerable degree of oxidation with four components that corresponded to carbon atoms in different functional groups: non oxygenated ring carbon C (284.5 eV), C in C-O bond (286.6 eV), carbonyl C (287.6 eV) and carboxylate carbon (O-C=O, 289.1 eV). The results correspond to the similar findings by Dreyer et al. (Dreyer et al., 2010).

3.2.2 Material Preparation

GO used in the cement composite is presented in Figure 3.2. It has dark brownish appearance and is highly viscous in nature.

Figure 3.2: Graphene Oxide represented by brownish color viscous fluid

3.2.3 Mix Proportions and Casting of Specimens

Two dosages-0.01% and 0.05% GO (by the weight of cement) are mixed with cement and water. As the quantity of GO is much lower compared to the weight of cement, the water associated with GO has negligible effect on the w/c ratio of the specimens. Three different batches are prepared among which all the three batches contain cement and water while the second and third batches contain 0.01% and 0.05% GO, respectively. Casting was carried out based on the relevant tests which included compressive strength, flexural tests and microstructural characterization tests.

Experimental work plan for GOCC specimens are shown in Figure 3.3.

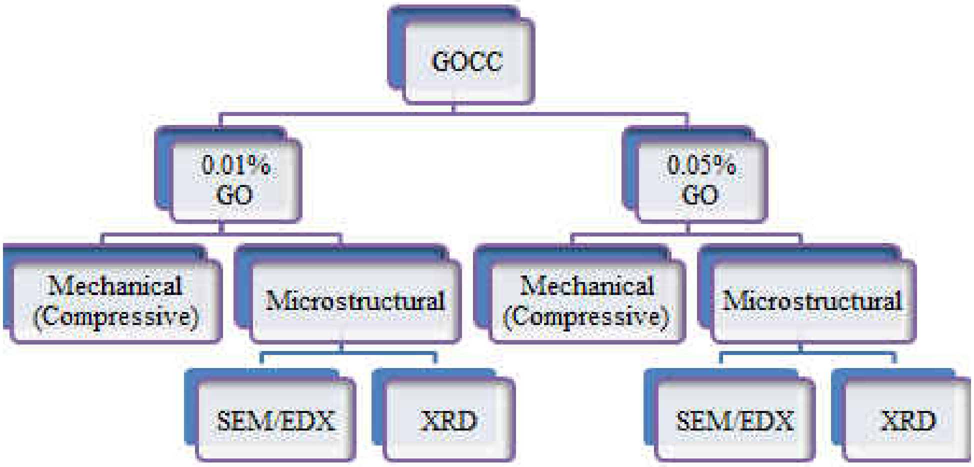

Figure 3.3: Work plan for GOCC specimens

Cement, GO and water is used in a mixing bowl. Kitchen Aid® sand mixer with 6-speed is used for the mixing process according to ASTM C305 (ASTMC305, 2013). Electronic Analytical Balance from DigiWeigh with a precision of 0.0001 g was used to measure the quantity of GO to be used in cement paste. GO dispersed in water and water, casted specimens and demolded cement composite cubes are shown in Figure 3.3.

(a)

(b)

(c)

Figure 3.4: Mixing of cement composite, (b) GOCC specimens after mixing, (c) GOCC specimens with 0.01% GO at demolding after 24 h.

3.2.4 Curing Regime and Testing Conditions for Mechanical, Microstructural and Electrical Conductivity Tests

The cast GOCC specimens were kept under airtight cover for 24 h to ensure the containment of moisture within the specimens according to ASTM C192 (13). The specimens were then demolded and kept fully submerged in water for curing until the appointed time for the tests, which, in this case is 3, 7, 14, and 28 d for compressive strength tests, and 3 and 28 d for material characterization tests i.e., SEM and XRD tests.

3.2.5 Specimen Preparation and Testing

Compressive strength is used as mechanical property tests performed in this study. Specimens were casted in 33mm^3 cubes and then tested on the selected test days after water curing. The specimens for compressive strength tests were taken out from the water curing condition after 3, 7, 14 and 28 d of curing, wiped with clean dry clothes and kept for 30 minutes before testing. Three specimens were tested on each test days and averaged to get the final compressive strength. Compressive strength tests were performed according to ASTM C109 (C109, 2013).

Pieces of broken specimens approximately 8mm-by-6mm in size were taken out after the flexural strength tests on 3 and 28 d. The specimens were immersed under acetone for 48 hours to inhibit the continued hydration process followed by 24 h of oven drying at 105±5°C. The specimens were kept into airtight test tubes under vacuum condition for SEM characterization tests.

Similar to specimen preparation for SEM tests, broken pieces were collected and kept under acetone for 48 hours which are followed by 24 h of oven drying condition around 105±5°C. The specimens were then taken out from the oven cooled and grinded by pestle which passes through 45µm sieve according to ASTM C1365 (ASTMC1365, 2011) to prepare for XRD powder tests.

3.2.6 Mechanical Property Tests

The minute details (Figure 3.4) of the compressive strength tests were carried out according to ASTM C109. (C109, 2013).


(a) (b)

Figure 3.5: Compressive Strength Tests (a) performed of GOCC specimens performed by MTS, (b) broken shards of GOCC specimens showing agglomeration of GO on some locations

3.2.7 Microstructural Tests

3.2.7.1 FESEM & EDX

Specimens prepared for the SEM tests were coated with Au-Pd Sputter coating before characterizing by ZEISS ULTRA-55 SEM equipment, other wisely known as Field Emission SEM or FESEM. It was ensure beforehand that no dust particles contaminate the surface of the specimen, otherwise the dust particles will contaminate the cathode chamber and the travelling electrons through the cathode ray tube will be dispersed by the dust particles and no meaningful visual observations will be possible (Goldstein et al., 2007). Working distance was set as 12 mm for the specimens for imaging and observations are made using several magnifications such as 500X, 2000X, 5000X, 10000X, and 20000X. For EDX analysis, the WD was revert to 10 mm. Chemical analyses on several distinctive points are carried out by EDX spectrum associated with the SEM instrument. A typical flowchart of the specimen preparation in the SEM chamber and its' outcome are shown in Figure

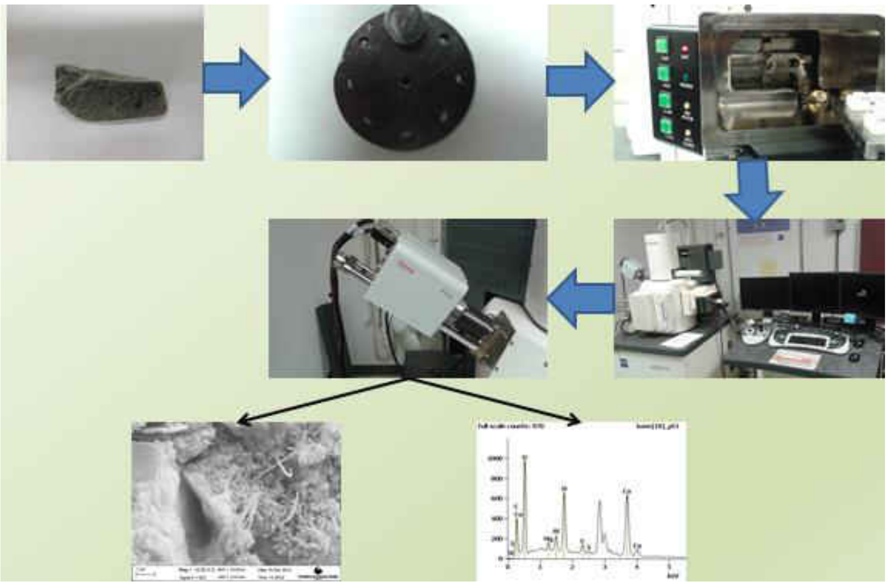

Figure 3.6: Sample preparation and assimilation for GOCC/rGOCC specimens in FESEM chamber

3.2.7.2 XRD

Rigaku D/MAX XRD II is used for peak pattern analyses and phase identification of the specimens. CuKα radiation with wavelength 1.54501Å is used as the source X-ray for the testing. To acquire appropriate phases, diffraction angle, $2\theta=5\sim80°$ and step size of 0.05 have been chosen. Quartz specimen was used for the calibration of the goniometer.

Test conducted for GOCC are listed in the Table 3.1.

Table 3.1: Specimen details with tests conducted for GOCC/rGOCC specimens

Tests	Test days	Size of the specimens	Curing regime	Testing Apparatus/Methods
Compressive strength	3,7,14,28 d	29 mm^3 cubes	Fully submerged in water until test day	MTS
Flexural Tests	7,14,28 d		Fully submerged in water until test day	MTS
Microstructural Tests (0.01% and 0.05%)	7, 28 d	6 mm-8 mm pieces	Submerged in water→48 hours under acetone→24 h in OD at 105℃	FESEM, EDX
Microstructural Tests (0.01% and 0.05%)	7,28 d	Powder< 45µm	Submerged in water→48 hours under acetone→24 h in OD at 105℃ →Grinding	XRD

3.3 Materials Used for Reduced Graphene-Oxide Cement Composite (rGOCC) Specimen

3.3.1 Materials and Tests

3.3.1.1 Cement

Ordinary Portland cement (OPC) confirming to ASTM C150 (Type II) is used as primary binding material in casting of cement composite. Water/cement ratio for casting of cement composite is 0.50 by the weight of cement.

3.3.1.2 Reduced Graphene Oxide (GO)

rGO is pitch black in color and viscous as GO. Dry rGO is similar to powdered lead of pencils. The work schedule for rGOCC specimens are shown below (Figure 3.7).

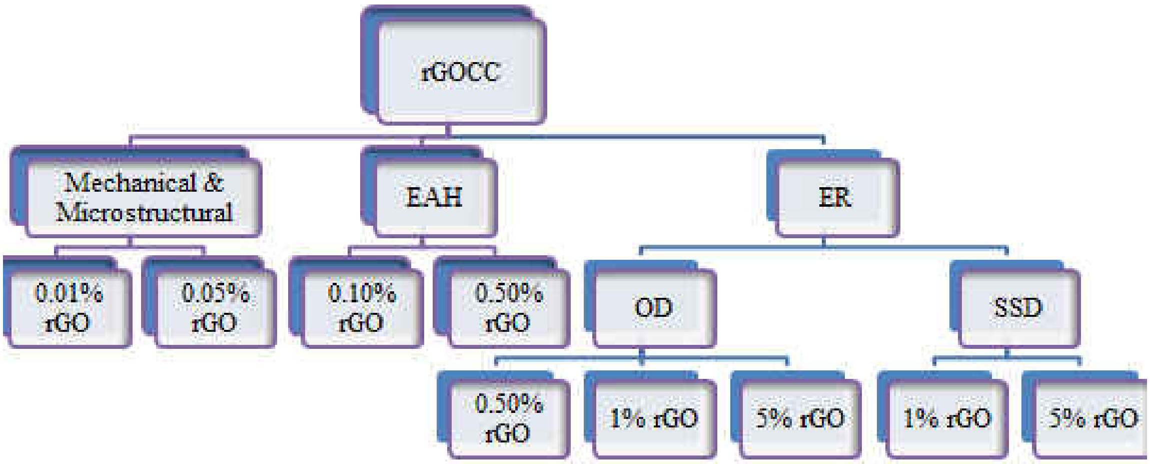

Figure 3.7: Work schedule for rGOCC specimens

3.3.2 Material Preparation

rGO was prepared by reduction of functional groups from GO basal plane using hydrazine. 1 mg of rGO was dispersed in 1 mL of maker making 1mg/mL solution concentration.

3.3.3 Mix Proportions and Casting of Specimens

3.3.3.1 Mechanical Property Tests

Similar to GOCC, 0.01% and 0.05% rGO (by the weight of cement) are mixed with cement and water. As the quantity of rGO is much lower compared to the weight of cement, the water associated with GO has negligible effect on the w/c ratio of the specimens. Three different batches are prepared among which all the three batches contain cement and water while the second and third batches contain 0.01% and 0.05% GO, respectively. Casting was carried out based on the relevant tests which included compressive strength, flexural tests and microstructural characterization tests.

Cement, rGO and water is used in a mixing bowl. Kitchen Aid® sand mixer with 6-speed is used for the mixing process according to ASTM C305 (ASTMC305, 2013). Electronic Analytical Balance from DigiWeigh with a precision of 0.0001 g was used to measure the quantity of rGO to be used in cement paste.

3.3.3.2 *Electrical Resistivity Tests*

Three different concentrations, 0.5%, 1%, and 5% rGO are used in the rGOCC for ER tests followed by 7 d of curing. rGO are mixed with cement with 0.50 w/c ratio in 0.4 cm^3 molds, and then tested as follows (Figure 3.8).

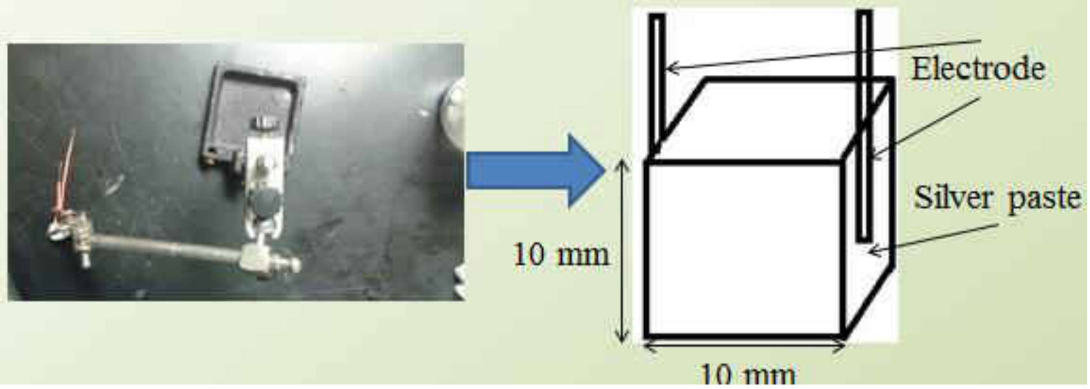

Figure 3.8: Preparation of rGOCC for Electrical Resistivity

3.3.3.3 *Early Age Hydration Tests*

It has been studied that nanomaterials such as carbon nanotubes, nanofibers, and others alter the early age hydration behavior of cement paste. On this note, two different concentrations-0.10% and 0.50% rGO are mixed with cement to cast rGOOC specimens to evaluate early age hydration characteristics of cement composite with the incorporation of rGO. EAH tests are carried out using FESEM/EDX and XRD tests.

3.3.4 Curing Regime and Testing Conditions for Mechanical, Microstructural and Electrical Conductivity Tests

rGOCC specimens were kept under airtight cover for 24 h to ensure that the moisture within the specimens cannot evaporate according to ASTM C192 (13). The specimens were then demolded and kept fully submerged in water for curing until the appointed time for the tests, which, in this case is 3, 7, 14, and 28 d for compressive strength tests, 7, 14 and 28 d for flexural tests and 3 and 28 d for material characterization (microstructural) tests i.e., SEM and XRD tests.

The specimens were demolded from the mold after 7 d of curing and put into oven-dried condition for 24 h at approximately 105±5°C. By following the procedure of Zhang et al. (Zhang et al., 2008) silver paste was applied on the surface of the specimens and kept for approximately 20 minutes to form a good contact with electrode. DC bias voltages of 0.1V, 1V and 10 V are applied on both sides of the specimens. FESEM/EDX and XRD analysis was performed on the specimens to correlate the microstructure of the specimens with the resistivity behavior.

Six specimens were prepared for 15min, 1 h, 3 h, and 24 h of testing time with 1% rGO in the cement composite. After the stipulated time of curing, the specimens underwent similar procedures as microstructural tests for GOCC and rGOCC. The specimens were then taken out from the oven and put inside airtight plastic bags for SEM tests and airtight vial for XRD tests.

3.3.5 Specimen Preparation and Testing

Compressive strength and flexural strength tests are used as mechanical property tests performed in this study. Specimens were casted in 33mm^3 cubes and then tested on the selected test days after water curing. The specimens for compressive strength tests were taken out from the water curing condition after 3, 7, 14 and 28 d of curing, wiped with clean dry clothes and kept for 30 min before testing. Three specimens were tested on each test days and averaged to get the final compressive strength. Compressive strength tests were performed according to ASTM C109 (C109, 2013).

Pieces of broken specimens approximately 8mm-by-6mm in size were taken out after the flexural strength tests on 3 and 28 d. The specimens were immersed under acetone for 48 hours to inhibit the continued hydration process followed by 24 h of oven drying at 105±5°C. The specimens were kept into airtight test tubes under vacuum condition for SEM characterization tests.

Similar to specimen preparation for SEM tests, broken pieces were collected and kept under acetone for 48 hours which are followed by 24 h of oven drying condition around 105±5°C. The specimens were then taken out from the oven cooled and grinded by pestle which passes through 45μm sieve according to ASTM C1365 (ASTMC1365, 2011) to prepare for XRD powder tests.

3.3.6 Mechanical Property Tests

The minute details of the compressive strength tests were carried out according to ASTM C109. (C109, 2013). Flexural tests on rGO composites are performed according to ASTM C78 (C78, 2015).

3.3.7 Microstructural Tests for Mechanical Properties

3.3.7.1 FESEM & EDX

Specimens prepared for the SEM tests were coated with Au-Pd Sputter coating before characterizing by ZEISS ULTRA-55 SEM equipment, other wisely known as Field Emission SEM or FESEM. It was ensure beforehand that no dust particles contaminate the surface of the specimen, otherwise the dust particles will contaminate the cathode chamber and the travelling electrons through the cathode ray tube will be dispersed by the dust particles and no meaningful visual observations will be possible (Goldstein et al., 2007). Working distance (WD) was set as 12 mm for the specimens for imaging and observations are made using several magnifications such as 500X, 2000X, 5000X, 10000X, and 20000X. For EDX analysis, the WD was revert to 10 mm. Chemical analyses on several distinctive points are carried out by EDX spectrum associated with the SEM instrument.

3.3.7.2 XRD

Rigaku D/MAX XRD II is used for peak pattern analyses and phase identification of the specimens. CuKα radiation with wavelength 1.54501Å is used as the source X-ray for the testing. To acquire appropriate phases, diffraction angle, $2\theta=5\sim80°$ and step size of 0.05 have been chosen. Quartz specimen was used for the calibration of the goniometer.

3.3.8 Microstructural Tests for Electrical Properties

3.3.8.1 FESEM & EDX

For SEM tests of ER properties on rGOCC specimens, 0.40 mm^3 cubes were broken into pieces and several pieces were submerged under acetone for 48 h before taking out and putting into oven for 24 h at 105±5 ℃. After removing from oven, the samples were kept into vials until the actual test in FESEM and EDX. Three sets of specimens were prepared for SEM tests for 0.5%, 1%, and 5% rGO contents. For, SSD conditioned specimens, the specimens are removed from the curing container, wiped, chunks are cut-off from the specimens, and kept into airtight vials for SEM tests. Details of the specimen condition and specification can be consulted from Table 3.1

3.3.9 Specimen Preparation for Early Age Hydration Tests

3.3.9.1 FESEM & EDX

Six specimens were prepared for 15min, 1 h, 3 h, and 24 h of testing time with 0.1% and 0.5% rGO in the cement composite. After the stipulated time of curing, the specimens underwent similar procedures as microstructural tests for GOCC and rGOCC. The specimens were then taken out from the oven and put inside airtight vials for SEM tests and XRD tests.

Specimens prepared for the SEM tests were coated with Au-Pd Sputter coating before characterizing by ZEISS ULTRA-55 SEM equipment, other wisely known as Field Emission SEM or FESEM. It was ensure beforehand that no dust particles contaminate the surface of the specimen, otherwise the dust particles will contaminate the cathode chamber and the travelling electrons through the cathode ray tube will be dispersed by the dust particles and no meaningful visual observations will be possible (Goldstein et al., 2007). Working distance was set as 12 mm for the specimens for imaging and observations are made using several magnifications such as 500X, 2000X, 5000X, 10000X, and 20000X. For EDX analysis, the WD was revert to 10 mm. Chemical analyses on several distinctive points are carried out by EDX spectrum associated with the SEM instrument.

3.3.9.2 XRD

The collected specimens for SEM were taken out from the oven and grinded passed 45µm for powder XRD tests. The powdered specimens were kept in different airtight vials for different test times.

Rigaku D/MAX XRD II is used for peak pattern analyses and phase identification of the specimens. CuKα radiation with wavelength λ=1.54501Å is used as the source X-ray for the testing. To acquire appropriate phases, diffraction angle, 2θ=5~80° and step size of 0.05 have been chosen. Quartz specimen was used for the calibration of the goniometer.

3.3.9.3 Temperature Measurement during Early Age Hydration

Heat evolution is inherent in cement hydration due to the exothermic reactions of C_3S and C_2S cement phases with water. Temperature measurement profile is one of the indirect indications of heat profile of cement hydration within certain duration. As a result a temperature data-logger (Figure 3.5) is used to measure temperatures of rGOCC samples with a range of rGO concentrations, usually for first 24 hours.

(a) (b)

Figure 3.9: (a) Electrode immersed in cement paste for measuring temperature, (b) T1 electrode showing the air temperature whereas T2 stipulates the temperature inside the cement paste at a particular hydration time.

CHAPTER 4 RESULTS AND DISCUSSIONS

4.1 Introduction

In this chapter, mechanical properties of GOCC and rGOCC are presented followed by microstructural investigations using FESEM and XRD. In FESEM is used to study to topographic analyses of GOCC and rGOCC. Chemical analyses are carried out by EDX. Phase identification and crystal structures are determined with XRD. ER characteristics of rGOCC are investigated experimentally followed by microstructural investigation of the composite to bring forth the correlation between the network of rGO and electrical conductivity. Finally, EAH properties of rGOCC are investigated from at the age of 15 min, 1 h, 3 h and 24 h up using FESEM and XRD.

4.2 Mechanical Properties of GO-Cement Composite

Compressive strength tests were conducted to evaluate the effect of GO on the mechanical behavior of GO cement composite. As shown in Figure 4.1 (a), compressive strength of GOCC-0.05% specimens reached up to 22.7 MPa at 28 d compared to 18.2 and 17.6 MPa for GOCC-0.01% and control specimen, respectively, showing 29% and increment in strength over the control specimen (cement paste) and GOCC-0.01%, respectively. After 3 d, GOCC-0.05% and GOCC-0.01% specimens showed 24% and 16% increment, respectively in strength compared to the cement paste specimens. Although GOCC-0.01% exhibited higher strength compared to the control specimen, as hydration continues, the strength gain diminishes and after 28 d GOCC-0.01% shows only 3.4% increase. On the other hand, the compressive strength of GOCC-0.05% continued to increase until 28 d. The density of

GOCC specimens increased with GO content as shown in Figure 4.1 (b). This can be attributed to the filling of nanopores by GO sheets.

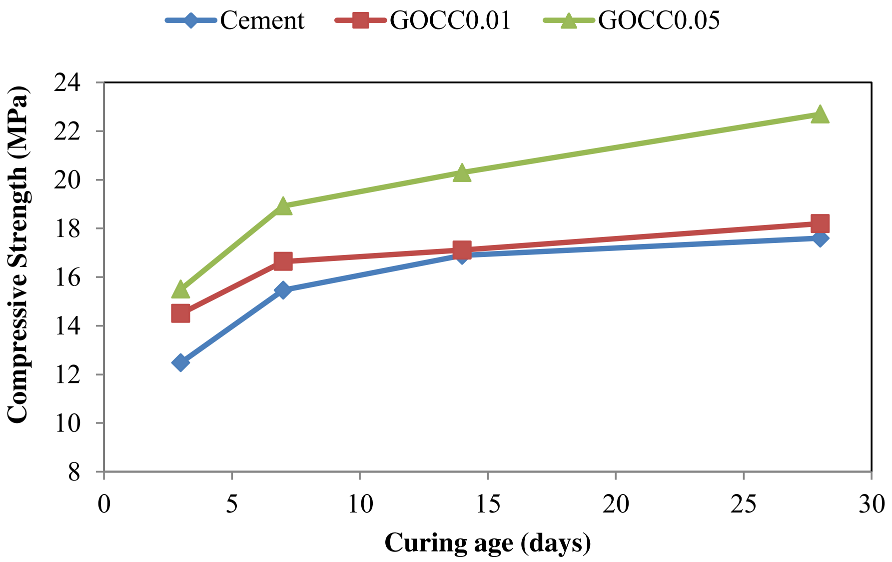

(a)

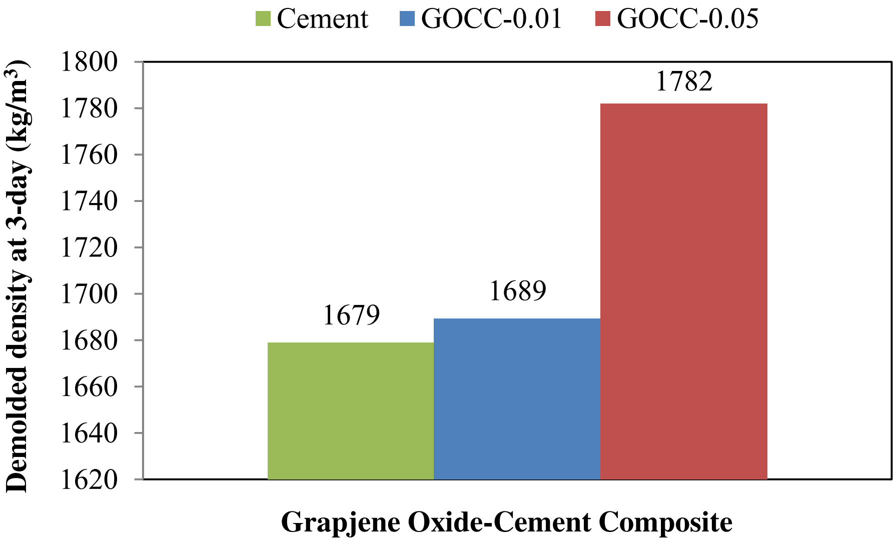

(b)

Figure 4.1: (a) Compressive Strength, (b) Demolded density of GOCC-0.01% and GOCC-0.05%

The strength increase in GOCC specimens can be the consequence of two distinctive contributions: 1) "crack bridging" effect, and 2) heterogeneous nucleation. First, GO sheets act as the bridging agent between the cracks created during the compressive strength testing

(Rafiee et al., 2013a). GO is well known for its high Young’s modulus and intrinsic tensile strength capacity (Liu et al., 2012). Eventually, as cracks are developed and propagated, GO sheets may hold them together resulting in higher strength which is introduced as “crack bridging (Chandler et al., 2010, Banthia and Nandakumar, 2003, Banthia and Sheng, 1996). Second, as CNTs acts as heterogeneous nucleation sites in cement paste, it is believed that GO can act as same manner (Sedaghat et al., 2014). If the GO sheets in cement paste also act as heterogeneous nucleation sites, the activation energy of hydration reactions decreases and the reaction rates increases, which, eventually produces more C-S-H and portlandite rapidly (Sedaghat et al., 2014). When activation energy decreases, it will take less effort to produce sTable nuclei of same critical radius compared to the homogeneous nuclei (Porter et al., 2009). For example, it will take less effort to produce same grain size for GOCC-0.05% or GOCC-0.01% specimens compared to cement paste specimens. GOCC-0.05% specimens have more GO sites compared to either GOCC-0.01% or control specimens, which may explain its higher strength. The fracture patterns of GOCC specimens in the following Figure 4.2 dictates the tortuous path of crack propagation.

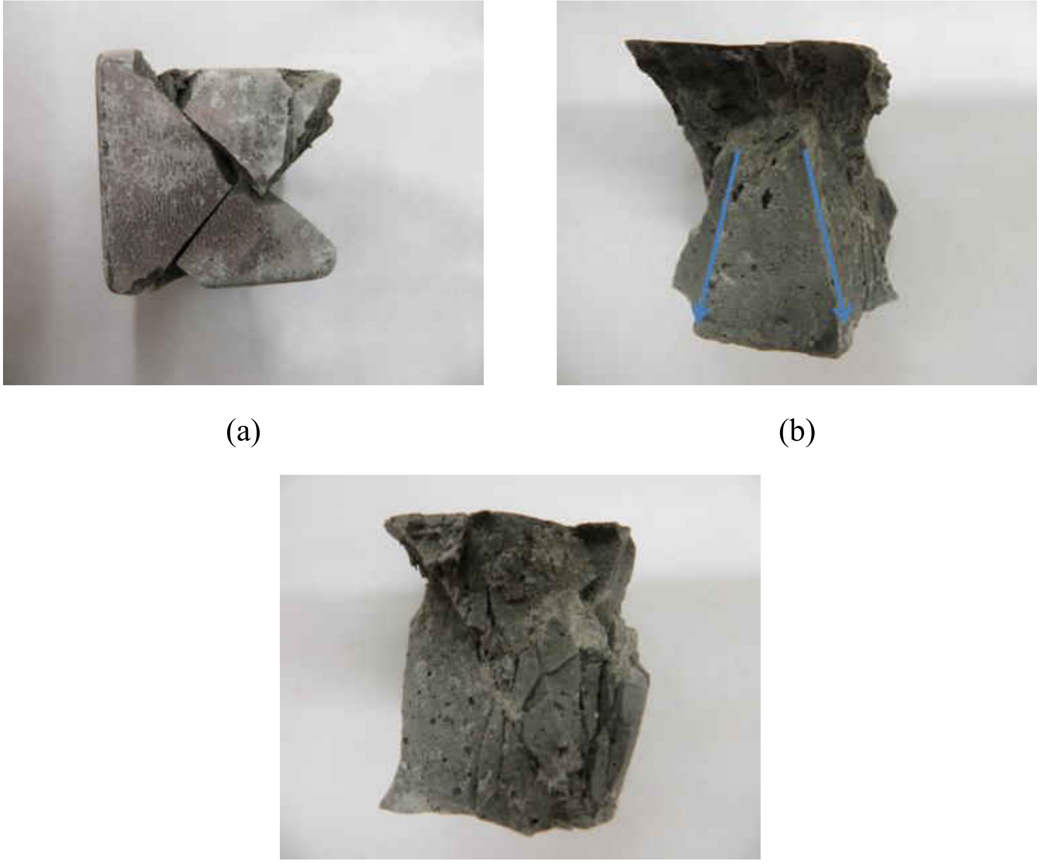

(a) (b)

(c)

Figure 4.2: (a), (b) and (c) Fracture pattern of GOCC with 0.05% GO content

4.3 Mechanical Properties of rGO-Cement Composite

4.3.1 Compressive Strength

Compressive strength increased by 5.46% for rGOCC-0.01% specimen compared to plain cement paste after 3 d of hydration. rGOCC-0.05% specimen showed 17% increased after same duration. After 28 d of hydration, rGOCC-0.01% specimens showed 7% increment for same duration of hydrated cement pastes; however, rGOCC-0.05% showed 21% increase in compressive strength. It is also evident that rGOCC-0.01% did not start off with very high early strength compared to cement paste whereas rGOCC-0.05% was almost 400 psi higher in compressive strength.

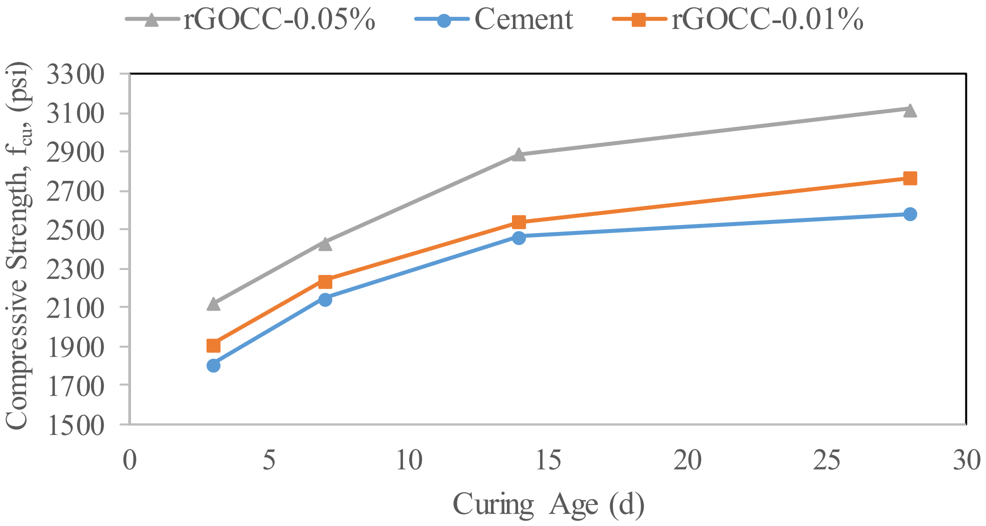

Figure 4.3: Compressive strength variation for rGOCC-0.01% and rGOCC-0.05% specimens

Compressive strength of cement increased 42% after 28 d of hydration compared to its' value from 3 d. On the other hand, strengths for rGOCC-0.01% and rGOCC-0.05% increased 44% and 47%, respectively for the same duration, indicating the rate of compressive strength increment for rGO composites are also higher than that of cement. Although increase in compressive strength is evident for rGOCC specimens, it was lower than compressive strength developed by GOCC specimens, indicating that the decrease in reactive functional groups for rGOCC specimens might be responsible for lowered strength.

4.3.2 Flexural Strength

Figure 4.4 below demonstrates the typical setup for 3-point bending test (Flexural strength test) of rGO-cement specimens according to ASTM. The contact point between the load cell and the specimen was in the center of the specimen.

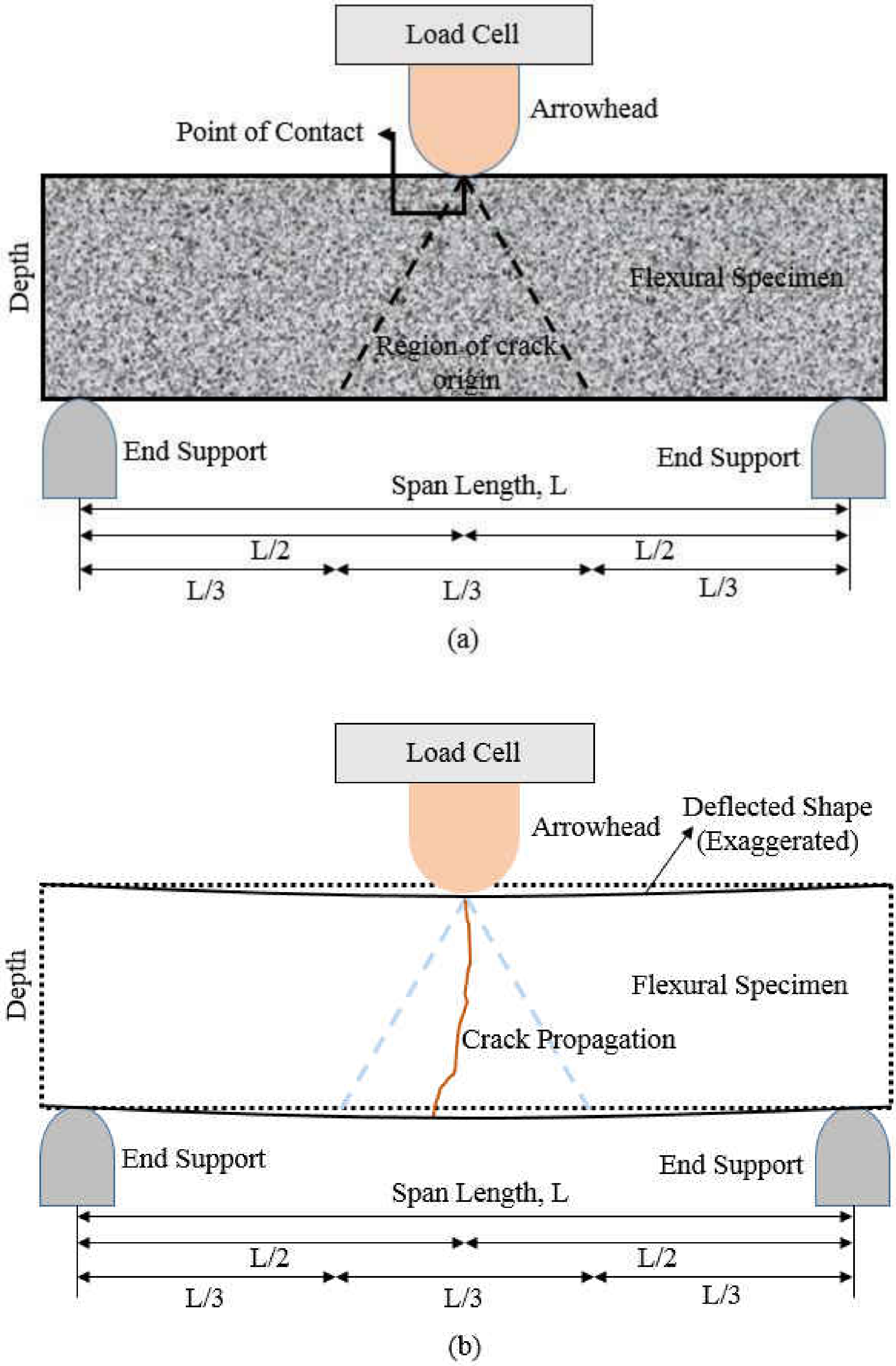

Figure 4.4: (a) Test setup for 3-point bending tests for GOCC/rGOCC specimens, (b) Specimen condition after the test

Crack propagation was found out to be within the middle third part (designated by the L/3 in Figure 4.3) of all the specimen after the bending test.

Loading rate was calculated using the following formula (Equation 4.1),

$$r = \frac{Sbd^2}{L} \tag{4.1}$$

Here, r= loading rate, lb/min,

S= rate of increase in maximum stress on the tension face, psi/min,

b=average width of the specimen as oriented for testing, in,

d=average depth of the specimen as oriented for testing, in,

L= span length, in.

Modulus of rupture of the tested specimen was calculated using,

$$R = \frac{PL}{bd^2} \tag{4.2}$$

Here, R= modulus of rupture, psi,

P=maximum applied load indicated by the testing machine, lbf,

L= span length, in,

b= average width of the specimen at fracture, in,

d= average depth of the specimen at fracture, in.

The following Table 4.1 and Figure 4.4 represent the modulus of rupture with the curing age for rGO specimens. rGOCC-0.01% specimens showed 0.35% increase in flexural strength over the control specimen after 28 d. But, rGOCC-0.05% showed 15.5% increase in flexural strength compared to the control specimen. rGOCC-0.01% and rGOCC-0.05% specimens showed a total of 114 psi and 129 psi of increase in strength from 3 d to 28 d of hydration as opposed to only 76 psi of increase showed by cement paste.

Table 4.1: Calculation of flexural strength (indicated by modulus of rupture) of rGOCC specimens

Specimen	Test day	Specimen 1 Load (lbf)	Specimen 2 Load (lbf)	Average Load, P (lbf)	Modulus of Rupture, f_r (psi)	Standard Deviation, s
Cement	7	353	326	339.50	744.31	10.26
	14	386	355	370.50	813.10	11.78
	28	381	396	388.50	827.07	5.70
rGOCC-0.01%	7	327	353	340.00	716.90	9.88
	14	382	404	393.00	832.98	8.36
	28	378	411	394.50	830.30	12.54
rGOCC-0.05%	7	355	477	416.00	828.69	46.36
	14	409	481	445.00	917.90	27.36
	28	422	513	467.50	956.05	34.58

Figure 4.4 clearly showed that the rate of increase in flexural strength for rGOCC-0.05% during curing period was higher than those of either rGOCC-0.01% or cement paste.

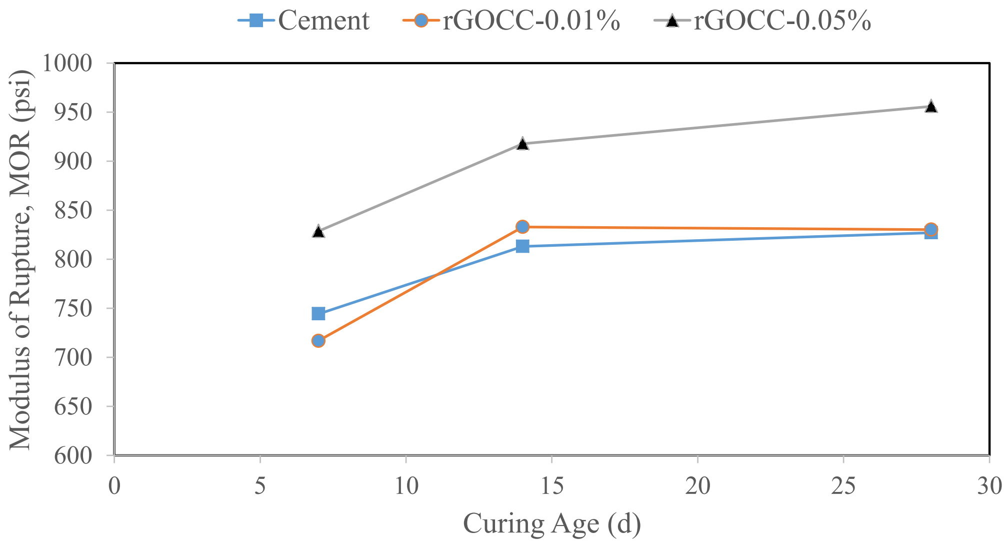

Figure 4.5: Modulus of rupture of rGOCC-0.05% with curing age

Both cement paste and rGOCC-0.01% specimens showed little standard deviation/(s) in flexural strength. In contrast, rGOCC-0.05% showed higher standard deviation indicating probably high degrees of uncertainty associated with the strength development by high rGO content in cement paste. As the rGO content increased, so did the porosity of the specimens which were indicated by the lower density of the specimens compared to the plain cement paste specimens. Although rGO can act as filler material and decrease the pores, the wrinkled surfaces and twisting/folding capability of rGO sheets (similar to the GO sheets) supposedly can result in pores inside the cement paste which can increase the porosity. Hence, this pores can alter the local strength development of the cement paste, leading to the local failure of the specimens during the loading test, hence higher standard deviation occurs.

Both rGOCC-0.01% and rGOCC-0.05% showed no variation in temperature at 21.3℃ data in Figure 4.5 until 1.8 h when the accelerating period started. But rGOCC-0.1% showed higher temperature (22.7℃) although the acceleration period for this specimen also started approximately at 1.8 h. the acceleration period lasted from 1.8 h to 10 h for rGOCC-0.01% specimen. For rGOCC-0.05% and rGOCC-0.1%, the acceleration period lasted until ~11.11 h. Both rGOCC-0.01% and rGOCC-0.05% showed same slope for temperature increment. But, rGOCC-0.1% specimens showed steeper slope compared to both rGOCC-0.01% and rGOCC-0.05% indicating higher rate of nucleation and growth in the acceleration period. The rGOCC-0.1% specimens showed peak at 11.11 h after hydration started followed by start of deceleration period. For, rGOCC-0.01% specimen, the deceleration period started ~1 h earlier. The temperature deceleration curve was also steeper for rGOCC-0.1% specimen compared to other two sets of specimens. The three curves met at 16.8 h after hydration, after which, the temperature curve of rGOCC-0.1% fell below rGOCC-0.1%. The temperature curve of rGOCC-0.1% became flat at 20 h and continued to progress as flat curve without any variation even after 24 h. On the other hand, curves for rGOCC-0.1% and rGOCC-0.5% specimens dropped below that of rGOCC-0.1% and continued to become flatter at 24 h.

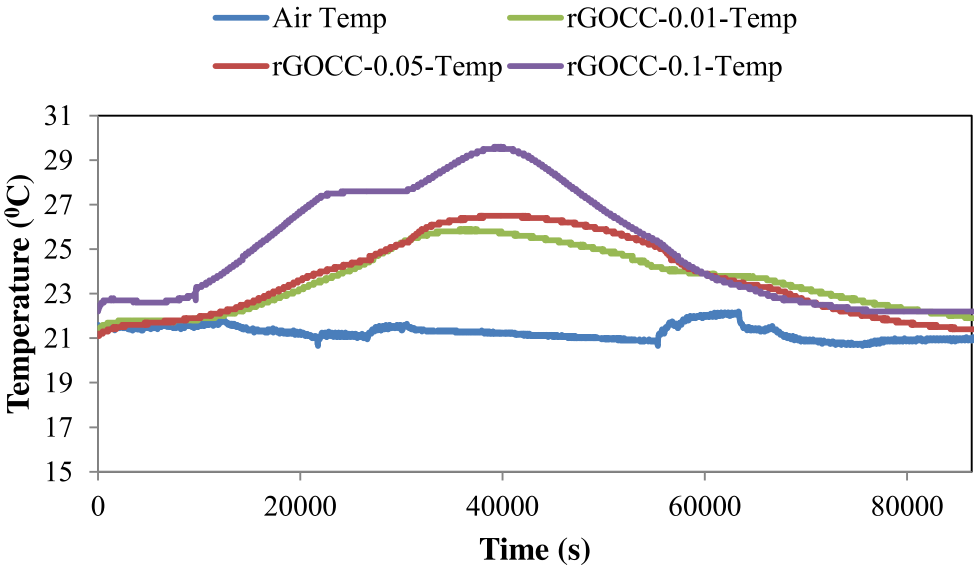

Figure 4.6: Evolution of internal temperature of rGOCC specimens with different concentrations for first 24 h of hydration

4.4 Microstructural Characterization of GO-Cement Composite

4.4.1 FESEM & EDX

Microstructural characterization techniques such as SEM, EDX and XRD were used to examine the conditions for increasing strength shown by GOCC specimens. Figure 4.7 (a) shows the overall surface morphology of a GOCC-0.05% specimen at 500X magnification. A closer magnification of 2500X (Figure 4.7 (b)) reveals several platy like crystals, GO sheets, needle like ettringite and early age morphologies of C-S-H. Figures 4.7 (c) and 4.7 (d) reveal the structures of the grains and crystals with higher magnifications. Needle-shaped ettringite can be clearly seen from Figures 4.7 (c) and 4.7 (d) protruding into the pores. GO is observed to bridge the cracks in Figure 4.7 (e) which is able to explain the increase in compressive strengths. Amorphous morphology of C-S-H is clearly evident from Figure 4.7 (d) One important thing to be noted here is that the EDX analysis shows the evidence of Al in C-S-H with the usual elements Ca, Si, O. XRD analysis (next section) also shows the evidence of tobermorite peak which is in agreement with the SEM/EDX analysis of C-S-H.

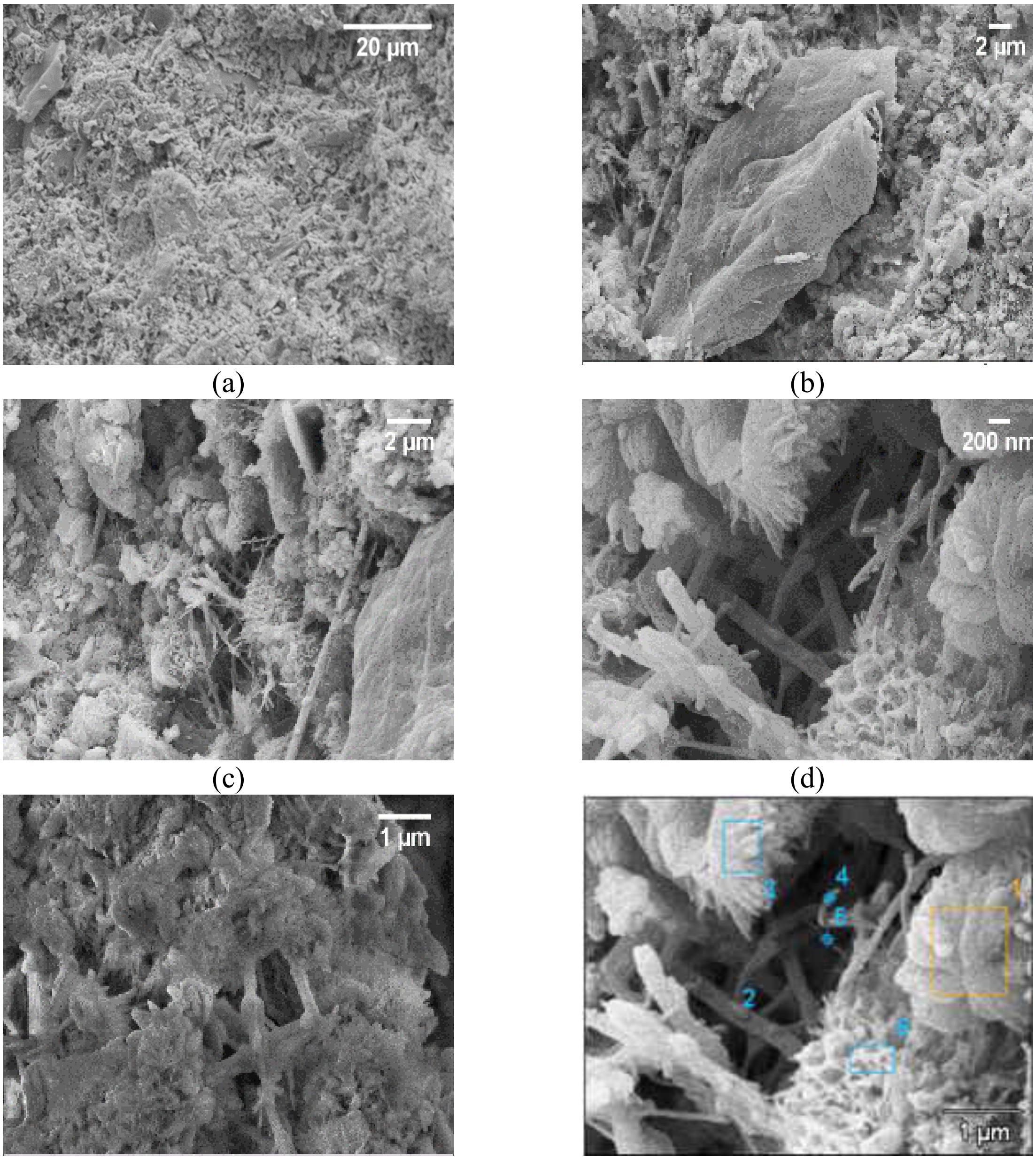

(a) (b) (c) (d) (e) (f)

Figure 4.7: Low magnification SEM image of GOCC-0.05% surface at 3-day; (b) high magnification SEM shows the distribution of different crystals; (c) & (d) SEM shows higher magnifications of different crystals and their distribution through the pores; (e) SEM shows crack bridging mechanism by GO, (f) point and area to be shot for EDX analysis.

Figure 4.7 (c), (d) and (e) shows the needle-shaped ettringite crystals. Crack bridging by GO is evident from Figure 4.7 (e). Figure 4 (e) shows the evidence of GO bridging the crack gap in cement paste. Figure 4.7 (f) shows the different spots on which the EDX analysis is performed. Actual snapshot of SEM and EDX data can be found in Appendix C.

Area shot is made on point 1 in Figure 4.7 (f) which indicates the presence of C-S-H. Table 2 refers to the chemical analysis of elements on 6 different shots on Figure 4.7 (f) in atom % (at. %). Point 2 may refer to the needle like ettringite or AFt phase with the presence of Al, S and Ca. Area 3 detects the presence of high amount of O and C including Si, Al and Ca which may refer to the substitution of Si by Al in jennite found from XRD analysis (see section 4.4.2). The presence of GO coated with jennite like C-S-H formations can be observed from area 3. Ca/Si ratio of 2.5 directly pointed out the presence of jennite in area 3. Point shots on 4 and 5 reveals the presence of Ca, S, Al and Si which may refer to Area 6 is another evidence of C-S-H lumps on the surfaces of unhydrated cement grain. Presence of Pd and Au are attributed to the surface coating of the specimen. SEM and EDX analysis focus on the evidence and distribution of the nucleated products due to the hydration of GOCC. From the SEM analysis, it appears that GO sheets mostly bridge the cracks between the cement matrices. EDX analysis reveals the presence of Ca, Si, Al and S which are essential elements for the formation of different forms of C-S-H. The evidence of the elements found by EDX analysis are bolstered by XRD data which also reveals the crystallite sizes of these hydration products in the later sections. The chemical analysis of the point and area shots is summarized in Table 4.2.

Table 4.2: Chemical analysis of GOCC-0.05% at 3 d of hydration by EDX

Shots	C	O	Al	Si	S	Ca	Pd	Au	Total %	Probable Compounds
	at. %									
1(Area)	12.43	30.05	---	3.17	---	50.93	---	3.42	100	C-S-H
2(Point)	5.29	31.98	4.39	6.82	4.63	46.89	---	---		C-S-H+Ettringite
3(Area)	15.56	39.99	0.86	10.15	---	25.74	4.56	3.15		Jennite+GO
4(Point)	---	13.70	2.58	9.23	5.47	69.01	---	---		Ettringite
5(Point)	---	7.29	1.58	12.91	2.35	75.87	---	---		Ettringite
6(Area)	16.94	39.34	---	8.38	---	26.00	5.62	3.72		C-S-H+GO

4.4.2 XRD

Major phases such as alite (C_3S), belite (C_2S), celite (C_3A) and ferrite/brownmillerite (C_4AF) are present in the cement powder used for this study as shown in Figure 4.8 (a) which are in agreement with the NIST guidelines (Stutzman, 1996). Gypsum ($CaSO_4.2H_2O$) can be also evident in XRD pattern analysis which is essential for nucleation of ettringite upon hydration. Because of the powder nature of specimen, the major phases can be located overlapping each other on several diffraction angles, for instance, d-spacings are so close to each other for these phases that the peaks seem to overlap.

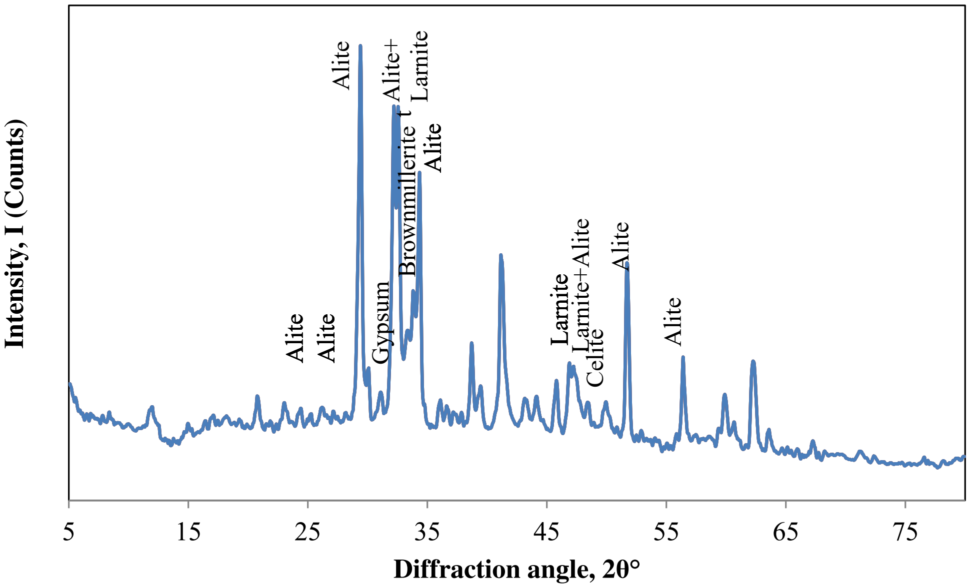

(a)

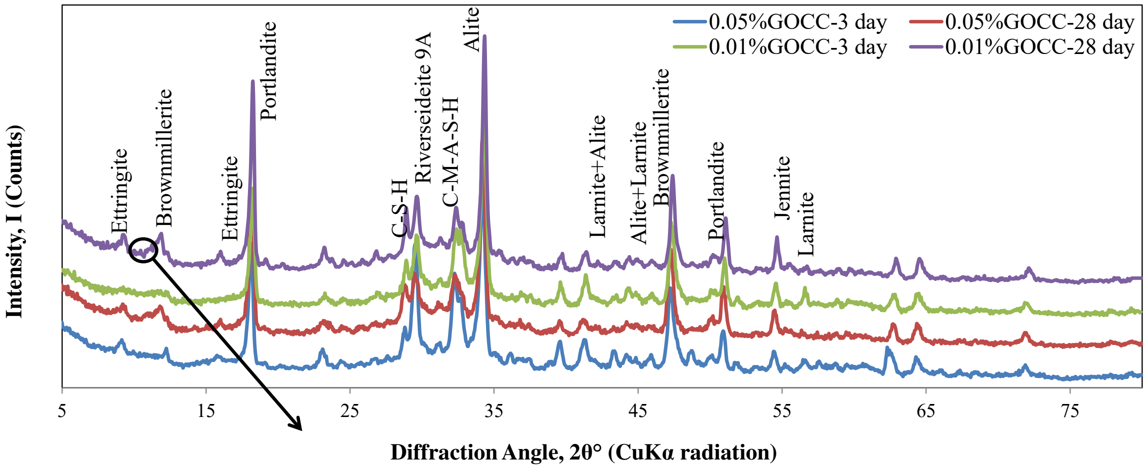

(b)

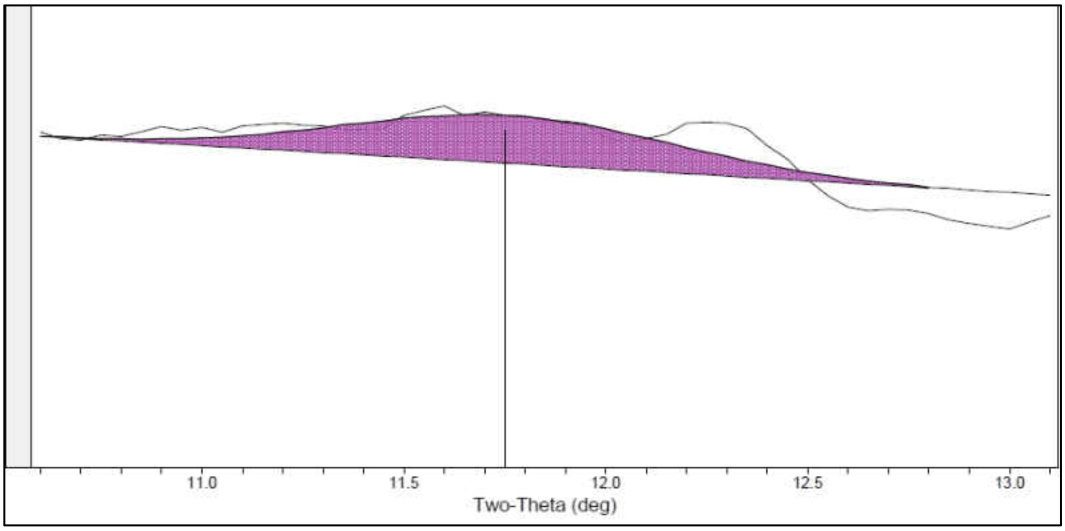

(c)

Figure 4.8: (a) XRD pattern showing different phases of unhydrated cement, (b) Different hydration products after 3 d and 28 d of hydration of GOCC with w/c of 0.50 (c) Closer magnification of GO showing diffraction peak at 11.78°

Figure 4.8 (b) demonstrates the evidence of all major hydration products for GOCC-0.01% and GOCC-0.05% after 3 d and 28 d of hydration (Referring to Appendix D). Ettringite is found in all the specimens as characterized by XRD. The peaks of ettringite are observed at exactly 9.24° (2θ) with a d-spacing of 9.56Å which is similar to the findings of Antao et al. (Antao et al., 2002). The d-spacing of GO is observed to be 7.5 Å as shown in

Figure 4.8 (c) and Table 4.3 which is higher than that of graphite flakes because of the functional groups and intercalated water molecules protruding outwards from the 2D sheet. From the shape and positions of the peaks, it is also evident that some phases are strain free and some phases are experiencing either tensile or compressive strains. Regardless of the manner of the strain, it is conclusive that some forms of residual stress are associated with the material prior to the hydration process.

It is to be noted that large hexagonal portlandite crystals can be found in all the specimens. The sharp and narrow peaks indicate that the crystallite sizes of portlandite are larger than some of the other crystals in the powder sample. Unhydrated alite, belite/larnite, brownmillerite are also present in the GOCC specimens. Belite (C_2S) has numerous polymorphs among which β polymorph of C_2S or larnite is prominent in cement paste. For this reason, belite will be termed as larnite in this paper. However, the absence of celite means either all celite reacted with gypsum and produce ettringite, or the relative intensity of celite peak is so small compared to the other major peaks such as those of portlandite or alite that it is not identifiable by XRD.

Although amorphous C-S-H is not distinguishable from background noise by XRD analysis, ordered crystalline portion of the jennite can be evident. Tobermorite-9Å is one of the other forms of C-S-H. C-M-A-S-H peak indicates that some of the Si(s) in the tetrahedra are also subjected to substitution by Al and Mg because of their almost similar atom size and valency. Some of the major phases of cement such as alite, larnite, C-S-H, portlandite etc. show multiple peaks which indicate the abundance of the phases in cement powder. This evidence from XRD also explains the presence of Al from the SEM/EDX analysis in the vicinity of GO.

Table 4.3: Generic Phase Identification of GOCC after Hydration at 3 and 28 d by XRD

Compound	Chemical Formula	Crystal Structure	Peak Position 2θ°	d-spacing (Å)	Miller Indices (h k l)
Ettringite	$Ca_6Al_2(SO_4)_3(OH)_{12}.26H_2O$	Hexagonal	9.24	9.56	1 0 0
Graphene Oxide	C-C and other groups	Hexagonal	11.78	7.5	0 0 1
Brownmillerite	$Ca_2(Al,Fe)_2O_5$	Orthorhombic	47.17	1.92	2 0 2
Portlandite	$Ca(OH)_2$	Hexagonal	18.24	4.85	0 0 1
			50.97	1.79	1 1 0
Tobermorite-9Å (Riversiderite)	$Ca_5Si_6O_{16}(OH)_2$	Orthorhombic	29.61	3.01	1 1 1
Alite (C_3S)	$3CaO.SiO_2$	Triclinic	34.28	2.19	$4\ 0\ \bar{4}$
Larnite (β-C_2S)	$2CaO.SiO_2$	Monoclinic	41.28	2.19	1 3 0
C-M-A-S-H	$54CaO.16SiO_2.Al_2O_3.MgO$	Monoclinic	29.55	3.02	5 1 5
			32.36	2.76	1 1 1 0
			32.66	2.74	9 1 4
Gypsum	$CaSO_4.2H_2O$	Monoclinic	29.57	3.01	2 0 0
Al tobermorite	$Ca_5Si_5Al(OH)O_{17}.5H_2O$	Monoclinic	28.87	3.09	$\bar{2}\ 2\ 1$
Jennite	$Ca_9H_2Si_6O_{18}(OH)_8.6H_2O$	Triclinic	54.52	1.68	$\bar{4}\ \bar{1}\ 5$

It is well studied that jennite (Richardson, 2004) and tobermorite-9Å (Subramani, 2008) in Table 4.3 are two different forms of C-S-H having monoclinic crystal structures. Tobermorite-9Å may indicate loosing of water molecules upon heating at 105±5°C whereas jennite is believed to be always present in cement paste with the lapse of time (Janakiram Subramani, 2008). The corresponding crystal structures, d-spacings and diffraction angles of these two forms of C-S-H are summarized in Table 4.3. However, as it can be seen in Table 4.4, that the Full Width at Half Maximum (FWHM) increases for jennite in GOCC-0.01% and GOCC-0.05% specimens from 3 d to 28 d of curing. For GOCC-0.01%, FWHM decreases from 0.272 to 0.238, indicating an increase in crystallite size as hydration continues. On the other hand, GOCC-0.05% specimen is showing a decrease in FWHM from 0.313 to 0.289 indicating also an increase in crystallite size. However, on both 3 d and 28 d, FWHMs of GOCC-0.05% are higher than those of GOCC-0.01%. On 3 d of hydration FWHM of GOCC-0.05% is 0.313 compared to 0.272 for GOCC-0.01%. It indicates that GOCC-0.05% specimens have much finer particles compared to GOCC-0.01% specimens.

Table 4.4: FWHM and crystallite size calculation of jennite and tobermorite based on curing age by XRD analysis

Compound	Days	Samples			
		GOCC-0.01%		GOCC-0.05%	
		FWHM°	Crystallite (Å)	FWHM°	Crystallite (Å)
Jennite	3	0.272	353	0.313	301
	28	0.238	416	0.289	329
Tobermorite-9Å	3	0.671	125	0.839	100
	28	0.300	293	0.660	127

Tobermorite-9Å is also demonstrating similar pattern in the change of FWHM upon hydration. As hydration continues, the crystallite sizes for tobermorite-9Å have grown from 3 d until 28 d. However, GOCC-0.05% specimens show finer crystallite sizes compared to GOCC-0.01% in the case of tobermorite-9Å also. Finally, the crystallite size calculation from Scherrer Equation (Cullity, 1956) agrees with the results reported from FWHM analysis for both the C-S-H phases (Cullity, 1956). The growth of jennite and tobermorite-9Å are represented schematically in the Figure 4.9.

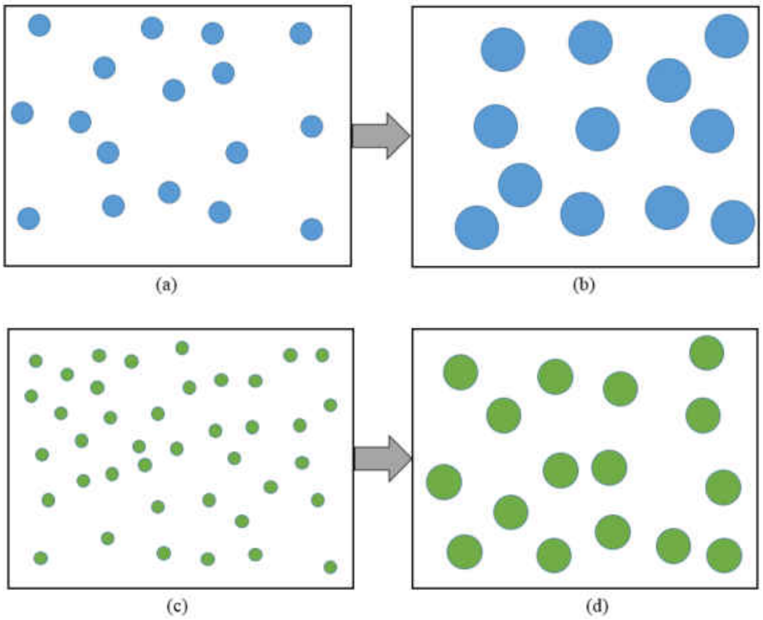

Figure 4.9: Crystallite sizes and growth of (a) GOCC-0.01%-3d, (b) GOCC-0.01%-28d, (c) GOCC-0.05%-3d, (d) GOCC-0.05%-28d

It is known that fine grained particles show broad diffused peak in XRD analysis (Cullity, 1956). If chemical species analyzed by GO act as heterogeneous nucleation sites, the activation energy of formation of sTable nuclei of C-S-H, i.e. tobermorite-9Å and jennite would decrease, resulting in finer particles. Both specimens showed that crystallite sizes increased from 3 d until 28 d, which is evidently a growth process. Our hypothesis and findings seems to be in agreement with Thomas et al. where they provided C-S-H seeding in pure C_3S hydration and observed faster hydration rate during the nucleation and growth process in the early stages of hydration due to the formation of new nucleation sites (Thomas et al., 2009).

GOCC-0.05% specimens are associated large number of reactive functional groups of GO which leads to the availability of new nucleation sites with large number of reactive sites which leads to the. The FWHM & crystallite size directs towards the suggestion that due to this heterogeneous nucleation, jennite or tobermorite-9Å would require lower activation energy and critical radius, resulting in the nucleation of much finer particles.

If a material consists of finer particles generally demonstrates higher strength, toughness and hardness (Callister and Rethwisch, 2013, Abbaschian et al., 2008). Material with finer particles has larger GB areas that act as obstacles to slip dislocations causing dislocations to pile-up on the slip planes behind the boundary. The number of these dislocations tends to pile-up with increase in grain size. Moreover, the pile-ups produce stress concentration in the next grain to the grain that contains pile-ups. As a result, the stress multiplication in the coarse grained material (GOCC-0.01%) is much higher than fine grained (GOCC-0.05%) material. Much larger applied stress is necessary to cause slip in crystallites of GOCC-0.05% to pass through the grain boundary compared to the crystallites of GOCC-

0.01% (Abbaschian et al., 2008). These phenomena may dictate a reasonable explanation for the higher compressive strength shown by GOCC-0.05% compared to other batches.

4.5 Microstructural Characterization of rGO-Cement Composite

4.5.1 Topographic Analysis using FESEM

SEM images on the hydration characteristics of rGOCC-0.05% specimens at 7 d have been presented in Figure 4.10. Hydration products such as C-S-H can be seen agglomerated around the periphery of rGO sheet in Figure 4.10 (a). However, some nuclei of C-S-H can also be evident on the top surface of rGO even at 1K magnification. Interestingly, crack propagation can be seen held by smaller flakes of rGO along the sheared path of crack propagation which looks much more rigid than CNT-cement composite. Very few pores are evident in Figure 4.10 (a) that can occur because of the higher C-S-H production due to the higher number of nucleation seeds provided by the rGO sheets and pore-filling capability of rGO sheets themselves.

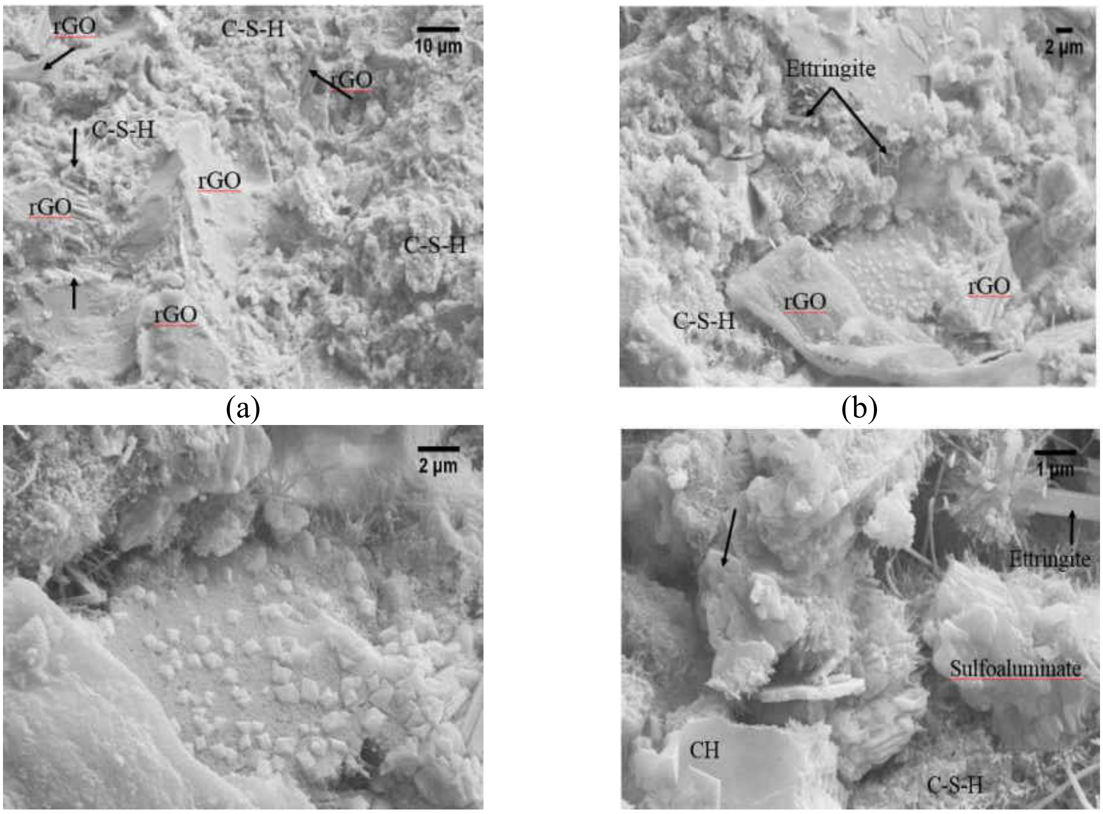

(a) (b)

(c) (d)

Figure 4.10: rGOCC-0.05% specimen after 7 d hydration where, (a) C-S-H network can be seen from low magnification in the pool of rGO sheets. Some rGO sheets bridging the cracks originated from the crack propagation path due to the stress build up in the specimen, (b) a closer look of the specimen shows various crystalline formations along with C-S-H and rGO, (c) hexagonal CH crystals are clearly evident in this image, (d) platy sulfoaluminates (AFm) resulting from the dissolution of ettringite (AFt) are evident.

Figure 4.10 (b) represents a higher magnification (2K) of rGOCC-0.05% specimen representing the C-S-H production on the left side of the image. Nucleation of certain crystals can be seen also in this image. Ettringite needles are also evident near the surface of the rGO sheets and also along the interfacial zone of C-S-H and rGO. More importantly, C-S-H can be seen growing from the surface of cement grains as well as from rGO sheets. No clear evidence of rGO sheets interpenetrating into each other or interconnecting to make a bonded network such as CNT-network is evident from the SEM images. rGO sheets are much larger in size, contrary to the CNT tubes whose aspect ratio is remarkably higher than that of rGO sheets. Hydration evolution of cement composites with rGO sheets can be depicted somewhat schematically as the following Figure 4.11.

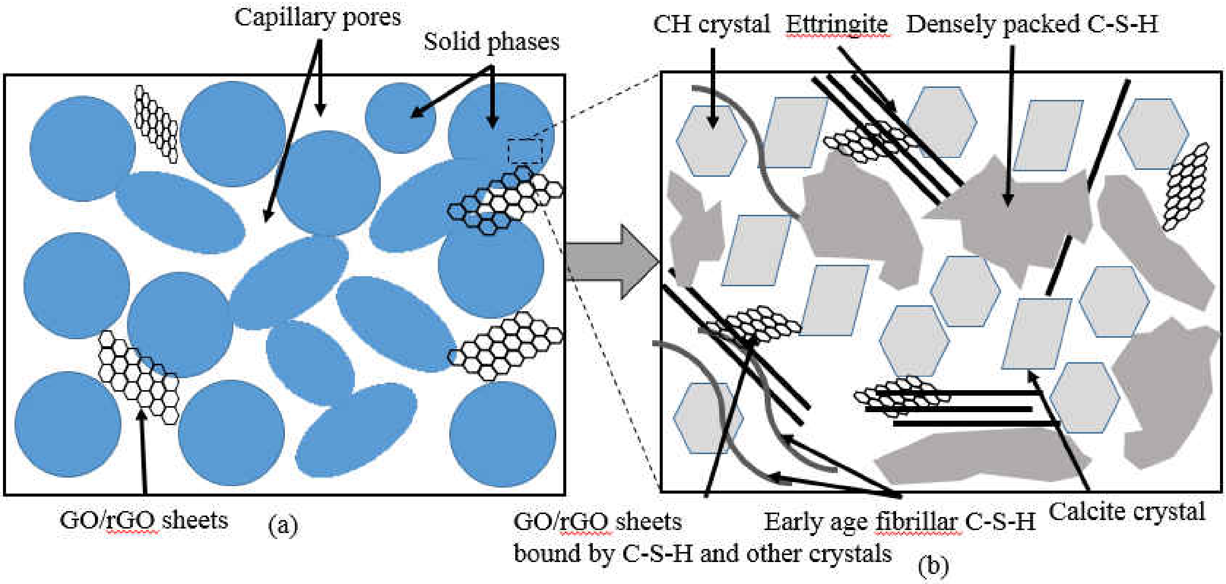

Figure 4.11: (a) Hydrated solid phases can be seen after cement-water interaction, rGO sheets are trapped inside the large capillary pores, (b) a higher magnification image of the solid phases are shown in this image showing various hydration products including all the main constituents evident from the SEM images

In the schematic diagram (Figure 4.11), the crystalline products are shown to be occupying the periphery of the C-S-H, which are clearly the norm in the SEM images of rGOCC-0.05%.

Nucleated C-S-H grains occupied the rGO surface whereas ettringite crystals are interconnected between C-S-H and rGO. Fibriller C-S-H possesses high surface area as seen in Figures 4.10 (c) and d. High flexural strength of rGOCC-0.05% specimens can be a directly interconnected to the fibriller C-S-H network. The structure of C-S-H resembles the structure proposed by Powers after observing TEM analysis by Richardson (Bensted and P.Barnes, 2002) that shows the Ca/Si ratio to be greater than 1.50. The following section shows that jennite peaks are evident from the XRD pattern of rGOCC-0.05%. It is reported by numerous researchers that jennites have Ca/Si>1.50 which acts as a cross-evidence of the validity of SEM analysis in this research work. Table 4.5 shows the proposed structures of C-S-H by various researchers. If the Ca/Si is around 2, the structure is be termed as C-S-H (II) by Chen et al., which is less ordered than jennite but more ordered that C-S-H gel. From this study, it can be said that the structure of C-S-H possibly resembled C-S-H (II). From the above (Chen et al., 2004) discussion and research findings from Chen et al. it is evident that C-S-H can be a mixture of tobermorite and jennite with jennite being the dominant one, and eventually, the sole C-S-H structure present. These research findings tend to concurrent with Chen's work.

Table 4.5: Models describing the structure of C-S-H proposed by various researchers

Models	Experimental validation	Author	Reference
Tobermorite gel		Brunauei (1962)	(Brunauer, 1962)
Tobermorite 14*Ȧ*Jennite	TGA, XRD	Taylor (1986)	(Taylor, 1986)
Hillebrandite	---	Dai and Post (1995)	(Dai and Post, 1995)
Tobermorite 14 *Ȧ*/Jennite	---	Cong & Kirkpatrick (1996)	(Cong and Kirkpatrick, 1996)
Tobermorite 11 *Ȧ*	---	Faucon et al. (1997)	(Faucon et al., 1997)
Tobermorite 11 *Ȧ*	---	Merlino et al. (2001)	(Merlino et al., 2001)
Refined Tobermorite 14*Ȧ* (Plombierite)	---	Bonaccorsi and Merlino (2005)	(Bonaccorsi et al., 2005)
Tobermorite 9 *Ȧ*,11 *Ȧ* and 14 *Ȧ*	---	Shahsavari et al. (2009)	(Shahsavari et al., 2009)
Tobermorite 14*Ȧ* and 11 *Ȧ*	---	Shahsavari et al. (2010)	(Shahsavari et al., 2011)
Tobermorite 9 *Ȧ*	---	Hamid (1981)	(Hamid, 1981)
Tobermorite/CH+ Tobermorite/Jennite	---	Richardson (2004)	(Richardson, 2004)
Tobermorite/Jennite	T:Ca/Si<1.5, J:Ca/Si>1.8	Chen et al. (2004)	(Chen et al., 2004)

In addition to C-S-H, hexagonal CH crystals 0.5µm-1µm in size nucleated and agglomerated on the unhydrated cement grains (Figure 4.10 (c)). Figure 4.10 (d) reveals a closer look about the hydration products of cement. Along with C-S-H grains, sulfoaluminate (AFm) products can also be evident protruding from the surface of C-S-H. Platy sulfoalumintes originated from the dissolution of ettringite crystals are certainly not a rarity in rGOCC-0.05% specimens. Sulfoaluminates can easily be distinguished from the ettringite and C-S-H due to their smooth jogged and plate-like surface. The sulfoaluminates are 1-2 µm in size and ettringite are 2-3 µm in length which are typical for these hydration products.

4.5.2 Chemical Analysis

Figure 4.12 showed the area from where the EDX analysis peaks were gathered. The Ca/Si ratio showed (Table 4.6) from the C-S-H are around 2.0 with some Al impurtity. Possibly, some Al replaced Ca in the interlayer Ca-O layer of the C-S-H.

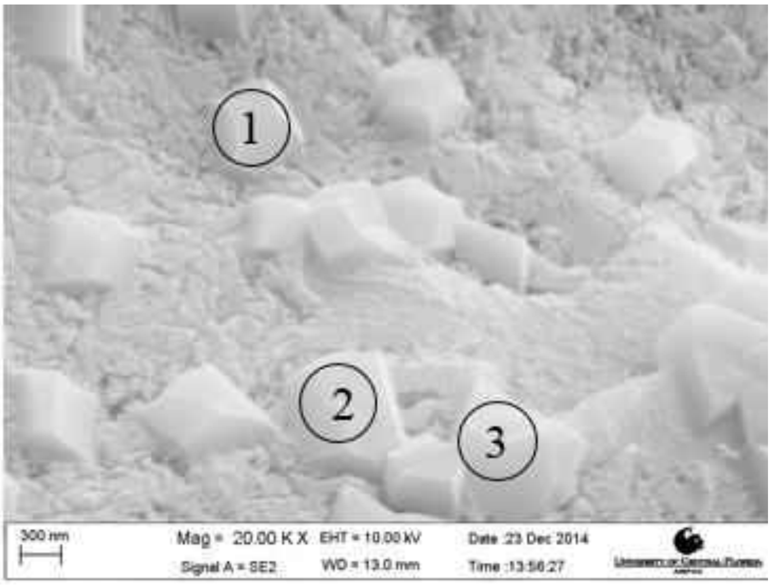

Figure 4.12: EDX analysis from the point shots are gathered from 1, 2 and 3 points

Table 4.6: Ca/Si ratio found in C-S-H of rGOCC-0.05% after 7 d of hydration

Shots	C-K	O-K	Al-K	Si-K	Ca-K	Ca/Si
Point 1	18.21	57.70	0.80	7.39	15.90	2.15
Point 2	15.42	31.96	3.38	16.08	33.16	2.06
Point 3	23.97	12.27	3.78	20.17	39.81	1.98

The EDX peaks of this analysis can be found in the Appendices.

4.5.3 Phase Identification, Crystal Structure Determination

XRD pattern evaluation of pristine rGO has been performed as shown in Figure 4.13. The XRD pattern has an amorphous hump in between 11.5° to 23° 2θ and a containing presumably carbon component peak is determined at 26.5° 2θ. The crystal structure information are summarized in Figure 4.13.

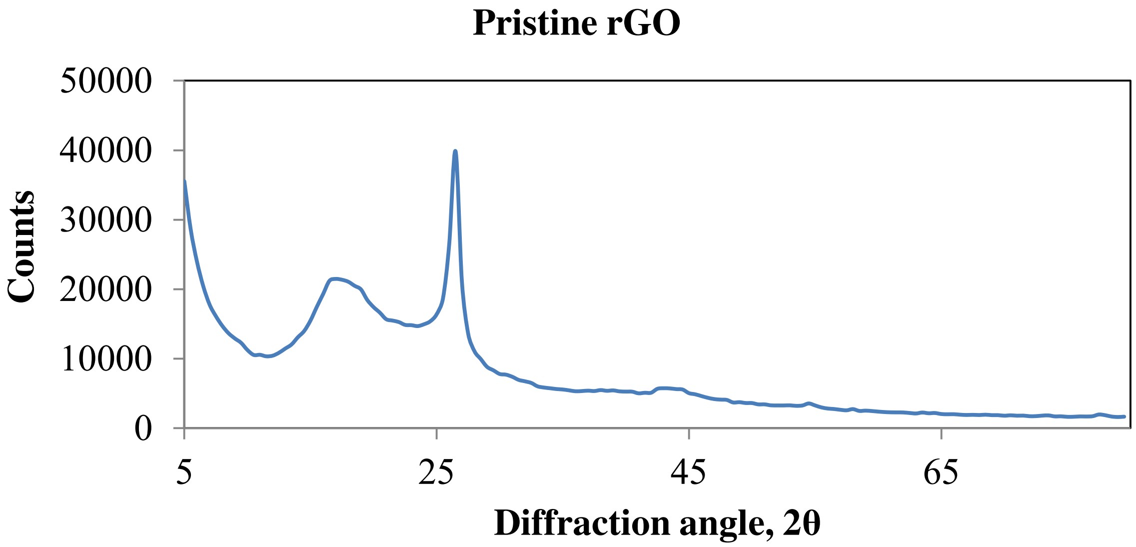

Figure 4.13: XRD pattern of rGO showing amorphous hump and a sharp peak around 26.5° Bragg angle.

It has been observed from the GOCC and rGOCC studies that GO had superior effects on the mechanical properties of cement paste at 0.05% concentration. To understand its' implications, in depth understanding of the structure of the two different C-S-H products-tobermorite and jennite has to be undertaken. GOCC specimens showed a mixture of tobermorite and jennite as its' production of C-S-H, whereas rGOCC specimens produced only jennite (disordered, to be exact). Ca/Si ratio of tobermorite is lower than that of jennite. As a result, tobermorite chain has more Ca in comparison to Si. It is well established that bond dissociation energy of Ca-O is lower than that of Si-O. So, if a structure has more Si-O bond, it presumably possesses higher strength, which is in fact the case for tobermorite. C-S-H (II) or disordered jennite, on the other hand, having Ca/Si ratio of 2.0, possesses more Ca-O bond in the interlayer than the number of Si-O bond, which dictates lower strength.

To summarize, GOCC, being a mixture of tobermorite and jennite, showed higher strength because of larger number of Si-O bond than rGOCC specimens which are built primarily of jennite having lower Si-O bond. The reason why rGO is blocking the nucleation of tobermorite is still unclear. The most probable reason can be, the atomic arrangements in the unit cell of jennite is such that it needed lower free energy of formation than that of tobermorite. However, of other parameters being equal for GOCC and rGOCC, there is plausible indication that rGO is responsible for producing more jennite in rGOCC and the interaction between rGO with cement paste to produce jennite might be better understood with the application of molecular dynamics (MD) or density function theory (DFT), which gives the free energy of formation of jennite.

4.6 Early Age Hydration Characteristics of rGO-Cement Composite

Figures 4.14 (a) and (b) showed overall topography of rGOCC-0.1% after only 15 min of hydration. Figure 4.14 (c) rGOCC 0.1%- after 15 min of hydration at 5K magnification showing GB along the grains, (d) nucleated C-S-H particles along the GB (10K magnification).

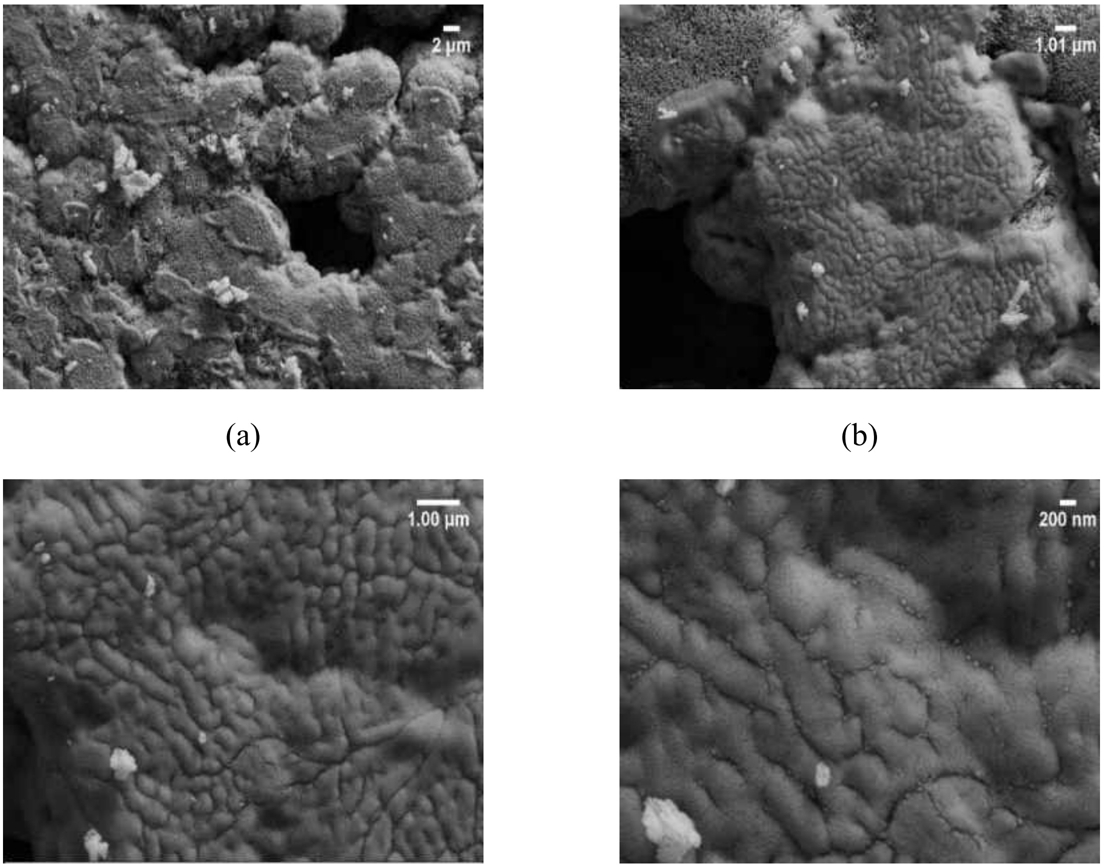

(a) (b)

(c) (d)

Figure 4.14: (a) represented undulations in the surface morphology of rGOCC-0.1% after 15 min of hydration at 500X magnification, (b) Two different regions of the composite surface can be encountered, (c) 5K magnification showing GB along the grains, (d) nucleated C-S-H particles along the GB (10K magnification).

These precipitates formed along the GB could be nuclei of C-S-H. Scherer (Scherer et al., 2012) hypothesized that cement hydration continued with nucleation and growth of C-S-H along the GB instead of randomly oriented nuclei. They showed analytically that the Boundary Nucleation Model (BNG) showed better fit with the calorimetric data of hydration compared to the JMAK model which assumed nucleation of C-S-H was random. The SEM image from this research work showed evidence of the nuclei of C-S-H about 5-20nm in size formed along the GB within minutes of hydration started. Bullard et al. (Bullard et al., 2011) also vouched the hypothesis of short burst of nucleation along the GB for cement hydration. This research tends to be concurrent with the past researchers in this aspect. The C-S-H that are forming along the GB can be safely said to be formed because of heterogeneous nucleation because of the lower activation energy required for formation of nucleation along GB defects (Porter et al., 2009).

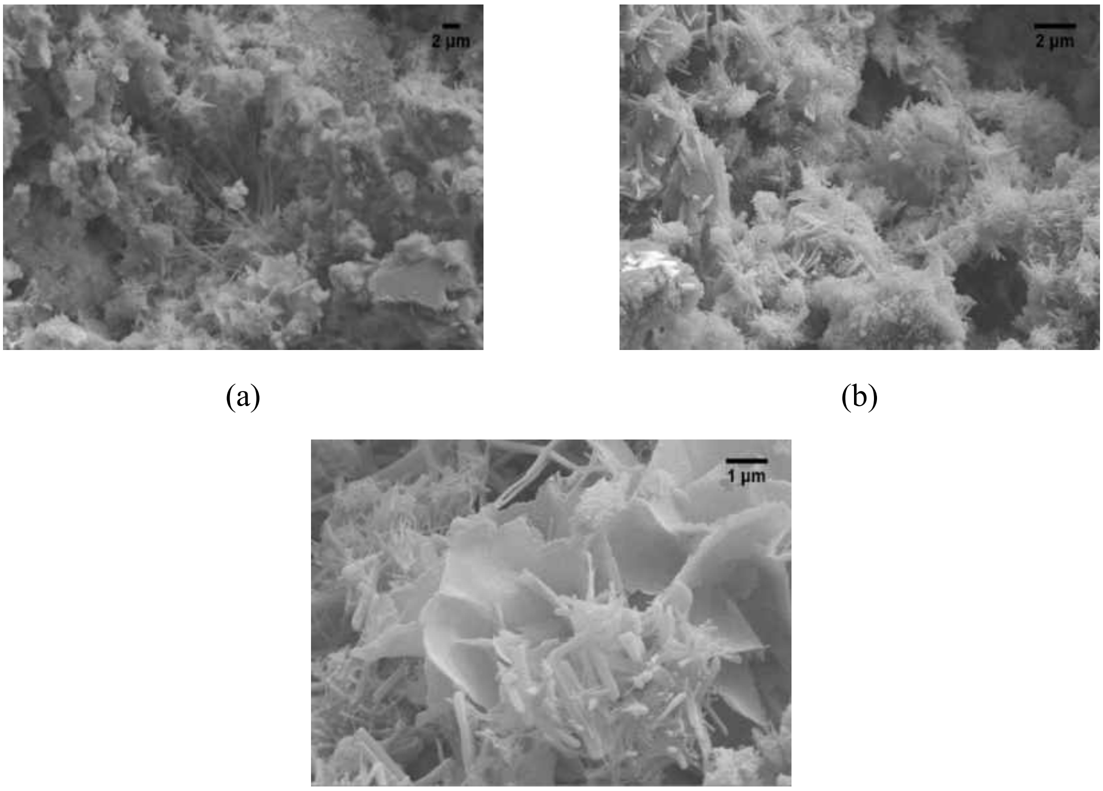

(a) (b)

(c)

Figure 4.15: (a) rGOCC-0.1% after 1h of hydration (2K), (b) 5K, (c) 10 K

Large difference can be evident between 1h and 15 min of hydration observing Figures 4.15 and 4.14, respectively. In Figure 4.15 (a), compacted C-S-H formed and filled up the pore spaces. In between the existing pore spaces, ettringite crystals and fibriller C-S-H can be seen. C-S-H formation can also be seen along the surfaces of unhydrated cement grains. Figure 4.15 (b) also showed high amount of C-S-H with large surface area. Some platy crystals can also be seen along with ettringite. The crystals resemble CH crystals in this image. Figure 4.15 (c) showed rGO sheets around 4μm in width with folding and twisting of the sheets. Ettringite crystals 2-2.5μm in length can be seen protruding from the surface of C-S-H. Despite of having high amount of C-S-H, pores and voids can also be evident.

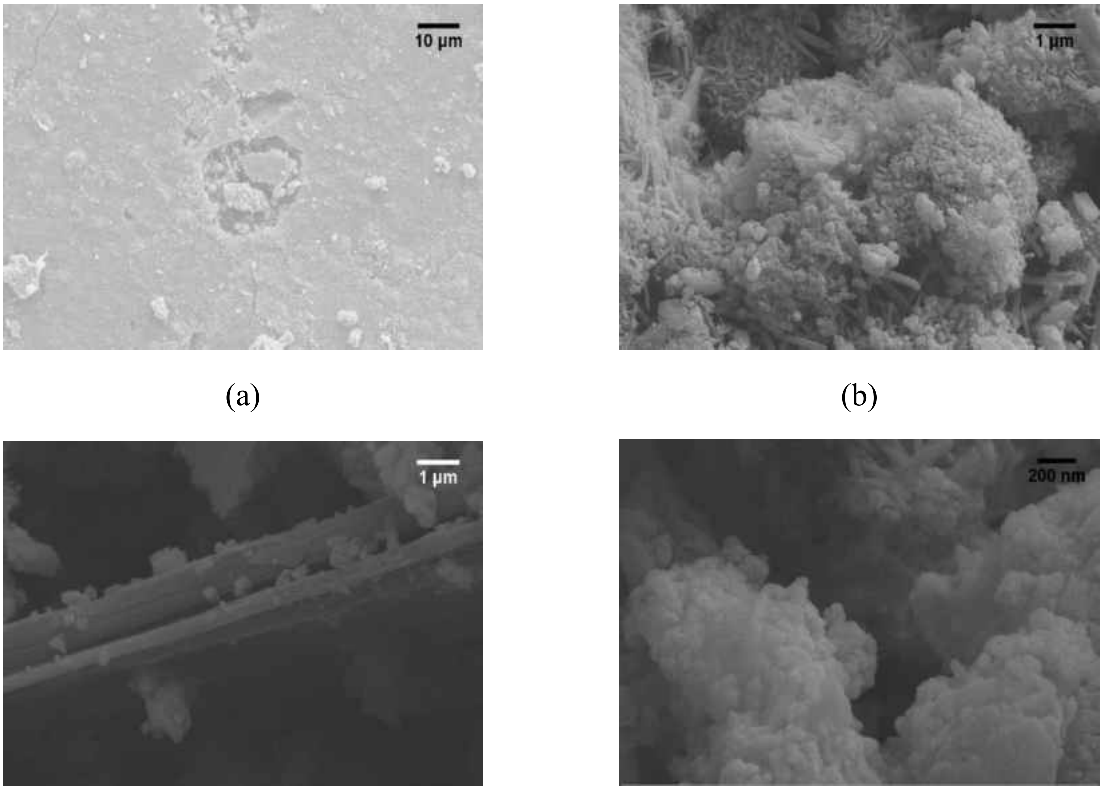

(a) (b)

(c) (d)

Figure 4.16: rGOCC-0.1% (a) hydration of rGOCC-0.1% 24 h (500X), (b) formation of large quantity of C-S-H (5K magnification), (c) ettringite 1 μm in width (5K magnification), (d) densely packed C-S-H (20K magnification)

All the above Figure 4.16 showed the gradual increase in the quantity of the C-S-H and its' corresponding surface area. Figure 4.16 (d) clearly depicts the dense C-S-H compared with the earlier version of fibriller C-S-H.

Figures 4.17 and 4.19 depicted the XRD pattern of rGOCC-0.1% and rGOCC-0.5% respectively. Ettringite was present in the Fig although significantly less in intensity compared to the other peaks. Brownmillerite (impure C_4AF) was also evident from the XRD pattern. CH peaks showed high rate of increase from 3 h to 24 h which indicates the accelerating period of hydration. During the accelerating period, large amount of C_3S reacts with water to form C-S-H and forms a byproduct of CH in the process. The reduction in the peak area of C_3S can also be seen at 29.40° 2θ from 3 h to 24 h. In fact, all the alite peaks were showing reduction in the peak area indicating the consumption of alite by the reaction and formation of C-S-H. Other major cement phases such as larnite (impure C_2S), C_3A and gypsum are also evident from the pattern. Monoclinic crystals of C_3S are also evident from the pattern. Gypsum peaks also had shown reduction in area from 1 h to 24 h. This can also be proven with the SEM images of rGOCC-0.1% when numerous formation of ettringite could be observed with progressive hydration age. Interestingly, jennite can also be found from the pattern which is one of the forms of C-S-H.

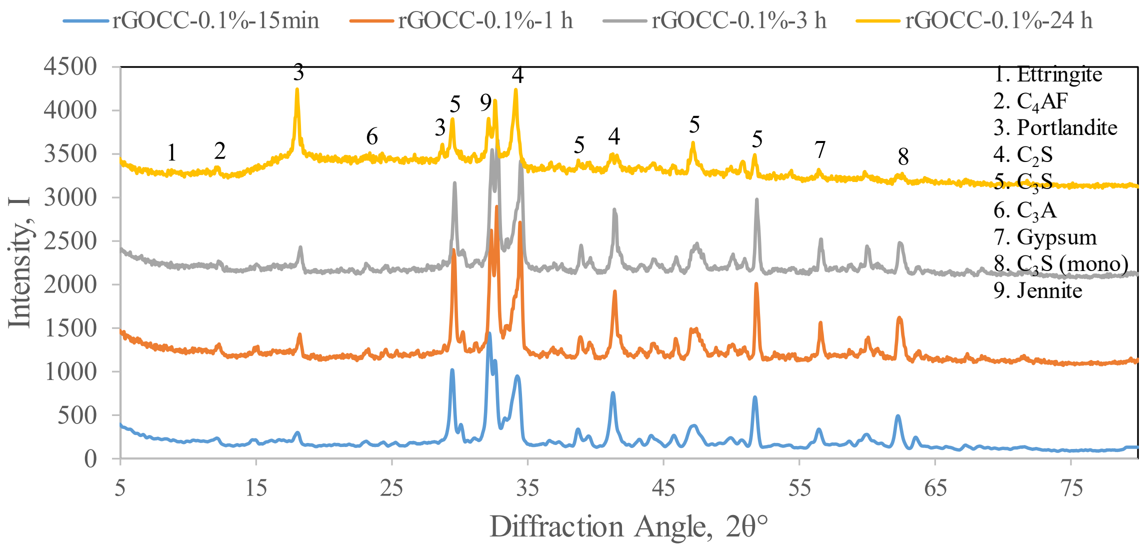

Figure 4.17: XRD pattern for rGOCC-0.1% showing hydration products

C-S-H form from the reaction of alite, larnite and water took the quasi-amorphous form. XRD cannot and should not detect XRD pattern of amorphous material such as C-S-H.

C-S-H resembled the crystal structure of naturally found mineral jennite and tobermorite in short range order (SRO). From this discussion, it can be hypothesized that the peak that are peaked up by the XRD could be a local or short range ordered structure of C-S-H that resembled jennite (Richardson, 2008, Richardson, 2004). Comparing with the EDS analysis on rGOCC-0.1% showed that Ca/Si>1.50 (Taylor, 1986) which is typical for jennite. So both EDS and XRD analysis indicated that C-S-H in this study represented the crystal structure of jennite.

It is noteworthy that, although in this research materials are informally quantified with observing the peak intensity, the peak intensity indicates the position of the atoms in a crystal-not the quantity of the material. However, peak area can be representative of the quantity of a material when background correction has been carried out which, in actuality, is done in this research work by following method (Figure 4.18):

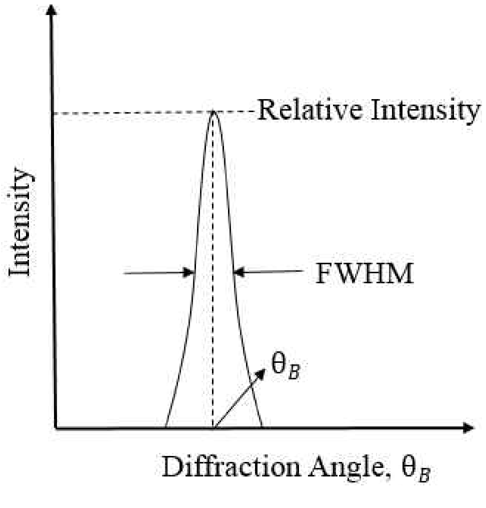

Figure 4.18: Calculation of peak area from FWHM and angle θ in radians.

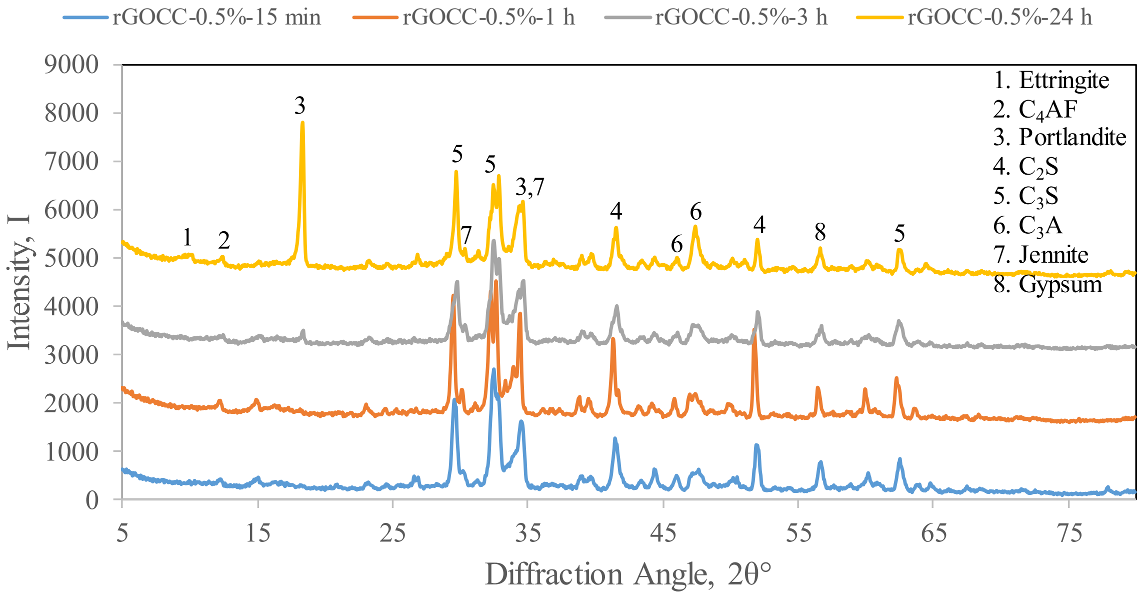

Figure 4.19: XRD pattern for rGOCC-0.5%

XRD pattern from rGOCC-0.5% showed high amount of CH formation. C_3S, C_2S, C_3A and C_4AF showed decrease in quantity after 24 h of hydration for rGOCC-0.5% indicating that all the major phases react similarly as in the plain cement paste.

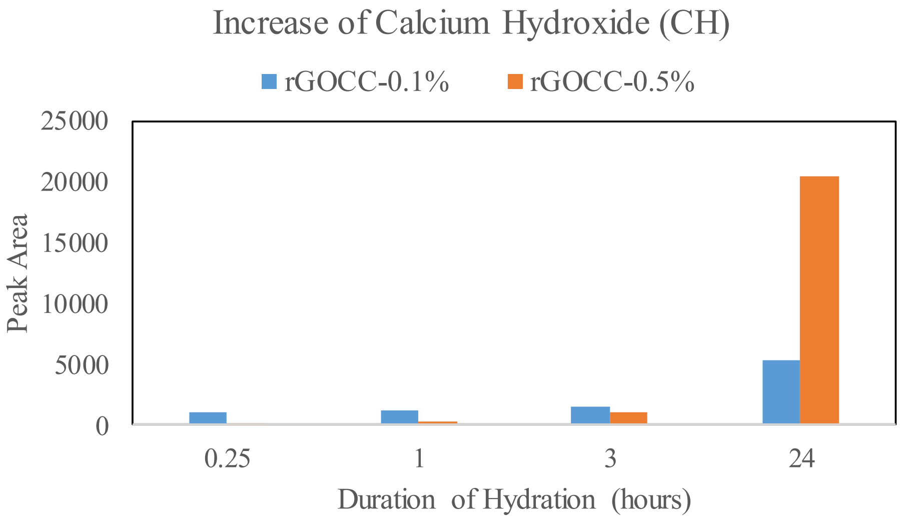

Figure 4.20: Increase of CH for rGOCC-0.1% and rGOCC0.5% over EAH hydration duration

Figure 4.20 indicated that the amount of CH increased for both rGOCC-0.1% and rGOCC-0.5% as hydration continued following Equation 2.1 but composites with 0.50% rGO content showed much higher CH formation after 24 h of hydration indicating larger amount of C_3S and C_2S consumption.

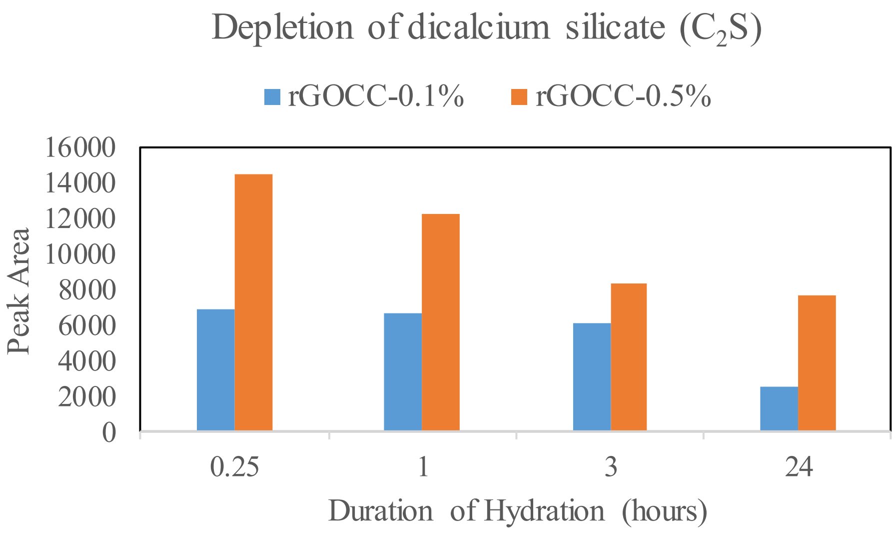

Figure 4.21: Reduction in the C_2S quantity for rGOCC-0.1% and rGOCC0.5% over EAH hydration duration

Evidently, rGOCC-0.5% showed higher rate of depletion for C_2S in Figure 4.21 comparing with that of rGOCC-0.1% until 3 h of hydration. However, at 24 h of hydration, rGOCC-0.1% showed higher depletion rate for C_2S than that of rGOCC-0.5%0%.

4.7 Electrical Resistivity Measurements of rGO-Cement Composite

Table 4.7 shows the variation of ER of rGOCC-cement composites alongside with control sample of cement paste. The rGO content used with cement are 0.5%, 1% and 5% in Saturated Surface Dry (SSD) and Oven Dry (OD) condition. ER was calculated as resitance per unit length using the following formula (Equation 4.3):

$$\rho = R\frac{A}{l} \tag{4.3}$$

Here, ρ is the electrical resistivity, ER (Ω.m), R is the electrical resistance (Ω), A is the cross sectional area of the measurements (m^2), and l is the length between the electrodes (m).

Table 4.7: Presentation of electrical resistivity with varying rGO concentration in cement paste in both SSD and OD conditions (w/c=0.50)

Composite No.	Concentration of rGO (%)	Drying Condition	Across Length (mm)	Bias Voltage E, (V)	Electrical Field Applied (V/m)	Electrical Resistivity, ρ, (Ω. m)
1	0	SSD	10	1	100	5.46×10^3
2	0	OD	10	1	100	3.17×10^6
3	0	OD	10	10	1000	3.50×10^7
4	0.5	OD	10	1	100	3.29×10^6
5	0.5	OD	10	10	1000	1.97×10^6
6	1	SSD	10	1	100	8.47×10^3
7	1	OD	10	1	100	3.86×10^6
8	1	OD	10	10	1000	2.48×10^6
9	5	OD	10	1	100	2.31×10^5

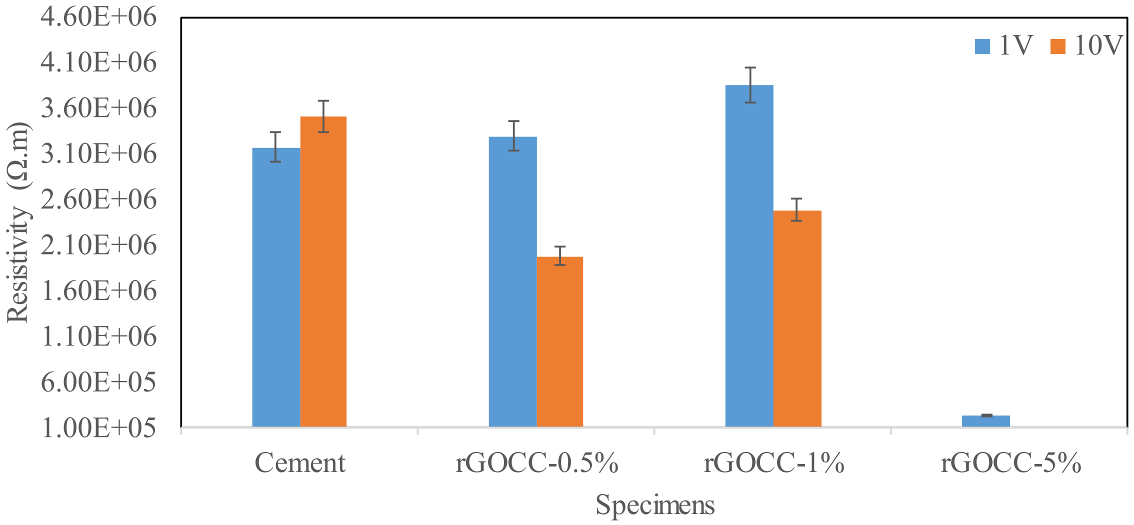

Figure 4.22: Comparison of electrical resistivity of rGOCC specimens (7 d hydration) at 1V and 10V electrical voltages in OD condition

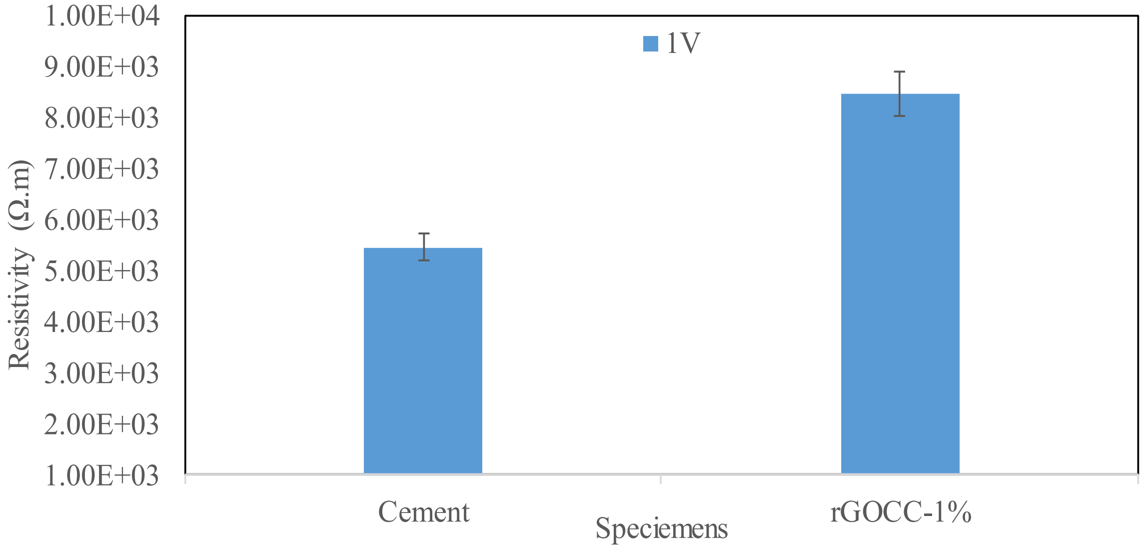

Figure 4.23: Electrical resistivity of cement and rGOCC-1% after 7 d hydration at 1V in SSD condition

From the Table 4.7 and Figures 4.22 and 4.23, it can be seen that two different bias voltages 1V and 10 V are applied as external electrical voltages to supply current through the specimens. In OD condition, cement or rGOCC-1% showed the highest resistivity. rGOCC-1% showed 22% increase in resistivity whereas rGOCC-0.5% showed only 3.79% increase in 1V. However, all the specimens showed decrease in resistivity compared to corresponding resistivity in 1V when 10 V was applied. Cement specimens showed 10% increase in resistivity when 10 V was applied which was presumably an anomaly. On the other hand, rGOCC-0.5% and rGOCC-1% showed 40% and 36% decrease in resistivity when 10 V is applied instead of 1V. Meanwhile, rGOCC-5% showed a drastic change in resistivity by showing 93% decrease in resistivity compared to that of cement at 1V external voltage.

As expected, both cement and rGOCC-1% specimen showed large reduction in resistivity in SSD condition. However, rGOCC-1% still held the trend for increment in resistivity compared to cement specimen in SSD condition as in OD condition. Both cement and rGOCC specimens showed almost 100% decrease in resistivity in SSD condition from their OD condition counterparts. It is to be noted here that the error bars in the graphs represent 95% confidence interval (CI) in the measurements.

The primary hypothesis was, as rGO content increased, the resistivity was supposed to decrease and conductivity was supposed to increase. The result show contrary evidence. The reason behind this observation could be the threefold: (1) filling capability of rGO. rGO could get into the pores and crevices of cement grains and fill up the pores creating compacted specimen as a whole, (2) rGO acts as nucleation sites for production of C-S-H which creates more compacted specimen because of larger surface area blocking the electron tunneling, (3) unlike the CNTs, rGO are sheets and flakes. As a result, they cannot provide as effective electron tunneling as CNTs. CNTs can provide end to end electron tunneling even in the cement paste because of their interconnecting networking capability while that is not the case for rGOs. A generic situation of hydration products of cement and rGO are shown in the Figure 4.24 and also a comparison is made with CNT-cement composite.

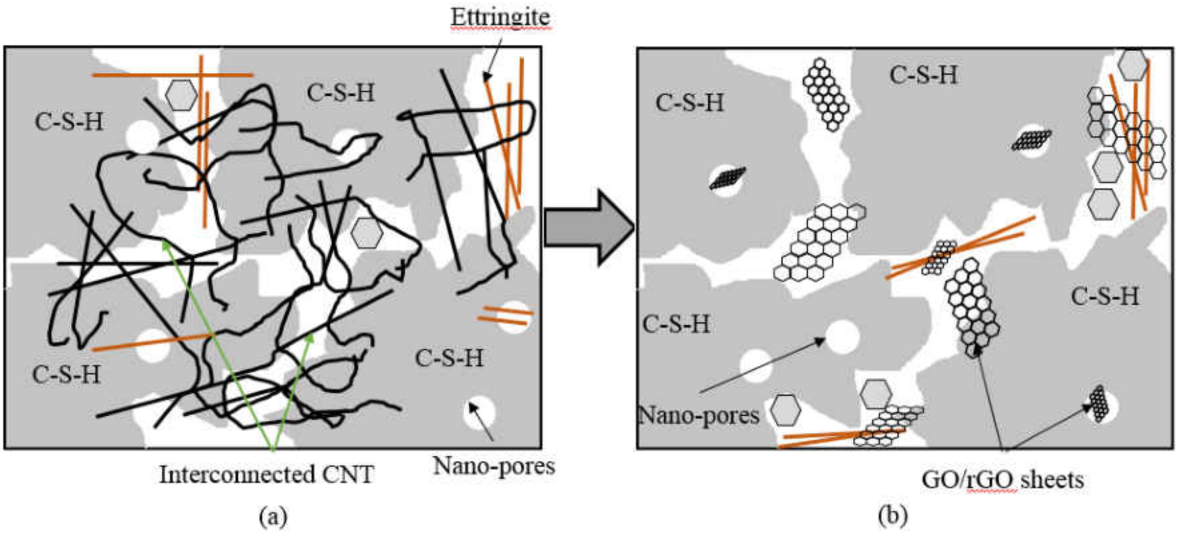

Figure 4.24: (a) Hydration products in CNT-cement composite showing the interweaving among the tubes, attributing to the electron tunneling between the CNT tubes, (b) hydration products in rGO-cement composite showing the lack of interconnection between the sheets hindering the electron tunneling process.

On the other hand, the increase in resistivity for rGOCC-1% in SSD condition compared to its' counterpart in OD condition can be attributed to the ionic conductivity-not increase in electronic conductivity itself. Chung et al. (Chung, 2002) also reported that addition of SF and latex increased the resistivity from 5×10^3 to 6×10^3 and 7×10^3 Ω.m, respectively, similar to the research work at hand. Moreover, with the increase in latex content, the resistivity increased.(Chung, 2004) However, resistivity decreased with an increase in filler content such as SF (Wen and Chung, 2001a).

Figure 4.25 describes the topography of rGOCC-5% which is one of the candidates for electrical resistivity experiments at 7 d of hydration. Observed topography of the rGOCC-5% showed rugged structure, forming many undulations. 2K magnification showed that although there are some 2-3 μm long ettringites were in the specimen, most of the space was occupied by the compacted form of C-S-H, a small portion of which was fibriller C-S-H. Even though the rGO content was 5%, it was not quite apparent because of the grown C-S-H formation. So, it might be plausible that rGO could not decrease the resistivity or increase the conductivity of cement composites in a way that CNT could with a similar CNT content. However, 5% rGO did decrease the resistivity of the cement paste a significant amount, whereas 0.5% and 1% rGO increased the resistivity of the paste because of the reasons already described. From the experimental result, it can be hypothesized that ER percolation threshold could be possible between 1%-5% rGO.

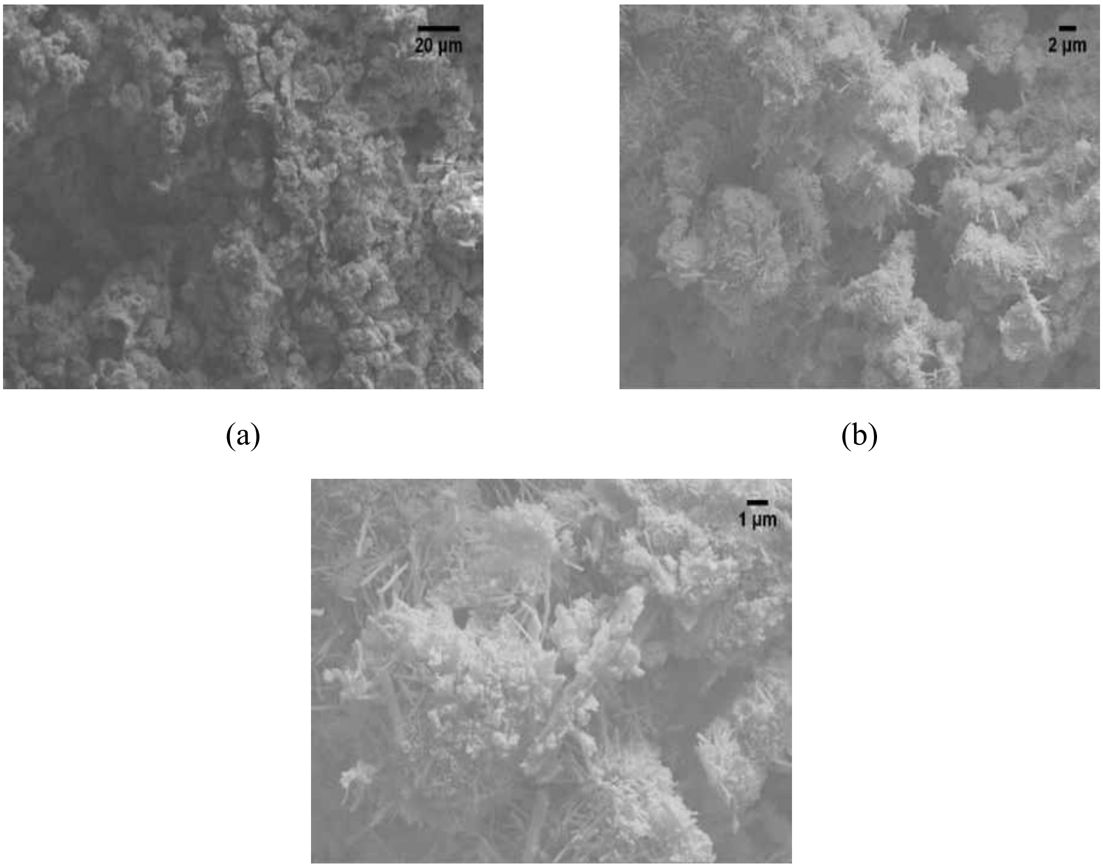

(a) (b)

(c)

Figure 4.25: (a) Topography of rGOCC5% at 500X magnifications, (b) image showing some fibriller structure of C-S-H, although most of C-S-H became compacted by 7 d, (c) closer view of compacted C-S-H at 5K magnification showing lack of interconnection of rGO.

Chung et al. (Chung, 2002, Chung, 2004) reported that ER of cement paste was 4.87×10^3 in SSD condition which was 10.8% lower than that of this research work. Studies about cement composites incorporating SF, CF (Wen and Chung, 2001b) and latex showed that the ER are almost similar to ER shown by rGOCC-1%. From the results of rGOCC-5% in OD condition, it can be fairly predicted that in SSD condition ER of rGO-5% would be just as good or similar to CF. The lower resistivity of CF-cement composite may attributed to the length of CF which averages 5 mm as opposed to the size of the rGO sheets which are drastically lower. In these scenarios, it would be easier for the CF to have better contact and provide carrier hoping electrical conduction. Hence, the percolation threshold of rGOCC falls between 1% and 5% compared to the threshold of CF-cement composite (Chung, 2002), which is ~1-2 %.

CHAPTER 5 CONCLUSIONS AND RECOMMENDATIONS

In this research work, the mechanical properties, microstructural characteristics, ER and EAH properties of GO-composites and rGO-composites are investigated. The results obtained from these experiments have led to the following conclusions:

- GOCC-0.05% demonstrated 27% higher compressive strength in comparison to cement paste after 28 d of hydration. GOCC-0.01% also showed 3.14% increase in compressive strength compared to control specimen after 28 d. The superior compressive strength shown by GOCC-0.05% might be attributed to the nano-filling capacity of GO sheets.

- SEM, EDX and XRD analysis showed that the structure of C-S-H resembled that of jennite and tobermorite-9Å. XRD data showed that crystallite sizes of jennite and tobermorite increased with increasing hydration time for both GOCC-0.01% and GOCC-0.05%. Moreover, GOCC-0.05% showed smaller crystallite sizes than those of GOCC-0.01%. The finer crystallites of GOCC-0.05% indicated larger surface area originating from the lower activation energy for heterogeneous nucleation. This study also provides an outlook on the debate about nucleation mechanism of cement composite incorporating nanomaterials. The study suggest that GO sheets act as nucleation seeds for C-S-H and as a result large number of nucleation occurred which, on the other hand, reduce the critical size of nucleus, hence smaller crystallites.

- Compressive strength of rGOCC-0.05% and rGOCC-0.01% increased by 17% and 7%, respectively after 28 d compared to the control cement paste. Modulus of Rupture

(MOR) increased to 15.5% after 28 d for rGOCC-0.05% and only 0.35% for rGOCC-0.01%, respectively compared to that of control cement paste.

- Microstructural investigation by FESEM on rGOCC-0.05% after 7 d of hydration indicated the presence of all the major hydration products such as C-S-H, ettringites, sulfoaluminates etc.

- Early age hydration (EAH) studies with FESEM for rGOCC-0.1% showed that Ca/Si ratio was around 2 which indicated the probability of disordered jennite-like structure for C-S-H. The Ca-O layer in the C-S-H structure has higher amount of Ca. Some traces of Al was also found from the EDX analysis which can come from the surrounding area of C-S-H, or Al could get into the Ca-O layer to replace Ca atoms and act substitutional element in C-S-H. XRD analysis also detected small intensity of jennite in both rGOCC-0.1% and rGOCC-0.5% specimens. It might dictate that the structure of C-S-H is ordered locally like jennite minerals, alternatively, the C-S-H is short range ordered. Consulting with the result of Chen's work, the structure of C-S-H resembled more as C-S-H (II).

- The XRD data indicated that portlandite (CH) content increased from 15 min to 24 h for both rGOCC-0.01% and rGOCC-0.5% due to the reaction of alite (C_3S) and larnite (C_2S) with water, with rGOCC-0.5% increasing rate being higher. Larnite content decreased with hydration time which indicated the rapid consumption of larnite. Meanwhile, production of CH and C-S-H was continuing.

- Early age hydration (EAH) study on rGOCC-0.1% showed that at 15 min hydration, numerous precipitates of, possibly, C-S-H formed along the grain boundary (GB) of unhydrated cement grains which was visual confirmation of the theory provided by Thomas and Scherer that hydration of cement grains initiated by the short burst of nucleation of C-S-H embryos along GB, which is termed as Boundary Nucleation and Growth (BNG) model.

- The electrical resistivity (ER) increased with an increase in rGO content upto 1 %. But the resistivity decreased drastically about 93% at 5 wt. % rGO content in OD condition, indicating percolation threshold between 1% and 5 wt. % rGO content. In SSD condition, the resistivity also increased compared to plain cement paste but the resistivity was actually much lower than that in OD condition. Comparing with other filler materials from literature, it can be concluded that rGO-cement paste behaves similarly as CF-cement paste, and in some cases better than steel fiber reinforced cement composite.
- Microstructural investigation on the topography of rGOCC-5% after 7 d of hydration indicates that most of the pore spaces are occupied with high density C-S-H. Also, content of ettringites and sulfoaluminates are less indicating less crystalline materials ensuing low conductivity or high resistivity. rGO sheets are covered with C-S-H which is responsible for propagation of the low amount of current through the material. Even though, rGOCC-5% showed the lowest resistivity.

Following recommendations can be made after extensive literature review and current study:

- GO/rGO can be coupled with CNT to investigate the mechanical and microstructural properties of cement composites.

- Measurement of Degree of hydration can be a valuable addition to the study because both GOCC and rGOOCC specimens showed steep slope of compressive and flexural strength curves, indicating hydration was not nearly completed within 28 d.

- It is ambitious to conclude about the structure of C-S-H solely from the XRD data because it makes an approximation about the structure but it does not reveal the true structure. Recommendations could be made to employ TEM to visualize the inner structure and crystallinity of C-S-H. Electron Diffraction pattern could be useful to indicate the ordering of the C-S-H. NMR could be useful to determine the chain length of dimer and trimer associated in the C-S-H polymeric chain.

- Low Ca cement instead of OPC can be used to decrease the Ca/Si ratio to the level of tobermorite. It might have different effects on the mechanical properties and microstructure of GOCC and rGOCC.

- Early age hydration characteristics will be different if low Ca cement is used as primary binding material.

- Reports have been made that the conductivity of cement composites can be higher if filler materials are coupled with polymers. So, studies can be carried out on coating with rGO-polymer over the cement composite surfaces

.

APPENDIX A:
CRYSTALLOGRAPHIC DATA

Calculation of interplanar spacings and unit cell volume of crystals:

Given,

Bragg's Law,

$n\lambda = 2d \sin\theta$

Here,

n=order of reflection

θ=diffraction angle

λ=Wavelength for X-ray diffraction (1.54501Å For CuKα radiation)

Table A.1: Formula for interplanar spacing calculation for several crystal structures

Crystal Structures	Formula for interplanar spacing and lattice parameter	Unit Cell Volume
Cubic	$\frac{1}{d^2} = \frac{h^2 + k^2 + l^2}{a^2}$	$V = a^3$
Hexagonal	$\frac{1}{d^2} = \frac{4}{3}\left(\frac{h^2 + hk + k^2}{a^2}\right) + \frac{l^2}{c^2}$	$V = a^2 c \sin 60^{\circ}$
Tetragonal	$\frac{1}{d^2} = \frac{h^2 + k^2}{a^2} + \frac{l^2}{c^2}$	$V = a^2 c$
Orthorhombic	$\frac{1}{d^2} = \frac{h^2}{a^2} + \frac{k^2}{b^2} + \frac{l^2}{c^2}$	$V = abc$
Rhombohedral	$\frac{1}{d^2} = \frac{(h^2 + k^2 + l^2)\sin^2\alpha + 2(hk + kl + hl)(\cos^2\alpha - \sin\alpha)}{a^2(1 - 3\cos^2\alpha + 2\cos^2\alpha)}$	$V = a^2 c \sin 60^{\circ}$
Monoclinic	$\frac{1}{d^2} = \frac{1}{\sin^2\beta}\left(\frac{h^2}{a^2} + \frac{k^2\sin^2\beta}{b^2} + \frac{l^2}{c^2} - \frac{2hl\cos\beta}{ac}\right)$	$V = abc\sin\beta$
Triclinic		$V = abc(1 - \cos^2\alpha - \cos^2\beta - \cos^2\gamma) + 2\sqrt{\cos\alpha\cos\beta\cos\gamma}$

Here,
h,k,l =miller indices
a,b,c =lattice parameters in X,Y,Z direction in Cartesian coordinates
α, β, γ =angles between, Y-Z, X-Z, and X-Y Coordinates, respectively

APPENDIX B:
ASTM C1365 STANDARD XRD DATA FOR CEMENT PHASES

Table B.1: Peak positions and crystal structures for common cement phases according to ASTM C1365

Phases	Crystal structure	2θ°	d (nm)	ICDD No.
alite	triclinic	29.35	0.3040	31-301
	monoclinic	29.39	0.3036	42-551
	monoclinic	51.78	0.1764	---
	monoclinic	52.00	0.1757	---
β-beilite	monoclinic	31.07	0.2876	33-302
	monoclinic	34.33	0.2610	---
ferrite	---	12.20	0.7249	30-226
	---	24.34	0.3653	---
	---	32.12	0.2784	---
aluminate	cubic	20.95	0.4235	38-1429
	orthorhombic	32.97	0.2714	---
	orthorhombic	33.25	0.2692	26-957

APPENDIX C:
CHEMICAL ANALYSIS DATA BY EDX

Representative quantitative chemical analysis data for GO and rGO by EDX and representative EDX analysis data for GOCC-0.05% after 7-day of hydration

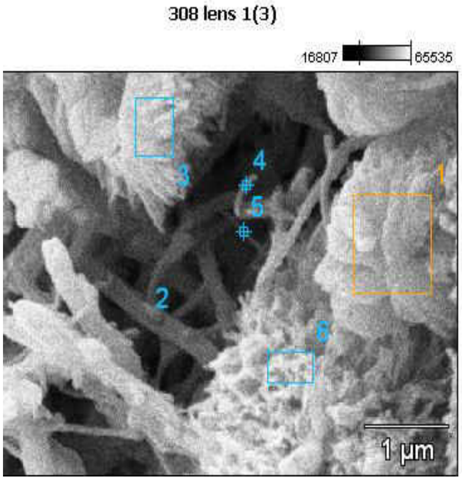

Image Name:	308 lens 1(3)
Image Resolution:	512 by 384
Image Pixel Size:	0.01 µm
Acc. Voltage:	10.0 kV
Magnification:	20000

Figure C.1: SEM image of GOCC-0.05% after 3 d showing points for chemical analysis

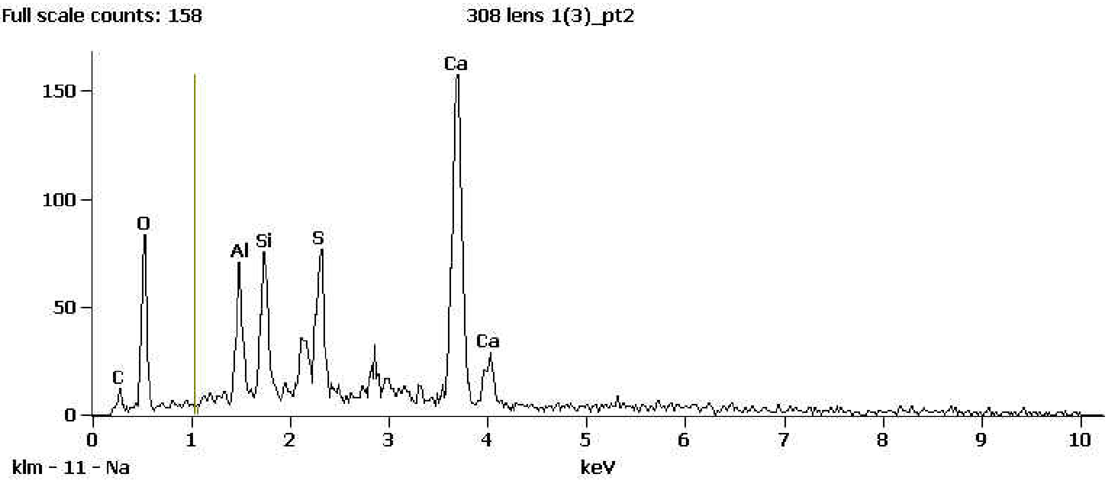

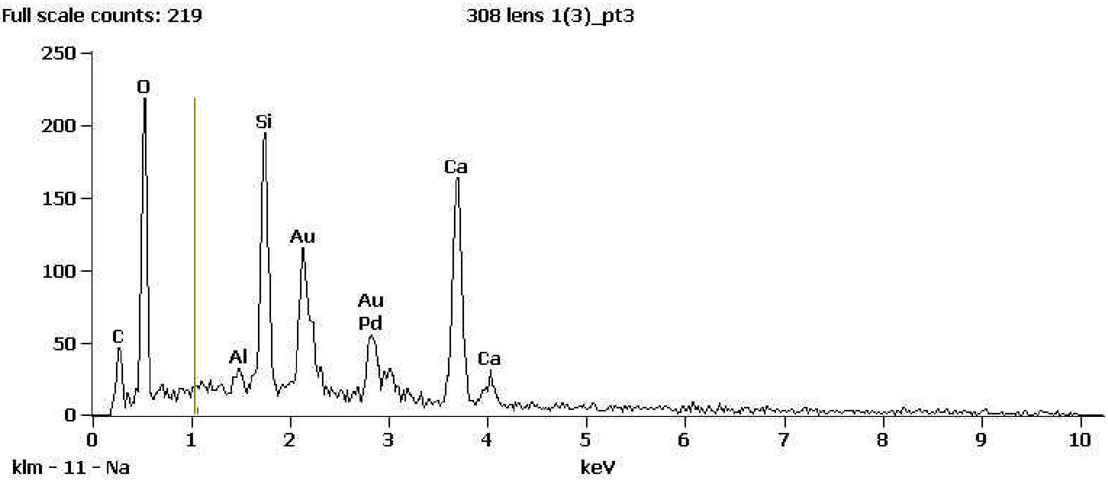

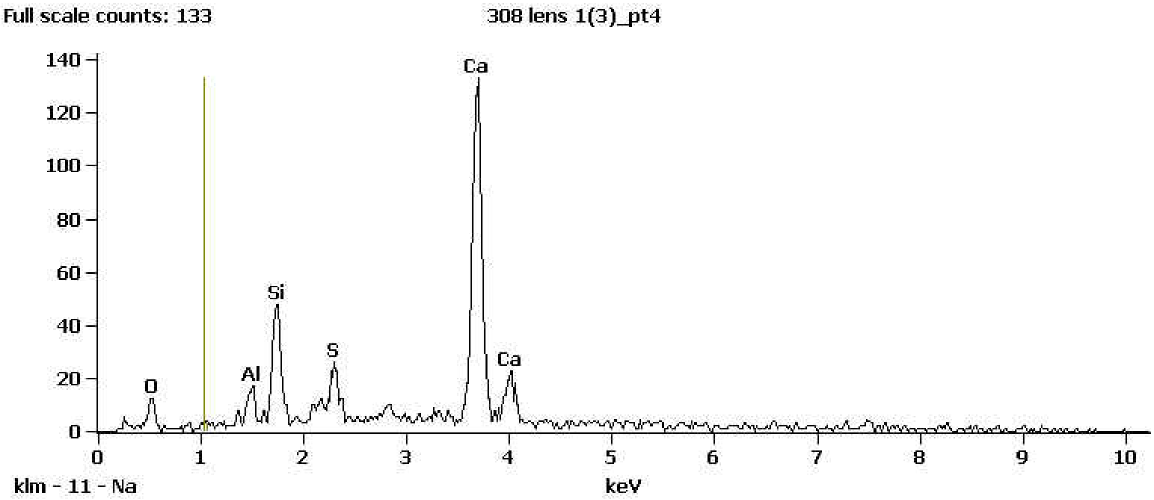
Full scale counts: 133
308 lens 1(3)_pt4
140
120
100
80
60
40
20
0
Ca
Si
S
Ca
Al
O
0
1
2
3
4
5
6
7
8
9
10
klm - 11 - Na
keV

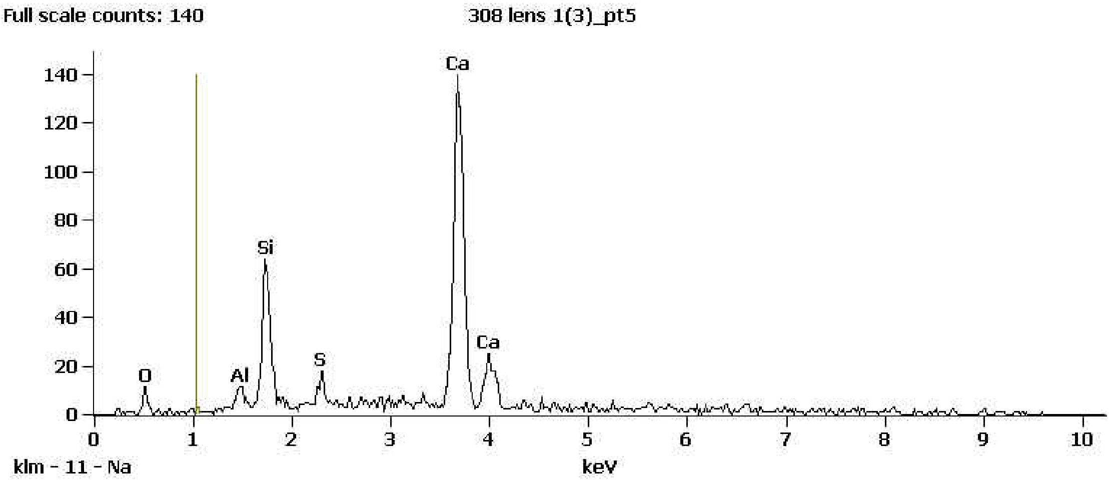
Full scale counts: 140
308 lens 1(3)_pt5
140
120
100
80
60
40
20
0
Ca
Si
Ca
S
Al
O
0
1
2
3
4
5
6
7
8
9
10
klm - 11 - Na
keV

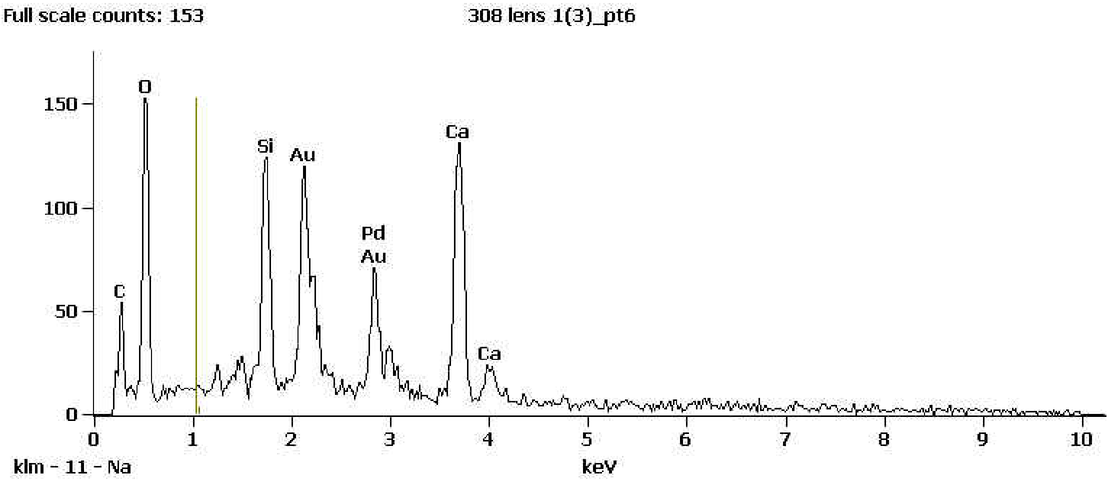

Figure C.2: Chemical analysis by EDX on 6 point shots

Table C.1: Quantitative analysis (weight %) on 6 point shots by EDX

	C-K	*O-K*	*Al-K*	*Si-K*	*S-K*	*Ca-K*	*Pd-L*	*Au-M*
308 lens 1(3)_pt1	4.35	14.00		2.59		59.44		19.63
308 lens 1(3)_pt2	2.18	17.56	4.07	6.58	5.09	64.51		
308 lens 1(3)_pt3	5.71	19.55	0.70	8.71		31.52	14.84	18.97
308 lens 1(3)_pt4		6.28	2.00	7.43	5.03	79.26		
308 lens 1(3)_pt5		3.20	1.17	9.97	2.07	83.59		
308 lens 1(3)_pt6	5.91	18.29		6.84		30.29	17.37	21.29

Weight % Error (+/- 1 Sigma)

	C-K	*O-K*	*Al-K*	*Si-K*	*S-K*	*Ca-K*	*Pd-L*	*Au-M*
308 lens 1(3)_pt1	+/-0.35	+/-1.12		+/-0.44		+/-2.28		+/-1.36
308 lens 1(3)_pt2	+/-0.44	+/-1.11	+/-0.50	+/-0.65	+/-0.89	+/-2.41		
308 lens 1(3)_pt3	+/-0.31	+/-0.79	+/-0.14	+/-0.40		+/-1.27	+/-1.10	+/-1.59
308 lens 1(3)_pt4		+/-0.97	+/-0.24	+/-0.60	+/-0.55	+/-3.31		
308 lens 1(3)_pt5		+/-0.42	+/-0.19	+/-0.58	+/-0.37	+/-3.14		
308 lens 1(3)_pt6	+/-0.34	+/-0.87		+/-0.42		+/-1.35	+/-2.01	+/-1.78

Atom %

	C-K	*O-K*	*Al-K*	*Si-K*	*S-K*	*Ca-K*	*Pd-L*	*Au-M*
308 lens 1(3)_pt1	12.43	30.05		3.17		50.93		3.42
308 lens 1(3)_pt2	5.29	31.98	4.39	6.82	4.63	46.89		
308 lens 1(3)_pt3	15.56	39.99	0.86	10.15		25.74	4.56	3.15
308 lens 1(3)_pt4		13.70	2.58	9.23	5.47	69.01		
308 lens 1(3)_pt5		7.29	1.58	12.91	2.35	75.87		
308 lens 1(3)_pt6	16.94	39.34		8.38		26.00	5.62	3.72

Atom % Error (+/- 1 Sigma)

	C-K	*O-K*	*Al-K*	*Si-K*	*S-K*	*Ca-K*	*Pd-L*	*Au-M*
308 lens 1(3)_pt1	+/-1.01	+/-2.41		+/-0.54		+/-1.95		+/-0.24
308 lens 1(3)_pt2	+/-1.06	+/-2.02	+/-0.54	+/-0.67	+/-0.81	+/-1.75		
308 lens 1(3)_pt3	+/-0.84	+/-1.62	+/-0.17	+/-0.47		+/-1.03	+/-0.34	+/-0.26
308 lens 1(3)_pt4		+/-2.12	+/-0.31	+/-0.74	+/-0.60	+/-2.88		
308 lens 1(3)_pt5		+/-0.96	+/-0.26	+/-0.75	+/-0.42	+/-2.85		
308 lens 1(3)_pt6	+/-0.96	+/-1.87		+/-0.51		+/-1.16	+/-0.65	+/-0.31

Representative EDX analysis data for rGOCC-0.05% for 7-day of hydration

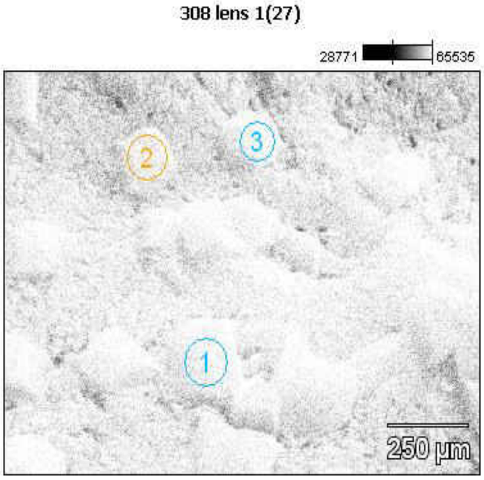

Image Name: 308 lens 1(27)
Image Resolution: 512 by 384
Image Pixel Size: 2.94 µm
Acc. Voltage: 10.0 kV
Magnification: 75

Figure C.3: SEM image of rGOCC-0.05% after 7 d with area shots on 3 different points

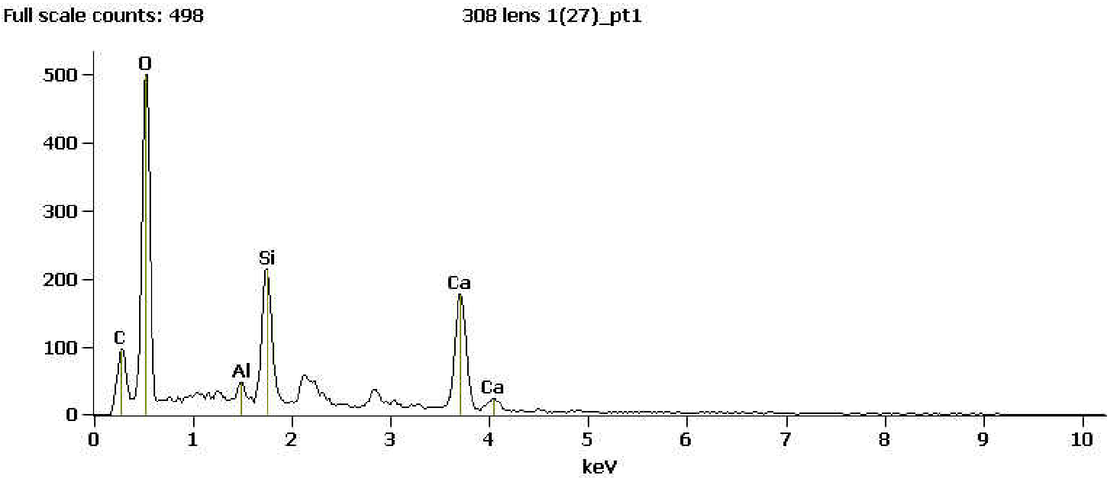

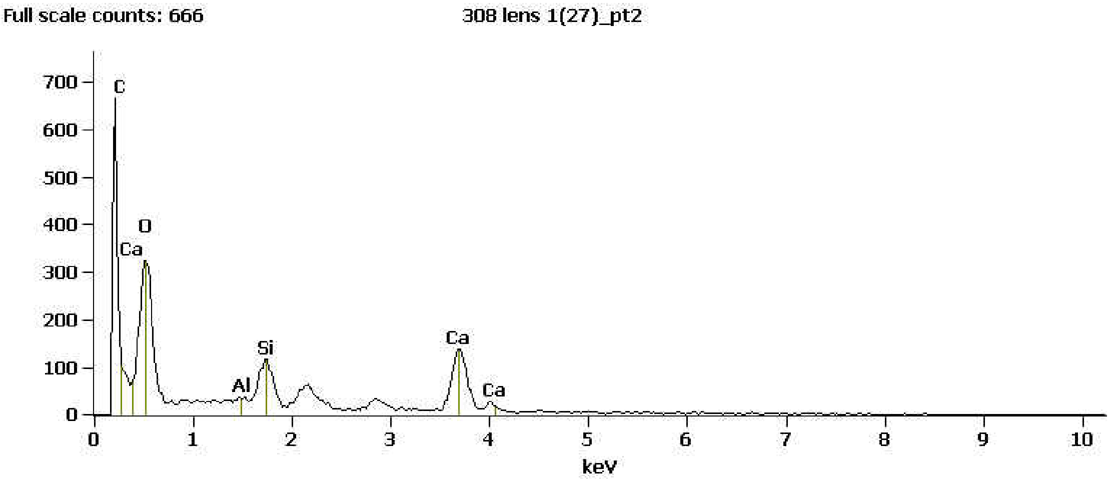

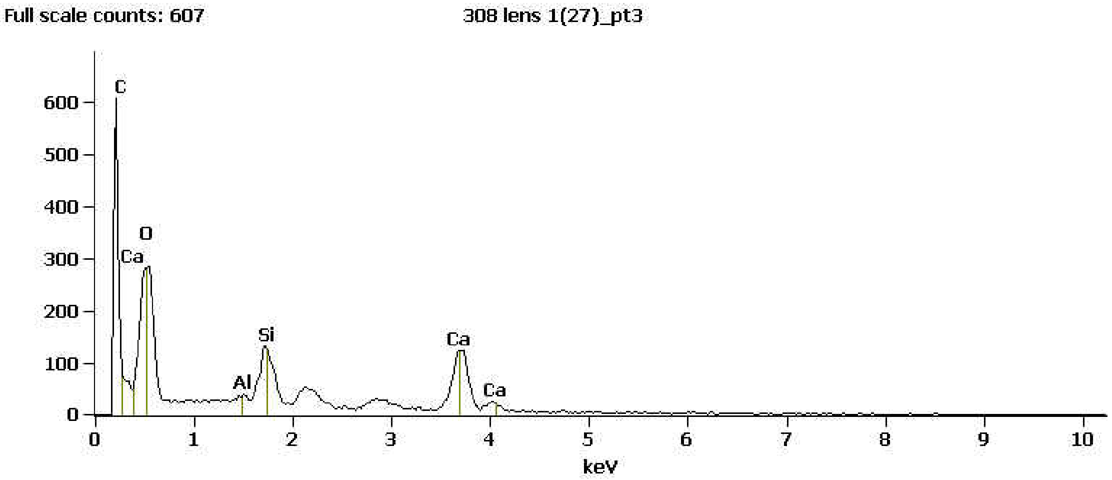

Figure C.4: Chemical analysis by EDX on 3 area shots

Table C.2: Quantitative analysis on 3 area shots by EDX

Weight %

	C-K	*O-K*	*Al-K*	*Si-K*	*Ca-K*
308 lens 1(27)_pt1	10.89	45.97	1.08	10.33	31.73
308 lens 1(27)_pt2	7.21	19.91	3.55	17.58	51.74
308 lens 1(27)_pt3	10.47	7.14	3.71	20.62	58.06

Weight % Error (+/- 1 Sigma)

	C-K	*O-K*	*Al-K*	*Si-K*	*Ca-K*
308 lens 1(27)_pt1	+/-0.47	+/-0.95	+/-0.13	+/-0.23	+/-0.71
308 lens 1(27)_pt2	+/-0.52	+/-4.65	+/-0.97	+/-1.29	+/-2.93
308 lens 1(27)_pt3	+/-0.61	+/-5.70	+/-1.04	+/-1.42	+/-3.25

Atom %

	C-K	*O-K*	*Al-K*	*Si-K*	*Ca-K*
308 lens 1(27)_pt1	18.21	57.70	0.80	7.39	15.90
308 lens 1(27)_pt2	15.42	31.96	3.38	16.08	33.16
308 lens 1(27)_pt3	23.97	12.27	3.78	20.17	39.81

Atom % Error (+/- 1 Sigma)

	C-K	*O-K*	*Al-K*	*Si-K*	*Ca-K*
308 lens 1(27)_pt1	+/-0.79	+/-1.20	+/-0.10	+/-0.17	+/-0.35
308 lens 1(27)_pt2	+/-1.10	+/-7.47	+/-0.92	+/-1.18	+/-1.88
308 lens 1(27)_pt3	+/-1.40	+/-9.79	+/-1.06	+/-1.39	+/-2.23

Representative EDX analysis data for rGOCC-0.1% after 15 minutes of hydration

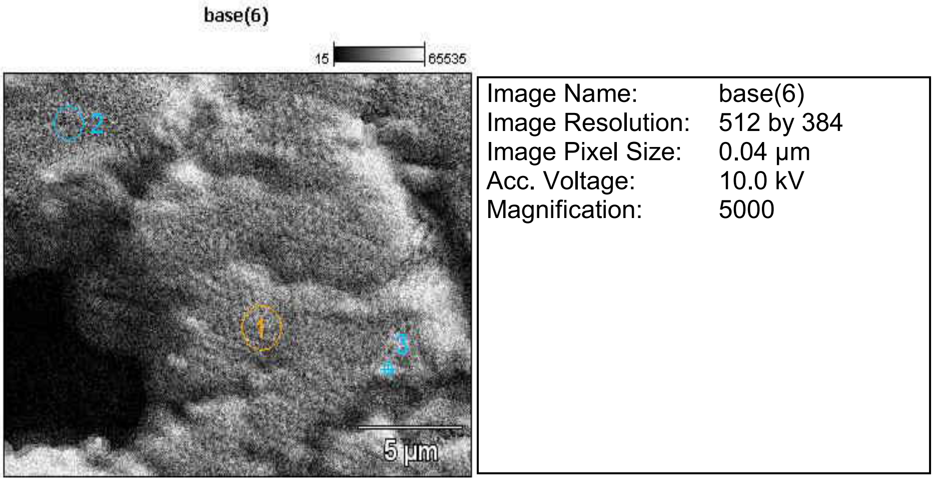

Image Name: base(6)
Image Resolution: 512 by 384
Image Pixel Size: 0.04 µm
Acc. Voltage: 10.0 kV
Magnification: 5000

Figure C.5: SEM image of rGOCC-0.1% after 15 min with area shots on 3 different areas

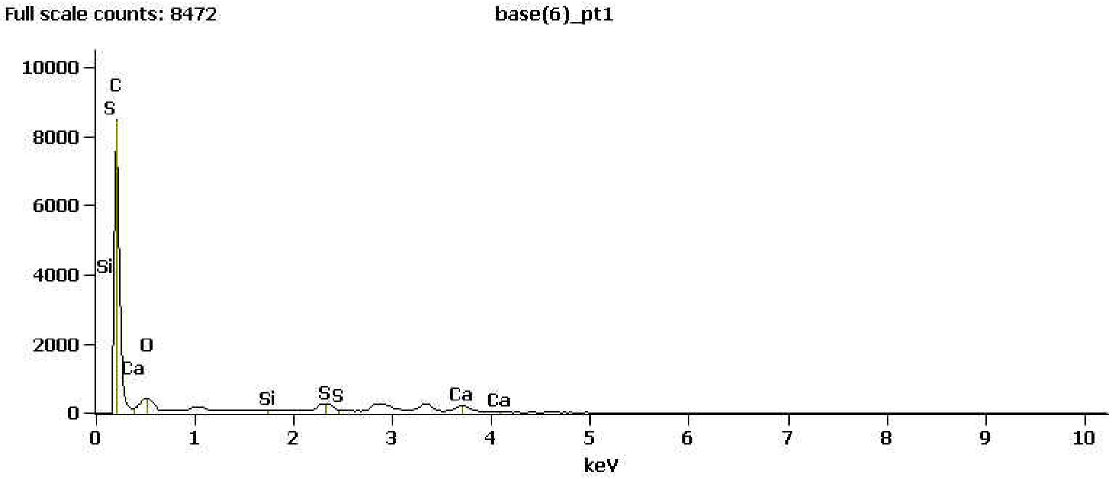

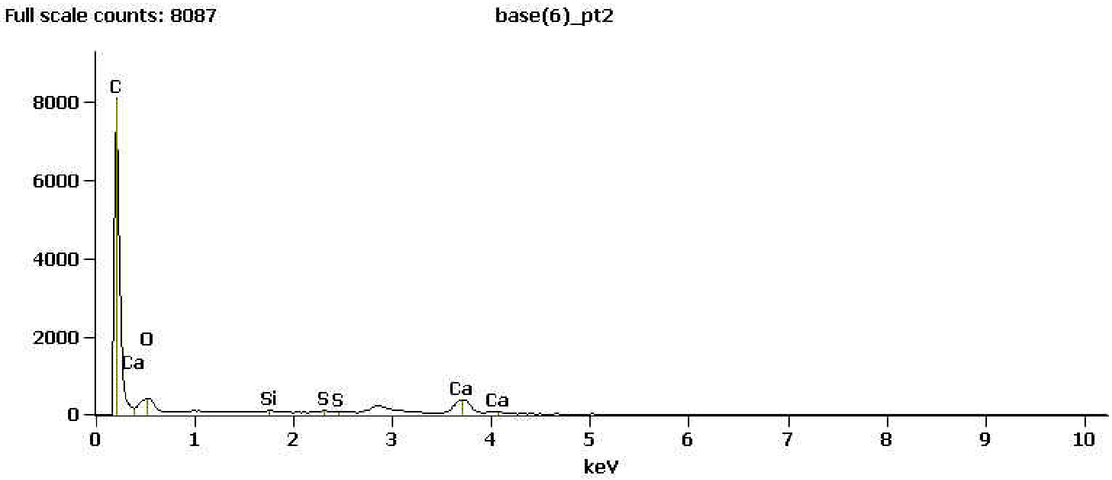

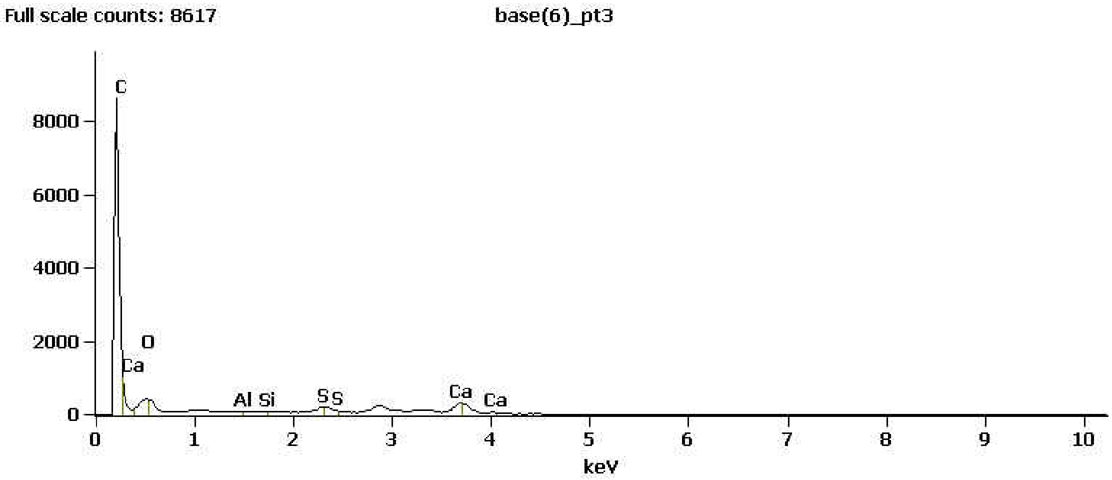

Figure C.6: Chemical analysis by EDX on 3 area shots

Table C.3: Quantitative analysis (weight %) on 3 area shots by EDX

	C-K	*O-K*	*Al-K*	*Si-K*	*S-K*	*Ca-K*
base(6)_pt1	42.87	17.77		0.14	12.02	27.20
base(6)_pt2	29.65	21.13		0.61	1.95	46.66
base(6)_pt3	0.19	0.00	0.33	0.04	23.43	76.00

Weight % Error (+/- 1 Sigma)

	C-K	*O-K*	*Al-K*	*Si-K*	*S-K*	*Ca-K*
base(6)_pt1	+/-1.19	+/-0.77		+/-0.11	+/-0.44	+/-0.95
base(6)_pt2	+/-0.79	+/-0.88		+/-0.12	+/-0.32	+/-1.11
base(6)_pt3	+/-0.12	+/-0.00	+/-0.76	+/-0.82	+/-1.09	+/-2.67

Atom %

	C-K	*O-K*	*Al-K*	*Si-K*	*S-K*	*Ca-K*
base(6)_pt1	62.20	19.35		0.09	6.54	11.83
base(6)_pt2	49.02	26.23		0.43	1.21	23.12
base(6)_pt3	0.61	0.00	0.46	0.06	27.51	71.37

Atom % Error (+/- 1 Sigma)

	C-K	*O-K*	*Al-K*	*Si-K*	*S-K*	*Ca-K*
base(6)_pt1	+/-1.72	+/-0.84		+/-0.07	+/-0.24	+/-0.41
base(6)_pt2	+/-1.31	+/-1.09		+/-0.08	+/-0.20	+/-0.55
base(6)_pt3	+/-0.38	+/-0.00	+/-1.06	+/-1.09	+/-1.28	+/-2.51

Representative EDX analysis data for rGOCC-0.1% after 1 h of hydration

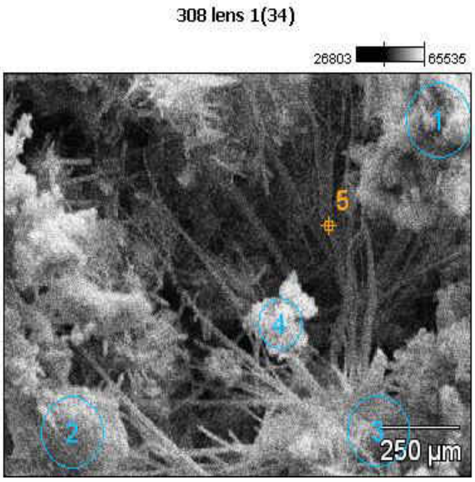

Image Name:	308 lens 1(34)
Image Resolution:	512 by 384
Image Pixel Size:	2.94 µm
Acc. Voltage:	10.0 kV
Magnification:	75

Figure C.7: SEM image of rGOCC-0.1% after 1 h with area shots on 5 different areas

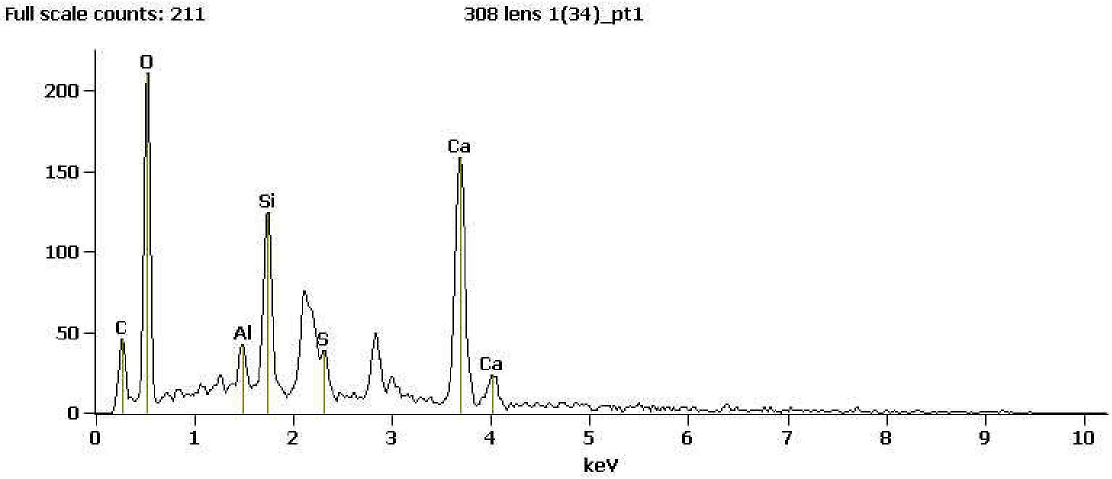

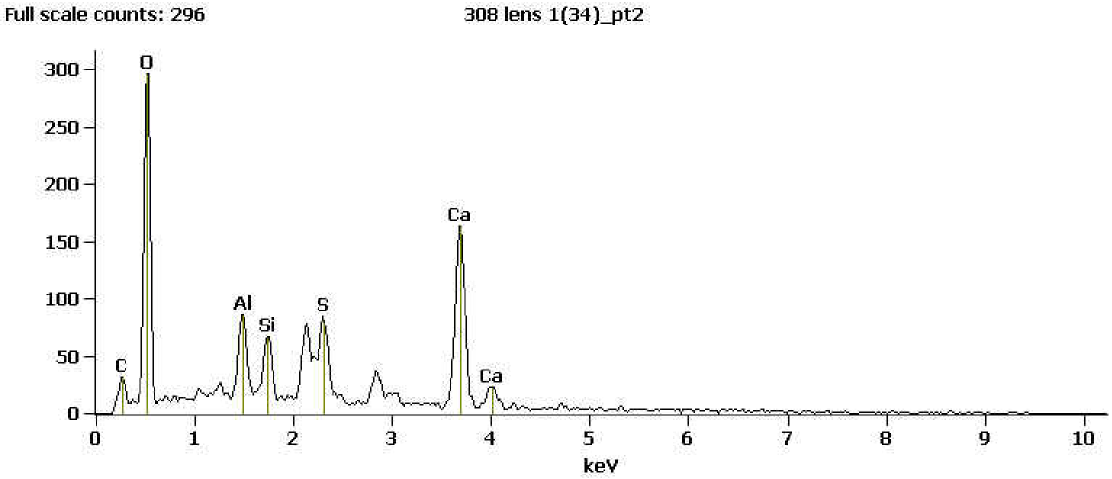

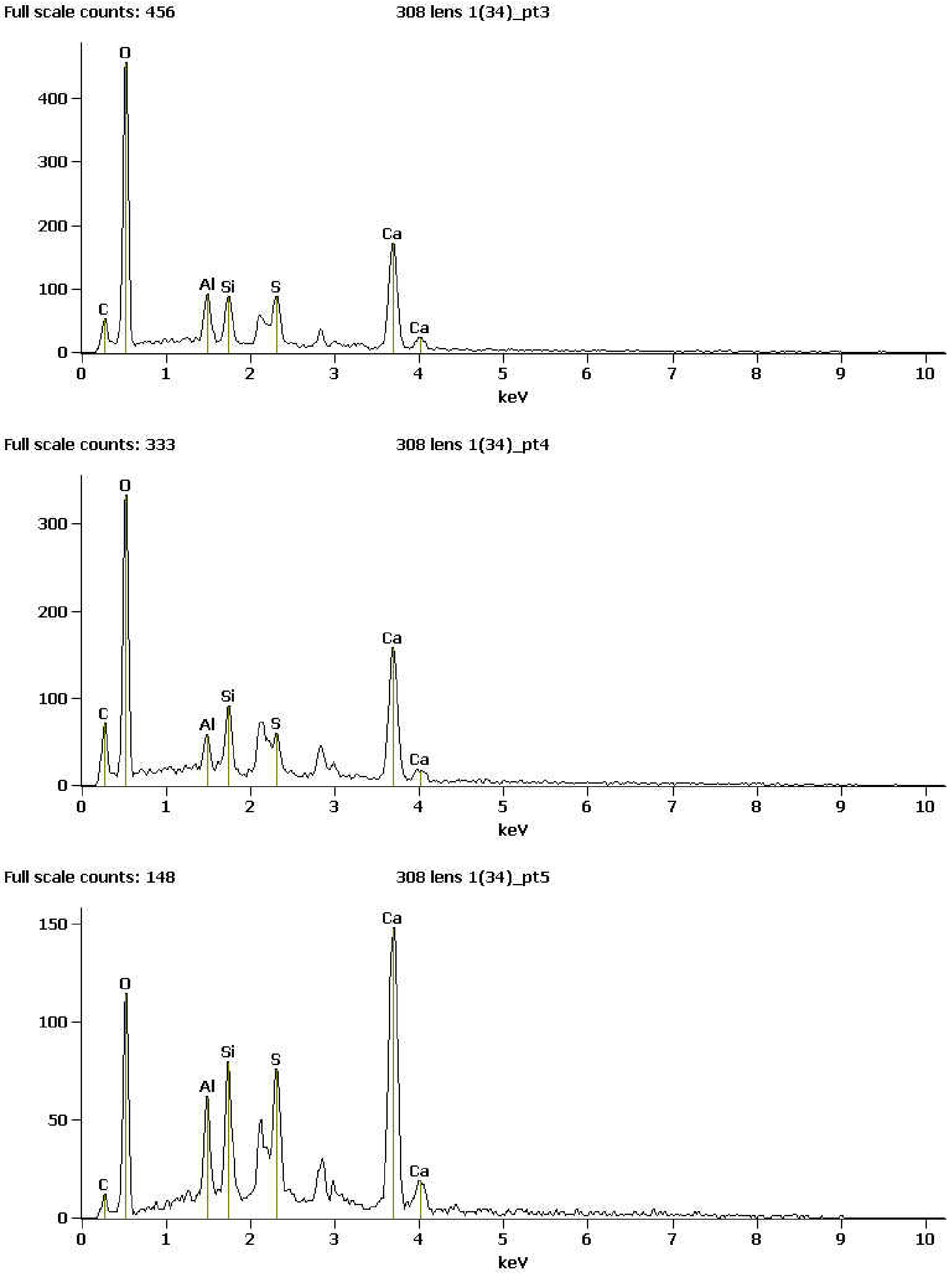

Figure C.8: Chemical analysis by EDX on 5 area shots

Table C.4: Quantitative analysis (weight %) on 3 area shots by EDX

	C-K	*O-K*	*Al-K*	*Si-K*	*S-K*	*Ca-K*
308 lens 1(34)_pt1	7.72	32.53	2.22	10.03	0.00	47.50
308 lens 1(34)_pt2	4.87	38.91	4.69	4.61	5.04	41.87
308 lens 1(34)_pt3	6.67	43.82	3.59	4.73	5.37	35.83
308 lens 1(34)_pt4	9.39	40.80	2.44	5.65	1.52	40.20
308 lens 1(34)_pt5	2.79	25.85	3.67	6.94	8.11	52.63

Weight % Error (+/- 1 Sigma)

	C-K	*O-K*	*Al-K*	*Si-K*	*S-K*	*Ca-K*
308 lens 1(34)_pt1	+/-0.55	+/-1.23	+/-0.21	+/-0.32	+/-0.00	+/-1.79
308 lens 1(34)_pt2	+/-0.52	+/-1.12	+/-0.42	+/-0.25	+/-0.45	+/-1.61
308 lens 1(34)_pt3	+/-0.40	+/-0.95	+/-0.34	+/-0.21	+/-0.35	+/-1.31
308 lens 1(34)_pt4	+/-0.43	+/-1.11	+/-0.20	+/-0.24	+/-0.40	+/-1.53
308 lens 1(34)_pt5	+/-0.38	+/-1.06	+/-0.44	+/-0.32	+/-0.56	+/-2.08

Atom %

	C-K	*O-K*	*Al-K*	*Si-K*	*S-K*	*Ca-K*
308 lens 1(34)_pt1	14.94	47.28	1.91	8.30	0.00	27.56
308 lens 1(34)_pt2	9.27	55.56	3.97	3.75	3.59	23.86
308 lens 1(34)_pt3	11.92	58.82	2.85	3.62	3.59	19.19
308 lens 1(34)_pt4	16.73	54.56	1.94	4.31	1.01	21.46
308 lens 1(34)_pt5	6.12	42.54	3.59	6.51	6.66	34.58

Atom % Error (+/- 1 Sigma)

	C-K	*O-K*	*Al-K*	*Si-K*	*S-K*	*Ca-K*
308 lens 1(34)_pt1	+/-1.06	+/-1.79	+/-0.18	+/-0.26	+/-0.00	+/-1.04
308 lens 1(34)_pt2	+/-0.99	+/-1.60	+/-0.35	+/-0.20	+/-0.32	+/-0.92
308 lens 1(34)_pt3	+/-0.72	+/-1.27	+/-0.27	+/-0.16	+/-0.24	+/-0.70
308 lens 1(34)_pt4	+/-0.76	+/-1.48	+/-0.16	+/-0.19	+/-0.27	+/-0.82
308 lens 1(34)_pt5	+/-0.83	+/-1.75	+/-0.43	+/-0.30	+/-0.46	+/-1.36

APPENDIX D:
XRD CRYSTAL STRUCTURE DATA

Table D.1: XRD peak fit profile for rGOCC-0.5% at 15 min of hydration

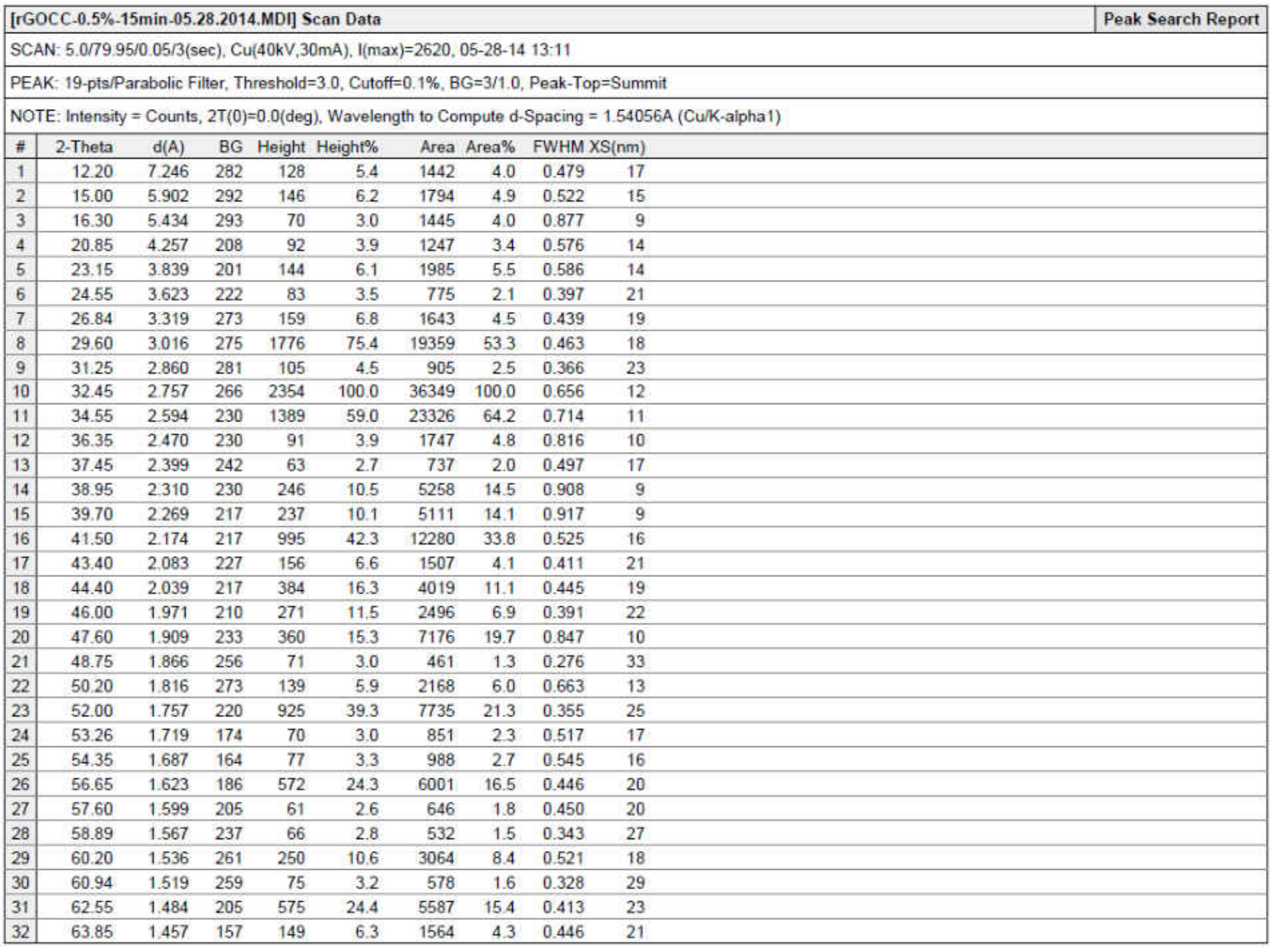

[rGOCC-0.5%-15min-05.28.2014.MDI] Scan Data **Peak Search Report**

SCAN: 5.0/79.95/0.05/3(sec), Cu(40kV,30mA), I(max)=2620, 05-28-14 13:11

PEAK: 19-pts/Parabolic Filter, Threshold=3.0, Cutoff=0.1%, BG=3/1.0, Peak-Top=Summit

NOTE: Intensity = Counts, 2T(0)=0.0(deg), Wavelength to Compute d-Spacing = 1.54056A (Cu/K-alpha1)

#	2-Theta	d(A)	BG	Height	Height%	Area	Area%	FWHM	XS(nm)
1	12.20	7.246	282	128	5.4	1442	4.0	0.479	17
2	15.00	5.902	292	146	6.2	1794	4.9	0.522	15
3	16.30	5.434	293	70	3.0	1445	4.0	0.877	9
4	20.85	4.257	208	92	3.9	1247	3.4	0.576	14
5	23.15	3.839	201	144	6.1	1985	5.5	0.586	14
6	24.55	3.623	222	83	3.5	775	2.1	0.397	21
7	26.84	3.319	273	159	6.8	1643	4.5	0.439	19
8	29.60	3.016	275	1776	75.4	19359	53.3	0.463	18
9	31.25	2.860	281	105	4.5	905	2.5	0.366	23
10	32.45	2.757	266	2354	100.0	36349	100.0	0.656	12
11	34.55	2.594	230	1389	59.0	23326	64.2	0.714	11
12	36.35	2.470	230	91	3.9	1747	4.8	0.816	10
13	37.45	2.399	242	63	2.7	737	2.0	0.497	17
14	38.95	2.310	230	246	10.5	5258	14.5	0.908	9
15	39.70	2.269	217	237	10.1	5111	14.1	0.917	9
16	41.50	2.174	217	995	42.3	12280	33.8	0.525	16
17	43.40	2.083	227	156	6.6	1507	4.1	0.411	21
18	44.40	2.039	217	384	16.3	4019	11.1	0.445	19
19	46.00	1.971	210	271	11.5	2496	6.9	0.391	22
20	47.60	1.909	233	360	15.3	7176	19.7	0.847	10
21	48.75	1.866	256	71	3.0	461	1.3	0.276	33
22	50.20	1.816	273	139	5.9	2168	6.0	0.663	13
23	52.00	1.757	220	925	39.3	7735	21.3	0.355	25
24	53.26	1.719	174	70	3.0	851	2.3	0.517	17
25	54.35	1.687	164	77	3.3	988	2.7	0.545	16
26	56.65	1.623	186	572	24.3	6001	16.5	0.446	20
27	57.60	1.599	205	61	2.6	646	1.8	0.450	20
28	58.89	1.567	237	66	2.8	532	1.5	0.343	27
29	60.20	1.536	261	250	10.6	3064	8.4	0.521	18
30	60.94	1.519	259	75	3.2	578	1.6	0.328	29
31	62.55	1.484	205	575	24.4	5587	15.4	0.413	23
32	63.85	1.457	157	149	6.3	1564	4.3	0.446	21

Table D.2: XRD Peaks for Alite (impure C_3S)

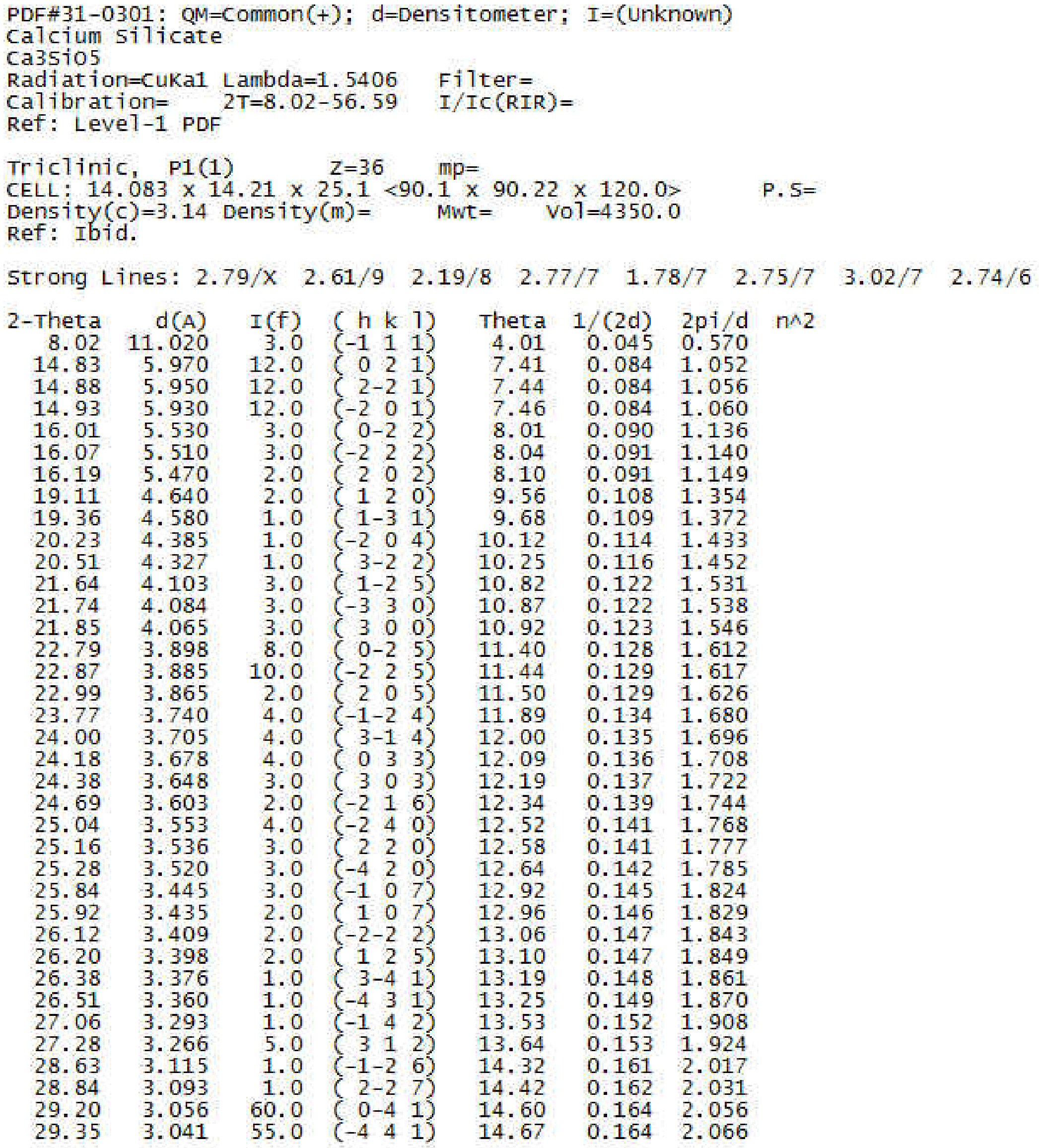

```
PDF#31-0301: QM=Common(+); d=Densitometer; I=(Unknown)
Calcium Silicate
Ca3SiO5
Radiation=CuKa1 Lambda=1.5406    Filter=
Calibration=     2T=8.02-56.59   I/Ic(RIR)=
Ref: Level-1 PDF

Triclinic,  P1(1)        Z=36     mp=
CELL: 14.083 x 14.21 x 25.1 <90.1 x 90.22 x 120.0>      P.S=
Density(c)=3.14 Density(m)=     Mwt=    Vol=4350.0
Ref: Ibid.

Strong Lines: 2.79/X  2.61/9  2.19/8  2.77/7  1.78/7  2.75/7  3.02/7  2.74/6

2-Theta    d(A)    I(f)   ( h k l)    Theta  1/(2d)  2pi/d  n^2
   8.02  11.020     3.0   (-1 1 1)     4.01   0.045  0.570
  14.83   5.970    12.0   ( 0 2 1)     7.41   0.084  1.052
  14.88   5.950    12.0   ( 2-2 1)     7.44   0.084  1.056
  14.93   5.930    12.0   (-2 0 1)     7.46   0.084  1.060
  16.01   5.530     3.0   ( 0-2 2)     8.01   0.090  1.136
  16.07   5.510     3.0   (-2 2 2)     8.04   0.091  1.140
  16.19   5.470     2.0   ( 2 0 2)     8.10   0.091  1.149
  19.11   4.640     2.0   ( 1 2 0)     9.56   0.108  1.354
  19.36   4.580     1.0   ( 1-3 1)     9.68   0.109  1.372
  20.23   4.385     1.0   (-2 0 4)    10.12   0.114  1.433
  20.51   4.327     1.0   ( 3-2 2)    10.25   0.116  1.452
  21.64   4.103     3.0   ( 1-2 5)    10.82   0.122  1.531
  21.74   4.084     3.0   (-3 3 0)    10.87   0.122  1.538
  21.85   4.065     3.0   ( 3 0 0)    10.92   0.123  1.546
  22.79   3.898     8.0   ( 0-2 5)    11.40   0.128  1.612
  22.87   3.885    10.0   (-2 2 5)    11.44   0.129  1.617
  22.99   3.865     2.0   ( 2 0 5)    11.50   0.129  1.626
  23.77   3.740     4.0   (-1-2 4)    11.89   0.134  1.680
  24.00   3.705     4.0   ( 3-1 4)    12.00   0.135  1.696
  24.18   3.678     4.0   ( 0 3 3)    12.09   0.136  1.708
  24.38   3.648     3.0   ( 3 0 3)    12.19   0.137  1.722
  24.69   3.603     2.0   (-2 1 6)    12.34   0.139  1.744
  25.04   3.553     4.0   (-2 4 0)    12.52   0.141  1.768
  25.16   3.536     3.0   ( 2 2 0)    12.58   0.141  1.777
  25.28   3.520     3.0   (-4 2 0)    12.64   0.142  1.785
  25.84   3.445     3.0   (-1 0 7)    12.92   0.145  1.824
  25.92   3.435     2.0   ( 1 0 7)    12.96   0.146  1.829
  26.12   3.409     2.0   (-2-2 2)    13.06   0.147  1.843
  26.20   3.398     2.0   ( 1 2 5)    13.10   0.147  1.849
  26.38   3.376     1.0   ( 3-4 1)    13.19   0.148  1.861
  26.51   3.360     1.0   (-4 3 1)    13.25   0.149  1.870
  27.06   3.293     1.0   (-1 4 2)    13.53   0.152  1.908
  27.28   3.266     5.0   ( 3 1 2)    13.64   0.153  1.924
  28.63   3.115     1.0   (-1-2 6)    14.32   0.161  2.017
  28.84   3.093     1.0   ( 2-2 7)    14.42   0.162  2.031
  29.20   3.056    60.0   ( 0-4 1)    14.60   0.164  2.056
  29.35   3.041    55.0   (-4 4 1)    14.67   0.164  2.066
```

Table D.3: XRD Peaks for Alite (Monoclinic C_3S)

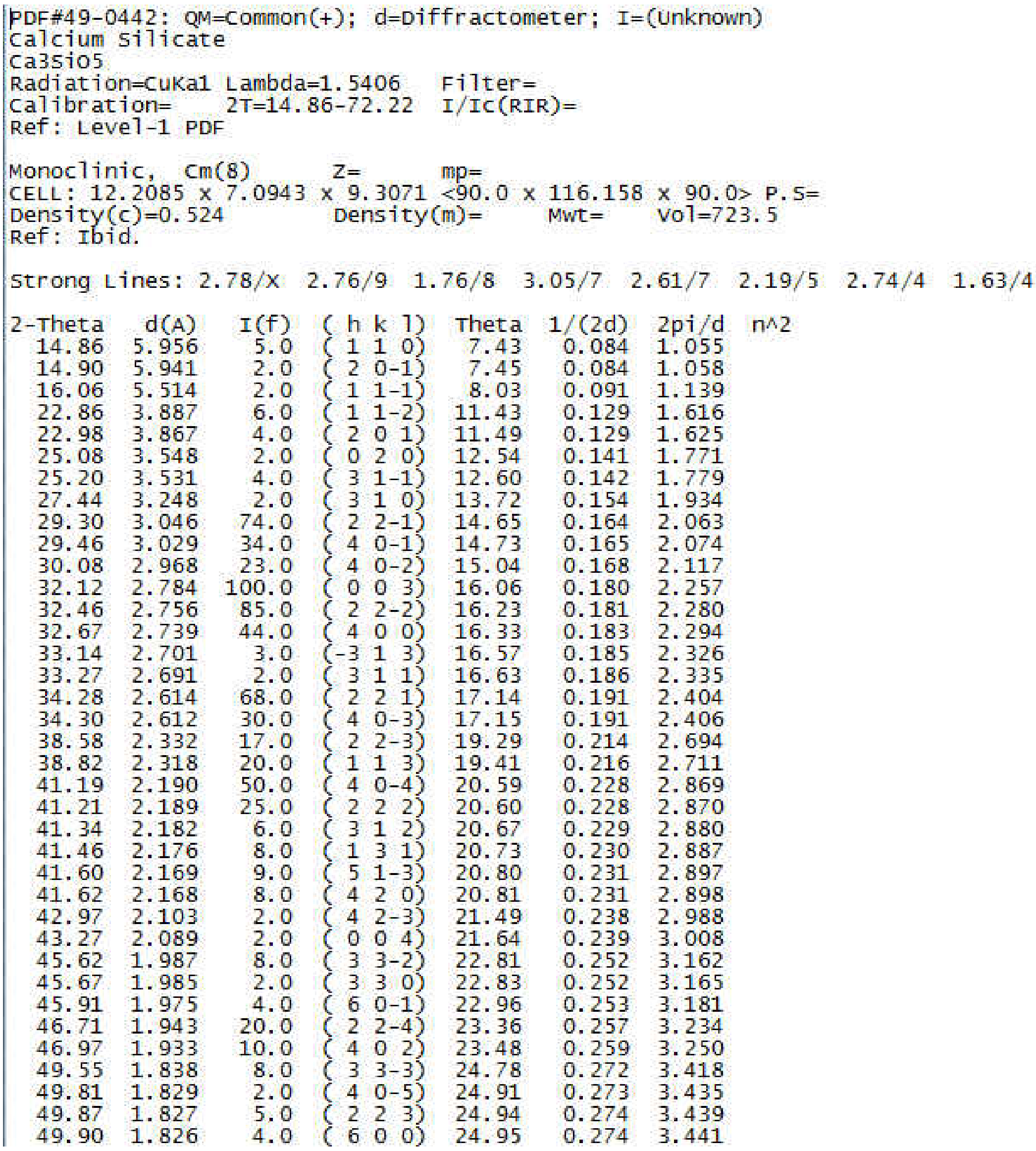

```
PDF#49-0442: QM=Common(+); d=Diffractometer; I=(Unknown)
Calcium Silicate
Ca3SiO5
Radiation=CuKa1 Lambda=1.5406   Filter=
Calibration=    2T=14.86-72.22  I/Ic(RIR)=
Ref: Level-1 PDF

Monoclinic,  Cm(8)       Z=      mp=
CELL: 12.2085 x 7.0943 x 9.3071 <90.0 x 116.158 x 90.0> P.S=
Density(c)=0.524        Density(m)=     Mwt=    Vol=723.5
Ref: Ibid.

Strong Lines: 2.78/X  2.76/9  1.76/8  3.05/7  2.61/7  2.19/5  2.74/4  1.63/4

2-Theta   d(A)    I(f)   ( h k l)   Theta  1/(2d)  2pi/d  n^2
  14.86  5.956     5.0  ( 1 1 0)    7.43   0.084  1.055
  14.90  5.941     2.0  ( 2 0-1)    7.45   0.084  1.058
  16.06  5.514     2.0  ( 1 1-1)    8.03   0.091  1.139
  22.86  3.887     6.0  ( 1 1-2)   11.43   0.129  1.616
  22.98  3.867     4.0  ( 2 0 1)   11.49   0.129  1.625
  25.08  3.548     2.0  ( 0 2 0)   12.54   0.141  1.771
  25.20  3.531     4.0  ( 3 1-1)   12.60   0.142  1.779
  27.44  3.248     2.0  ( 3 1 0)   13.72   0.154  1.934
  29.30  3.046    74.0  ( 2 2-1)   14.65   0.164  2.063
  29.46  3.029    34.0  ( 4 0-1)   14.73   0.165  2.074
  30.08  2.968    23.0  ( 4 0-2)   15.04   0.168  2.117
  32.12  2.784   100.0  ( 0 0 3)   16.06   0.180  2.257
  32.46  2.756    85.0  ( 2 2-2)   16.23   0.181  2.280
  32.67  2.739    44.0  ( 4 0 0)   16.33   0.183  2.294
  33.14  2.701     3.0  (-3 1 3)   16.57   0.185  2.326
  33.27  2.691     2.0  ( 3 1 1)   16.63   0.186  2.335
  34.28  2.614    68.0  ( 2 2 1)   17.14   0.191  2.404
  34.30  2.612    30.0  ( 4 0-3)   17.15   0.191  2.406
  38.58  2.332    17.0  ( 2 2-3)   19.29   0.214  2.694
  38.82  2.318    20.0  ( 1 1 3)   19.41   0.216  2.711
  41.19  2.190    50.0  ( 4 0-4)   20.59   0.228  2.869
  41.21  2.189    25.0  ( 2 2 2)   20.60   0.228  2.870
  41.34  2.182     6.0  ( 3 1 2)   20.67   0.229  2.880
  41.46  2.176     8.0  ( 1 3 1)   20.73   0.230  2.887
  41.60  2.169     9.0  ( 5 1-3)   20.80   0.231  2.897
  41.62  2.168     8.0  ( 4 2 0)   20.81   0.231  2.898
  42.97  2.103     2.0  ( 4 2-3)   21.49   0.238  2.988
  43.27  2.089     2.0  ( 0 0 4)   21.64   0.239  3.008
  45.62  1.987     8.0  ( 3 3-2)   22.81   0.252  3.162
  45.67  1.985     2.0  ( 3 3 0)   22.83   0.252  3.165
  45.91  1.975     4.0  ( 6 0-1)   22.96   0.253  3.181
  46.71  1.943    20.0  ( 2 2-4)   23.36   0.257  3.234
  46.97  1.933    10.0  ( 4 0 2)   23.48   0.259  3.250
  49.55  1.838     8.0  ( 3 3-3)   24.78   0.272  3.418
  49.81  1.829     2.0  ( 4 0-5)   24.91   0.273  3.435
  49.87  1.827     5.0  ( 2 2 3)   24.94   0.274  3.439
  49.90  1.826     4.0  ( 6 0 0)   24.95   0.274  3.441
```

Table D.4: XRD Peaks for Larnite (impure C_2S)

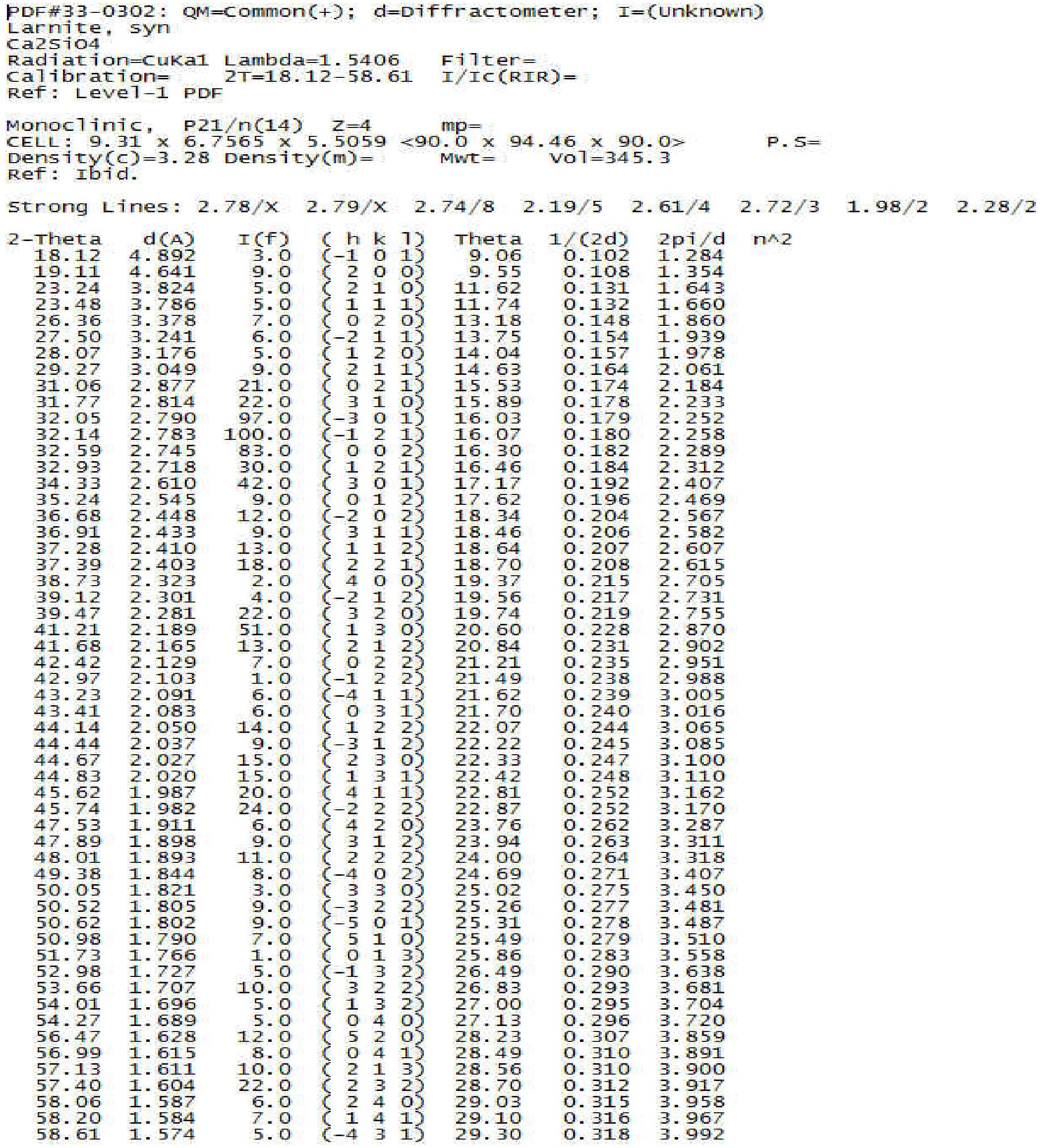

```
PDF#33-0302: QM=Common(+); d=Diffractometer; I=(Unknown)
Larnite, syn
Ca2SiO4
Radiation=CuKa1 Lambda=1.5406   Filter=
Calibration=    2T=18.12-58.61  I/Ic(RIR)=
Ref: Level-1 PDF

Monoclinic,  P21/n(14)  Z=4     mp=
CELL: 9.31 x 6.7565 x 5.5059 <90.0 x 94.46 x 90.0>      P.S=
Density(c)=3.28 Density(m)=     Mwt=    Vol=345.3
Ref: Ibid.

Strong Lines: 2.78/X  2.79/X  2.74/8  2.19/5  2.61/4  2.72/3  1.98/2  2.28/2

2-Theta   d(A)    I(f)   ( h k l)  Theta  1/(2d)  2pi/d  n^2
  18.12  4.892     3.0   (-1 0 1)   9.06  0.102   1.284
  19.11  4.641     9.0   ( 2 0 0)   9.55  0.108   1.354
  23.24  3.824     5.0   ( 2 1 0)  11.62  0.131   1.643
  23.48  3.786     5.0   ( 1 1 1)  11.74  0.132   1.660
  26.36  3.378     7.0   ( 0 2 0)  13.18  0.148   1.860
  27.50  3.241     6.0   (-2 1 1)  13.75  0.154   1.939
  28.07  3.176     5.0   ( 1 2 0)  14.04  0.157   1.978
  29.27  3.049     9.0   ( 2 1 1)  14.63  0.164   2.061
  31.06  2.877    21.0   ( 0 2 1)  15.53  0.174   2.184
  31.77  2.814    22.0   ( 3 1 0)  15.89  0.178   2.233
  32.05  2.790    97.0   (-3 0 1)  16.03  0.179   2.252
  32.14  2.783   100.0   (-1 2 1)  16.07  0.180   2.258
  32.59  2.745    83.0   ( 0 0 2)  16.30  0.182   2.289
  32.93  2.718    30.0   ( 1 2 1)  16.46  0.184   2.312
  34.33  2.610    42.0   ( 3 0 1)  17.17  0.192   2.407
  35.24  2.545     9.0   ( 0 1 2)  17.62  0.196   2.469
  36.68  2.448    12.0   (-2 0 2)  18.34  0.204   2.567
  36.91  2.433     9.0   ( 3 1 1)  18.46  0.206   2.582
  37.28  2.410    13.0   ( 1 1 2)  18.64  0.207   2.607
  37.39  2.403    18.0   ( 2 2 1)  18.70  0.208   2.615
  38.73  2.323     2.0   ( 4 0 0)  19.37  0.215   2.705
  39.12  2.301     4.0   (-2 1 2)  19.56  0.217   2.731
  39.47  2.281    22.0   ( 3 2 0)  19.74  0.219   2.755
  41.21  2.189    51.0   ( 1 3 0)  20.60  0.228   2.870
  41.68  2.165    13.0   ( 2 1 2)  20.84  0.231   2.902
  42.42  2.129     7.0   ( 0 2 2)  21.21  0.235   2.951
  42.97  2.103     1.0   (-1 2 2)  21.49  0.238   2.988
  43.23  2.091     6.0   (-4 1 1)  21.62  0.239   3.005
  43.41  2.083     6.0   ( 0 3 1)  21.70  0.240   3.016
  44.14  2.050    14.0   ( 1 2 2)  22.07  0.244   3.065
  44.44  2.037     9.0   (-3 1 2)  22.22  0.245   3.085
  44.67  2.027    15.0   ( 2 3 0)  22.33  0.247   3.100
  44.83  2.020    15.0   ( 1 3 1)  22.42  0.248   3.110
  45.62  1.987    20.0   ( 4 1 1)  22.81  0.252   3.162
  45.74  1.982    24.0   (-2 2 2)  22.87  0.252   3.170
  47.53  1.911     6.0   ( 4 2 0)  23.76  0.262   3.287
  47.89  1.898     9.0   ( 3 1 2)  23.94  0.263   3.311
  48.01  1.893    11.0   ( 2 2 2)  24.00  0.264   3.318
  49.38  1.844     8.0   (-4 0 2)  24.69  0.271   3.407
  50.05  1.821     3.0   ( 3 3 0)  25.02  0.275   3.450
  50.52  1.805     9.0   (-3 2 2)  25.26  0.277   3.481
  50.62  1.802     9.0   (-5 0 1)  25.31  0.278   3.487
  50.98  1.790     7.0   ( 5 1 0)  25.49  0.279   3.510
  51.73  1.766     1.0   ( 0 1 3)  25.86  0.283   3.558
  52.98  1.727     5.0   (-1 3 2)  26.49  0.290   3.638
  53.66  1.707    10.0   ( 3 2 2)  26.83  0.293   3.681
  54.01  1.696     5.0   ( 1 3 2)  27.00  0.295   3.704
  54.27  1.689     5.0   ( 0 4 0)  27.13  0.296   3.720
  56.47  1.628    12.0   ( 5 2 0)  28.23  0.307   3.859
  56.99  1.615     8.0   ( 0 4 1)  28.49  0.310   3.891
  57.13  1.611    10.0   ( 2 1 3)  28.56  0.310   3.900
  57.40  1.604    22.0   ( 2 3 2)  28.70  0.312   3.917
  58.06  1.587     6.0   ( 2 4 0)  29.03  0.315   3.958
  58.20  1.584     7.0   ( 1 4 1)  29.10  0.316   3.967
  58.61  1.574     5.0   (-4 3 1)  29.30  0.318   3.992
```

Table D.5: XRD Peaks for Larnite (impure C_3A)

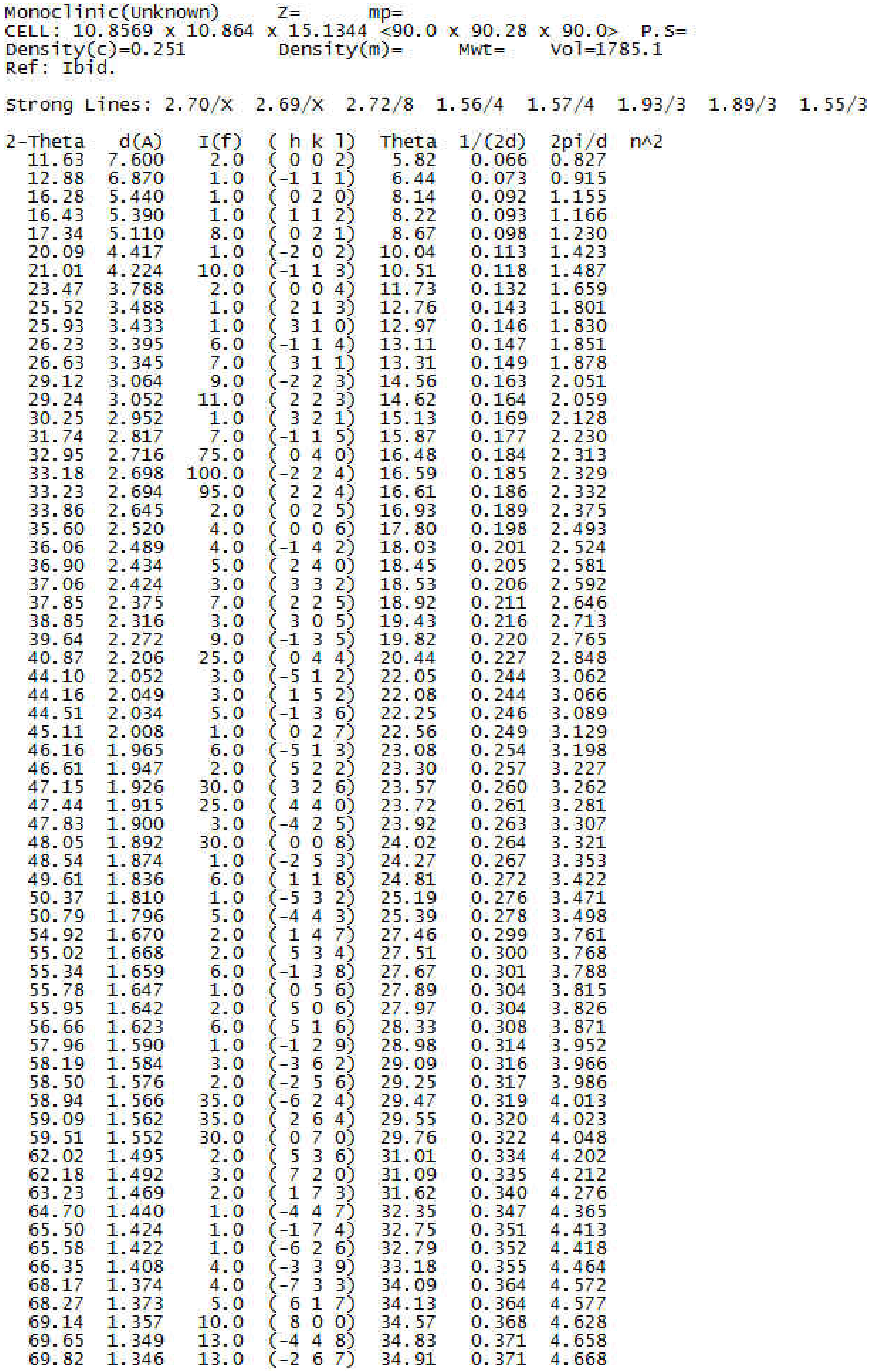

```
Monoclinic(Unknown)      Z=      mp=
CELL: 10.8569 x 10.864 x 15.1344 <90.0 x 90.28 x 90.0>  P.S=
Density(c)=0.251        Density(m)=     Mwt=    Vol=1785.1
Ref: Ibid.

Strong Lines: 2.70/X  2.69/X  2.72/8  1.56/4  1.57/4  1.93/3  1.89/3  1.55/3

2-Theta   d(A)   I(f)   ( h k l)  Theta  1/(2d)  2pi/d  n^2
  11.63  7.600    2.0   ( 0 0 2)   5.82  0.066  0.827
  12.88  6.870    1.0   (-1 1 1)   6.44  0.073  0.915
  16.28  5.440    1.0   ( 0 2 0)   8.14  0.092  1.155
  16.43  5.390    1.0   ( 1 1 2)   8.22  0.093  1.166
  17.34  5.110    8.0   ( 0 2 1)   8.67  0.098  1.230
  20.09  4.417    1.0   (-2 0 2)  10.04  0.113  1.423
  21.01  4.224   10.0   (-1 1 3)  10.51  0.118  1.487
  23.47  3.788    2.0   ( 0 0 4)  11.73  0.132  1.659
  25.52  3.488    1.0   ( 2 1 3)  12.76  0.143  1.801
  25.93  3.433    1.0   ( 3 1 0)  12.97  0.146  1.830
  26.23  3.395    6.0   (-1 1 4)  13.11  0.147  1.851
  26.63  3.345    7.0   ( 3 1 1)  13.31  0.149  1.878
  29.12  3.064    9.0   (-2 2 3)  14.56  0.163  2.051
  29.24  3.052   11.0   ( 2 2 3)  14.62  0.164  2.059
  30.25  2.952    1.0   ( 3 2 1)  15.13  0.169  2.128
  31.74  2.817    7.0   (-1 1 5)  15.87  0.177  2.230
  32.95  2.716   75.0   ( 0 4 0)  16.48  0.184  2.313
  33.18  2.698  100.0   (-2 2 4)  16.59  0.185  2.329
  33.23  2.694   95.0   ( 2 2 4)  16.61  0.186  2.332
  33.86  2.645    2.0   ( 0 2 5)  16.93  0.189  2.375
  35.60  2.520    4.0   ( 0 0 6)  17.80  0.198  2.493
  36.06  2.489    4.0   (-1 4 2)  18.03  0.201  2.524
  36.90  2.434    5.0   ( 2 4 0)  18.45  0.205  2.581
  37.06  2.424    3.0   ( 3 3 2)  18.53  0.206  2.592
  37.85  2.375    7.0   ( 2 2 5)  18.92  0.211  2.646
  38.85  2.316    3.0   ( 3 0 5)  19.43  0.216  2.713
  39.64  2.272    9.0   (-1 3 5)  19.82  0.220  2.765
  40.87  2.206   25.0   ( 0 4 4)  20.44  0.227  2.848
  44.10  2.052    3.0   (-5 1 2)  22.05  0.244  3.062
  44.16  2.049    3.0   ( 1 5 2)  22.08  0.244  3.066
  44.51  2.034    5.0   (-1 3 6)  22.25  0.246  3.089
  45.11  2.008    1.0   ( 0 2 7)  22.56  0.249  3.129
  46.16  1.965    6.0   (-5 1 3)  23.08  0.254  3.198
  46.61  1.947    2.0   ( 5 2 2)  23.30  0.257  3.227
  47.15  1.926   30.0   ( 3 2 6)  23.57  0.260  3.262
  47.44  1.915   25.0   ( 4 4 0)  23.72  0.261  3.281
  47.83  1.900    3.0   (-4 2 5)  23.92  0.263  3.307
  48.05  1.892   30.0   ( 0 0 8)  24.02  0.264  3.321
  48.54  1.874    1.0   (-2 5 3)  24.27  0.267  3.353
  49.61  1.836    6.0   ( 1 1 8)  24.81  0.272  3.422
  50.37  1.810    1.0   (-5 3 2)  25.19  0.276  3.471
  50.79  1.796    5.0   (-4 4 3)  25.39  0.278  3.498
  54.92  1.670    2.0   ( 1 4 7)  27.46  0.299  3.761
  55.02  1.668    2.0   ( 5 3 4)  27.51  0.300  3.768
  55.34  1.659    6.0   (-1 3 8)  27.67  0.301  3.788
  55.78  1.647    1.0   ( 0 5 6)  27.89  0.304  3.815
  55.95  1.642    2.0   ( 5 0 6)  27.97  0.304  3.826
  56.66  1.623    6.0   ( 5 1 6)  28.33  0.308  3.871
  57.96  1.590    1.0   (-1 2 9)  28.98  0.314  3.952
  58.19  1.584    3.0   (-3 6 2)  29.09  0.316  3.966
  58.50  1.576    2.0   (-2 5 6)  29.25  0.317  3.986
  58.94  1.566   35.0   (-6 2 4)  29.47  0.319  4.013
  59.09  1.562   35.0   ( 2 6 4)  29.55  0.320  4.023
  59.51  1.552   30.0   ( 0 7 0)  29.76  0.322  4.048
  62.02  1.495    2.0   ( 5 3 6)  31.01  0.334  4.202
  62.18  1.492    3.0   ( 7 2 0)  31.09  0.335  4.212
  63.23  1.469    2.0   ( 1 7 3)  31.62  0.340  4.276
  64.70  1.440    1.0   (-4 4 7)  32.35  0.347  4.365
  65.50  1.424    1.0   (-1 7 4)  32.75  0.351  4.413
  65.58  1.422    1.0   (-6 2 6)  32.79  0.352  4.418
  66.35  1.408    4.0   (-3 3 9)  33.18  0.355  4.464
  68.17  1.374    4.0   (-7 3 3)  34.09  0.364  4.572
  68.27  1.373    5.0   ( 6 1 7)  34.13  0.364  4.577
  69.14  1.357   10.0   ( 8 0 0)  34.57  0.368  4.628
  69.65  1.349   13.0   (-4 4 8)  34.83  0.371  4.658
  69.82  1.346   13.0   (-2 6 7)  34.91  0.371  4.668
```

Table D.6: XRD Peaks for Brownmillerite (impure C_4AF)

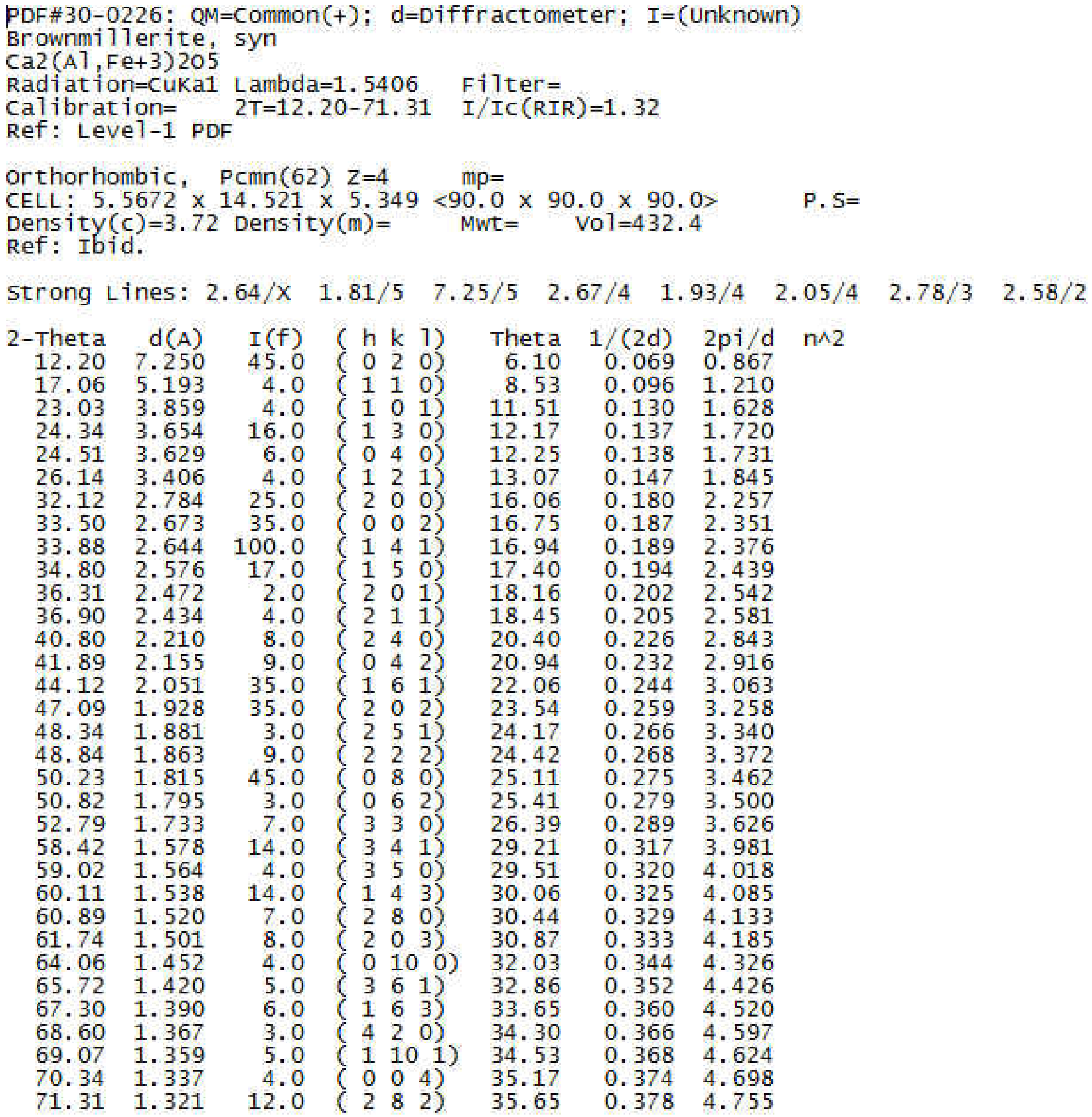

```
PDF#30-0226: QM=Common(+); d=Diffractometer; I=(Unknown)
Brownmillerite, syn
Ca2(Al,Fe+3)2O5
Radiation=CuKa1 Lambda=1.5406   Filter=
Calibration=    2T=12.20-71.31  I/Ic(RIR)=1.32
Ref: Level-1 PDF

Orthorhombic,  Pcmn(62) Z=4     mp=
CELL: 5.5672 x 14.521 x 5.349 <90.0 x 90.0 x 90.0>      P.S=
Density(c)=3.72 Density(m)=     Mwt=    Vol=432.4
Ref: Ibid.

Strong Lines: 2.64/X  1.81/5  7.25/5  2.67/4  1.93/4  2.05/4  2.78/3  2.58/2

2-Theta   d(A)   I(f)   ( h k l)   Theta  1/(2d)  2pi/d  n^2
  12.20  7.250   45.0   ( 0 2 0)    6.10   0.069  0.867
  17.06  5.193    4.0   ( 1 1 0)    8.53   0.096  1.210
  23.03  3.859    4.0   ( 1 0 1)   11.51   0.130  1.628
  24.34  3.654   16.0   ( 1 3 0)   12.17   0.137  1.720
  24.51  3.629    6.0   ( 0 4 0)   12.25   0.138  1.731
  26.14  3.406    4.0   ( 1 2 1)   13.07   0.147  1.845
  32.12  2.784   25.0   ( 2 0 0)   16.06   0.180  2.257
  33.50  2.673   35.0   ( 0 0 2)   16.75   0.187  2.351
  33.88  2.644  100.0   ( 1 4 1)   16.94   0.189  2.376
  34.80  2.576   17.0   ( 1 5 0)   17.40   0.194  2.439
  36.31  2.472    2.0   ( 2 0 1)   18.16   0.202  2.542
  36.90  2.434    4.0   ( 2 1 1)   18.45   0.205  2.581
  40.80  2.210    8.0   ( 2 4 0)   20.40   0.226  2.843
  41.89  2.155    9.0   ( 0 4 2)   20.94   0.232  2.916
  44.12  2.051   35.0   ( 1 6 1)   22.06   0.244  3.063
  47.09  1.928   35.0   ( 2 0 2)   23.54   0.259  3.258
  48.34  1.881    3.0   ( 2 5 1)   24.17   0.266  3.340
  48.84  1.863    9.0   ( 2 2 2)   24.42   0.268  3.372
  50.23  1.815   45.0   ( 0 8 0)   25.11   0.275  3.462
  50.82  1.795    3.0   ( 0 6 2)   25.41   0.279  3.500
  52.79  1.733    7.0   ( 3 3 0)   26.39   0.289  3.626
  58.42  1.578   14.0   ( 3 4 1)   29.21   0.317  3.981
  59.02  1.564    4.0   ( 3 5 0)   29.51   0.320  4.018
  60.11  1.538   14.0   ( 1 4 3)   30.06   0.325  4.085
  60.89  1.520    7.0   ( 2 8 0)   30.44   0.329  4.133
  61.74  1.501    8.0   ( 2 0 3)   30.87   0.333  4.185
  64.06  1.452    4.0   ( 0 10 0)  32.03   0.344  4.326
  65.72  1.420    5.0   ( 3 6 1)   32.86   0.352  4.426
  67.30  1.390    6.0   ( 1 6 3)   33.65   0.360  4.520
  68.60  1.367    3.0   ( 4 2 0)   34.30   0.366  4.597
  69.07  1.359    5.0   ( 1 10 1)  34.53   0.368  4.624
  70.34  1.337    4.0   ( 0 0 4)   35.17   0.374  4.698
  71.31  1.321   12.0   ( 2 8 2)   35.65   0.378  4.755
```

Table D.7: XRD Peaks for Gypsum ($CaSO_4.2H_2O$)

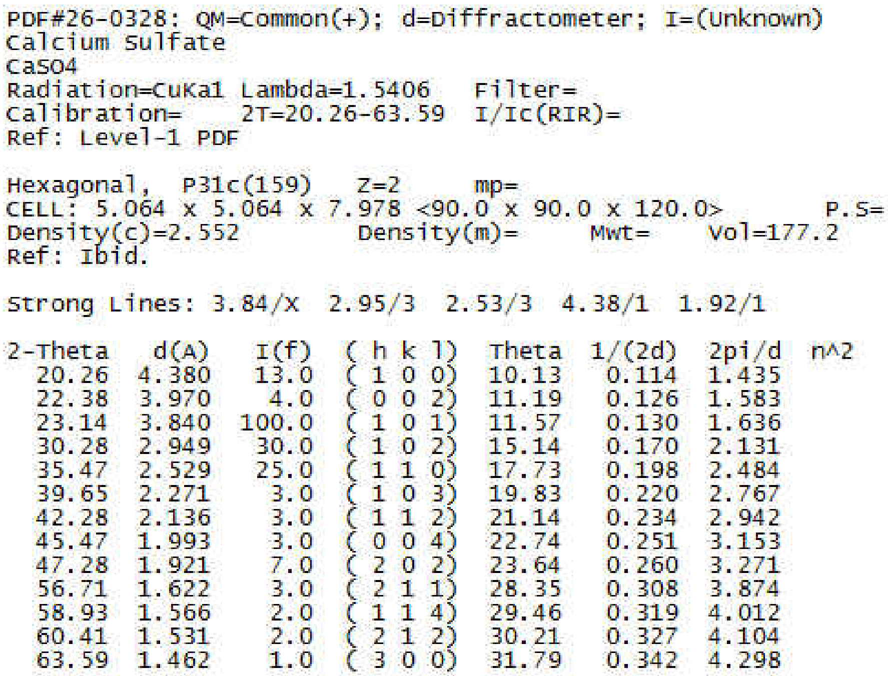

```
PDF#26-0328: QM=Common(+); d=Diffractometer; I=(Unknown)
Calcium Sulfate
CaSO4
Radiation=CuKa1 Lambda=1.5406   Filter=
Calibration=    2T=20.26-63.59  I/Ic(RIR)=
Ref: Level-1 PDF

Hexagonal,  P31c(159)   Z=2      mp=
CELL: 5.064 x 5.064 x 7.978 <90.0 x 90.0 x 120.0>       P.S=
Density(c)=2.552        Density(m)=     Mwt=    Vol=177.2
Ref: Ibid.

Strong Lines: 3.84/X  2.95/3  2.53/3  4.38/1  1.92/1

2-Theta   d(A)    I(f)  ( h k l)  Theta  1/(2d)  2pi/d  n^2
  20.26  4.380   13.0  ( 1 0 0)  10.13   0.114  1.435
  22.38  3.970    4.0  ( 0 0 2)  11.19   0.126  1.583
  23.14  3.840  100.0  ( 1 0 1)  11.57   0.130  1.636
  30.28  2.949   30.0  ( 1 0 2)  15.14   0.170  2.131
  35.47  2.529   25.0  ( 1 1 0)  17.73   0.198  2.484
  39.65  2.271    3.0  ( 1 0 3)  19.83   0.220  2.767
  42.28  2.136    3.0  ( 1 1 2)  21.14   0.234  2.942
  45.47  1.993    3.0  ( 0 0 4)  22.74   0.251  3.153
  47.28  1.921    7.0  ( 2 0 2)  23.64   0.260  3.271
  56.71  1.622    3.0  ( 2 1 1)  28.35   0.308  3.874
  58.93  1.566    2.0  ( 1 1 4)  29.46   0.319  4.012
  60.41  1.531    2.0  ( 2 1 2)  30.21   0.327  4.104
  63.59  1.462    1.0  ( 3 0 0)  31.79   0.342  4.298
```

REFERENCES

Abbaschian, R., Abbaschian, L. & Reed-Hill, R. E. (2008). "*Physical Metallurgy Principles",* USA.

Antao, S. M., Duane, M. J. & Hassan, I. (2002). "DTA, TG, AND XRD STUDIES OF STURMANITE AND ETTRINGITE". *The Canadian Mineralogist,* 40 (5)**,** pp. 1403-1409.

ASTM C78, (2015), "Standard Test Method for Flexural Strength of Concrete (Using Simple Beam with Third-Point Loading)".

ASTM C109, (2013). "Standard Test Method for Compressive Strength of Hydraulic Cement Mortars (Using 2-in. or [50-mm] Cube Specimens)".

ASTM C192, (2015), Standard Practice for Making and Curing Concrete Test Specimens in the Laboratory.

ASTM C305 (2013), Standard Practice for Mechanical Mixing of Hydraulic Cement Pastes and Mortars of Plastic Consistency.

ASTM 1365 (2011), Standard Test Method for Determination of the Proportion of Phases in Portland Cement and Portland-Cement Clinker Using X-Ray Powder Diffraction Analysis.

Babak, F., Abolfazl, H., Alimorad, R. & Parviz, G. (2014). "Preparation and Mechanical Properties of Graphene Oxide: Cement Nanocomposites". *The Scientific World Journal,* 2014 1-10.

Banthia, N. & Nandakumar, N. (2003). "Crack growth resistance of hybrid fiber reinforced cement composites". *Cement and Concrete Composites,* 25 (1)**,** pp. 3-9.

Banthia, N. & Sheng, J. (1996). "Fracture toughness of micro-fiber reinforced cement composites". *Cement and Concrete Composites,* 18 (4)**,** pp. 251-269.

Bell, D. & Garratt-Reed, A. (2003). "*Energy Dispersive X-ray Microanalysis in the Electron Microscope",* Oxford, UK, BIOS Scientific Publishers Ltd.

Bensted, J. & P.Barnes (2002). "*Structure and Performance of Cements",* London, SPON Press.

Bishnoi, S. (2013). "Geometric limitations of nucleation and growth models: Revisiting the impingement assumption". *Cement and Concrete Research,* 46 (0)**,** pp. 30-40.

Bonaccorsi, E., Merlino, S. & Kampf, A. R. (2005). "The Crystal Structure of Tobermorite 14 Å (Plombierite), a C–S–H Phase". *Journal of the American Ceramic Society,* 88 (3)**,** pp. 505-512.

Brunauer, S. (1962). "TOBERMORITE GEL—THE HEART OF CONCRETE". *American Scientist,* 50 (1)**,** pp. 210-229.

Bullard, J. W. (2008). "A Determination of Hydration Mechanisms for Tricalcium Silicate Using a Kinetic Cellular Automaton Model". *Journal of the American Ceramic Society,* 91 (7)**,** pp. 2088-2097.

Bullard, J. W., Jennings, H. M., Livingston, R. A., Nonat, A., Scherer, G. W., Schweitzer, J. S., Scrivener, K. L. & Thomas, J. J. (2011). "Mechanisms of cement hydration". *Cement and Concrete Research,* 41 (12)**,** pp. 1208-1223.

Callister, W. D. & Rethwisch, D. G. (2013). "*Materials Science and Engineering: An Introduction",* USA, Wiley, John & Sons.

Cao, M., Zhang, C. & Wei, J. (2013). "Microscopic reinforcement for cement based composite materials". *Construction and Building Materials,* 40 (0)**,** pp. 14-25.

Chandler, H. W., Macphee, D. E., Atkinson, I., Henderson, R. J. & Merchant, I. J. (2000). "Enhancing the mechanical behaviour of cement based materials". *Journal of the European Ceramic Society,* 20 (8)**,** pp. 1129-1133.

Chandler, M., Peters, J. & Pelessone, D. (2010). "Modeling Nanoindentation of Calcium Silicate Hydrate". *Transportation Research Record: Journal of the Transportation Research Board,* 2142 (1)**,** pp. 67-74.

Chen, J. J., Thomas, J. J., Taylor, H. F. W. & Jennings, H. M. (2004). "Solubility and structure of calcium silicate hydrate". *Cement and Concrete Research,* 34 (9)**,** pp. 1499-1519.

Chung, D. D. L. (2002). "Electrical Conduction Behavior of Cement-Matrix Composites". *Journal of Materials Engineering and Performance,* 11 194-204.

Chung, D. D. L. (2004). "Electrically conductive cement-based materials". *Advances in Cement Research,* 16 (4)**,** pp. 167-176.

Compton, O. C. & Nguyen, S. T. (2010). "Graphene Oxide, Highly Reduced Graphene Oxide, and Graphene: Versatile Building Blocks for Carbon-Based Materials". *Small,* 6 (6)**,** pp. 711-723.

Cong, X. & Kirkpatrick, R. J. (1996). "29Si MAS NMR study of the structure of calcium silicate hydrate". *Advanced Cement Based Materials,* 3 (3–4)**,** pp. 144-156.

Cullity, B. D. (1956). "*Elements Of X Ray Diffraction",* Reading, Massachusettes, Addison-Wesley Publishing Company, Inc.

Dai, Y. & Post, J. E. (1995). "Crystal structure of hillebrandite; a natural analogue of calcium silicate hydrate (CSH) phases in Portland cement". *American Mineralogist,* 80 (7-8)**,** pp. 841-844.

Dreyer, D. R., Park, S., Bielawski, C. W. & Ruoff, R. S. (2010). "The chemistry of graphene oxide". *Chemical Society Reviews,* 39 (1), pp. 228-240.

Faucon, P., Delaye, J. M., Virlet, J., Jacquinot, J. F. & Adenot, F. (1997). "Study of the structural properties of the C-S-H(I) BY molecular dynamics simulation". *Cement and Concrete Research,* 27 (10), pp. 1581-1590.

Forati, T., Atai, M., Rashidi, A. M., Imani, M. & Behnamghader, A. (2014). "Physical and mechanical properties of graphene oxide/polyethersulfone nanocomposites". *Polymers for Advanced Technologies,* 25 (3), pp. 322-328.

Goldstein, J., Newbury, D. E., Joy, D. C., Lyman, C. E., Echlin, P., Lifshin, E., Sawyer, L. & Michael, J. R. (2007). "*Scanning Electron Microscopy and X-ray Microanalysis",* Springer Science.

Hamid, S. A. (1981). "The crystal structure of the 11Å natural tobermorite Ca2.25[Si3O7.5(OH)1.5] · 1H2O". *Zeitschrift für Kristallographie - Crystalline Materials,* 154 (3-4), pp. 189–198.

Han, B., Yu, X. & Kwon, E. (2009). "A self-sensing carbon nanotube/cement composite for traffic monitoring". *Nanotechnology,* 20 (44), pp. 445-501.

Horszczaruk, E., Mijowska, E., Kalenczuk, R. J., Aleksandrzak, M. & Mijowska, S. (2015). "Nanocomposite of cement/graphene oxide – Impact on hydration kinetics and Young's modulus". *Construction and Building Materials,* 78 (0), pp. 234-242.

Hsueh, C.-H. (1991). "Interfacial debonding and fiber pull-out stresses of fiber-reinforced composites Part VI. Interpretation of fiber pull-out curves". *Materials Science and Engineering: A,* 149 (1), pp. 11-18.

Janakiram Subramani, V. 2008. *Atomistic simulations for the prediction of physical properties of cement-based materials.* University of Arkansas.

Jansen, D., Goetz-Neunhoeffer, F., Lothenbach, B. & Neubauer, J. (2012). "The early hydration of Ordinary Portland Cement (OPC): An approach comparing measured heat flow with calculated heat flow from QXRD". *Cement and Concrete Research,* 42 (1), pp. 134-138.

Konsta-Gdoutos, M. S. & Aza, C. A. (2014). "Self sensing carbon nanotube (CNT) and nanofiber (CNF) cementitious composites for real time damage assessment in smart structures". *Cement and Concrete Composites,* 53 (0), pp. 162-169.

Kuila, T., Bose, S., Mishra, A. K., Khanra, P., Kim, N. H. & Lee, J. H. (2012). "Chemical functionalization of graphene and its applications". *Progress in Materials Science,* 57 (7), pp. 1061-1105.

Kumar, A., Bishnoi, S. & Scrivener, K. L. (2012a). "Modelling early age hydration kinetics of alite". *Cement and Concrete Research,* 42 (7), pp. 903-918.

Kumar, M., Singh, S. K. & Singh, N. P. (2012b). "Heat evolution during the hydration of Portland cement in the presence of fly ash, calcium hydroxide and super plasticizer". *Thermochimica Acta,* 548 (0), pp. 27-32.

Land, G. & Stephan, D. (2015). "Controlling cement hydration with nanoparticles". *Cement and Concrete Composites,* 57 (0), pp. 64-67.

Langan, B. W., Weng, K. & Ward, M. A. (2002). "Effect of silica fume and fly ash on heat of hydration of Portland cement". *Cement and Concrete Research,* 32 (7), pp. 1045-1051.

Lawler, J. S., Wilhelm, T., Zampini, D. & Shah, S. P. (2003). "Fracture processes of hybrid fiber-reinforced mortar". *Materials and Structures,* 36 (3), pp. 197-208.

Lerch, W. (1946). "The Influence of Gypsum on the Hydration and Properties of Portland Cement Pastes". *American Society For Testing Materials,* 46 1252-1297.

Li, V. C. & Fischer, G. Reinforced ECC-An evolution from materials to structures. Proceedings of the First FIB Congress, Osaka, Japan, 2002. Citeseer, 105-122.

Li, V. C. & Maalej, M. (1996a). "Toughening in cement based composites. Part I: Cement, mortar, and concrete". *Cement and Concrete Composites,* 18 (4), pp. 223-237.

Li, V. C. & Maalej, M. (1996b). "Toughening in cement based composites. Part II: Fiber reinforced cementitious composites". *Cement and Concrete Composites,* 18 (4), pp. 239-249.

Li, X., Wei, W., Qin, H. & Hang Hu, Y. (2015). "Co-effects of graphene oxide sheets and single wall carbon nanotubes on mechanical properties of cement". *Journal of Physics and Chemistry of Solids,* 85 (0), pp. 39-43.

Lines, M. G. (2008). "Nanomaterials for practical functional uses". *Journal of Alloys and Compounds,* 449 (1–2), pp. 242-245.

Liu, L., Zhang, J., Zhao, J. & Liu, F. (2012). "Mechanical properties of graphene oxides". *Nanoscale,* 4 (19), pp. 5910-5916.

Liu, S., Wang, L., Gao, Y., Yu, B. & Tang, W. (2015). "Influence of fineness on hydration kinetics of supersulfated cement". *Thermochimica Acta,* 605 (0), pp. 37-42.

Livingston, R. A., Schweitzer, J. S., Rolfs, C., Becker, H.-W. & Kubsky, S. (2001). "Characterization of the induction period in tricalcium silicate hydration by nuclear resonance reaction analysis". *Journal of Materials Research,* 16 (03), pp. 687-693.

Lv, S., Liu, J., Sun, T., Ma, Y. & Zhou, Q. (2014). "Effect of GO nanosheets on shapes of cement hydration crystals and their formation process". *Construction and Building Materials,* 64 (0), pp. 231-239.

Lv, S., Ma, Y., Qiu, C., Sun, T., Liu, J. & Zhou, Q. (2013). "Effect of graphene oxide nanosheets of microstructure and mechanical properties of cement composites". *Construction and Building Materials,* 49 (0), pp. 121-127.

Merlino, S., Bonaccorsi, E. & Armbruster, T. (2001). "The real structure of tobermorite 11Å: normal and anomalous forms, OD character and polytypic modifications". *European Journal of Mineral,* 13 (577-590), pp.

Mkhoyan, K. A., Contryman, A. W., Silcox, J., Stewart, D. A., Eda, G., Mattevi, C., Miller, S. & Chhowalla, M. (2009). "Atomic and Electronic Structure of Graphene-Oxide". *Nano Letters,* 9 (3), pp. 1058-1063.

Mohammed, A., Sanjayan, J. G., Duan, W. H. & Nazari, A. (2015). "Incorporating graphene oxide in cement composites: A study of transport properties". *Construction and Building Materials,* 84 (0), pp. 341-347.

Morsy, M. S. (1999). "Effect of temperature on electrical conductivity of blended cement pastes1". *Cement and Concrete Research,* 29 (4), pp. 603-606.

Neville, A. M. (1995). "*Properties of Concrete",* London, Peason.

Neville, A. M. (2011). "*Properties of Concrete"*, Pearson Education Ltd.

Nicoleau, L. (2010). "New Calcium Silicate Hydrate Network". *Transportation Research Record: Journal of the Transportation Research Board,* 2142 (-1), pp. 42-51.

Ostertag, C. P., Yi, C. K. & Vondran, G. (2001). "Tensile strength enhancement in interground fiber cement composites". *Cement and Concrete Composites,* 23 (4–5), pp. 419-425.

Pan, Z., He, L., Qiu, L., Korayem, A. H., Li, G., Zhu, J. W., Collins, F., Li, D., Duan, W. H. & Wang, M. C. (2015). "Mechanical properties and microstructure of a graphene oxide–cement composite". *Cement and Concrete Composites,* 58 (0), pp. 140-147.

Porter, D. A., Easterling, K. E. & Sherif, M. (2009). "*Phase Transformations in Metals and Alloys",* Boca Raton, Florida, USA, CRC Press: Taylor and Francis Group.

Rafiee, M. A., Narayanan, T. N., Hashim, D. P., Sakhavand, N., Shahsavari, R., Vajtai, R. & Ajayan, P. M. (2013a). "Hexagonal Boron Nitride and Graphite Oxide Reinforced Multifunctional Porous Cement Composites". *Advanced Functional Materials,* 23 (45)**,** pp. 5624-5630.

Rafiee, M. A., Narayanan, T. N., Hashim, D. P., Sakhavand, N., Shahsavari, R., Vajtai, R. & Ajayan, P. M. (2013b). "Hexagonal Boron Nitride and Graphite Oxide Reinforced Multifunctional Porous Cement Composites". *Advanced Functional Materials,* n/a-n/a.

Richardson, I. G. (2004). "Tobermorite/jennite- and tobermorite/calcium hydroxide-based models for the structure of C-S-H: applicability to hardened pastes of tricalcium silicate, β-dicalcium silicate, Portland cement, and blends of Portland cement with blast-furnace slag, metakaolin, or silica fume". *Cement and Concrete Research,* 34 (9)**,** pp. 1733-1777.

Richardson, I. G. (2008). "The calcium silicate hydrates". *Cement and Concrete Research,* 38 (2)**,** pp. 137-158.

Salem, T. M. (2002). "Electrical conductivity and rheological properties of ordinary Portland cement–silica fume and calcium hydroxide–silica fume pastes". *Cement and Concrete Research,* 32 (9)**,** pp. 1473-1481.

Scherer, G. W., Zhang, J. & Thomas, J. J. (2012). "Nucleation and growth models for hydration of cement". *Cement and Concrete Research,* 42 (7)**,** pp. 982-993.

Sedaghat, A., Ram, M. K., Zayed, A., Kamal, R. & Shanahan, N. (2014). "Investigation of Physical Properties of Graphene-Cement Composite for Structural Applications". *Open Journal of Composite Materials,* 4 12-21.

Shah, S. P. & Ouyang, C. (1991). "Mechanical Behavior of Fiber-Reinforced Cement-Based Composites". *Journal of the American Ceramic Society,* 74 (11)**,** pp. 2727-2953.

Shahsavari, R., Buehler, M. J., Pellenq, R. J. M. & Ulm, F.-J. (2009). "First-Principles Study of Elastic Constants and Interlayer Interactions of Complex Hydrated Oxides: Case Study of Tobermorite and Jennite". *Journal of the American Ceramic Society,* 92 (10)**,** pp. 2323-2330.

Shahsavari, R., Pellenq, R. J.-M. & Ulm, F.-J. (2011). "Empirical force fields for complex hydrated calcio-silicate layered materials". *Phys. Chem. Chem. Phys,* 13 (1002-1011)**,** pp.

Shannag, M. J., Brincker, R. & Hansen, W. (1997). "Pullout behavior of steel fibers from cement-based composites". *Cement and Concrete Research,* 27 (6)**,** pp. 925-936.

Singh, A. P., Mishra, M., Chandra, A. & Dhawan, S. K. (2011a). "Graphene oxide/ferrofluid/cement composites for electromagnetic interference shielding application". *Nanotechnology,* 22 (46)**,** pp. 1-9.

Singh, V., Joung, D., Zhai, L., Das, S., Khondaker, S. I. & Seal, S. (2011b). "Graphene based materials: Past, present and future". *Progress in Materials Science,* 56 (8)**,** pp. 1178-1271.

Sivakumar, A. & Santhanam, M. (2007). "Mechanical properties of high strength concrete reinforced with metallic and non-metallic fibres". *Cement and Concrete Composites,* 29 (8)**,** pp. 603-608.

Soldano, C., Mahmood, A. & Dujardin, E. (2010). "Production, properties and potential of graphene". *Carbon,* 48 (8), pp. 2127-2150.

Stutzman, P. E. 1996. Guide for X-ray Powder Diffraction Analysis of Portland Cement and Clinker. USA: NISTIR.

Subramani, V. J. (2008). *"Atomistic simulations for the prediction of physical properties of cement-based materials"*, ProQuest LLC.

Suk, J. W., Piner, R. D., An, J. & Ruoff, R. S. (2010). "Mechanical Properties of Monolayer Graphene Oxide". *ACS Nano,* 4 (11), pp. 6557-6564.

Taylor, H. F. W. (1986). "Proposed Structure for Calcium Silicate Hydrate Gel". *Journal of the American Ceramic Society,* 69 (6), pp. 464-467.

Terrones, M., Botello-Méndez, A. R., Campos-Delgado, J., López-Urías, F., Vega-Cantú, Y. I., Rodríguez-Macías, F. J., Elías, A. L., Muñoz-Sandoval, E., Cano-Márquez, A. G., Charlier, J.-C. & Terrones, H. (2010). "Graphene and graphite nanoribbons: Morphology, properties, synthesis, defects and applications". *Nano Today,* 5 (4), pp. 351-372.

Thinh, P. X., Basavajara, C., Kim, J. K. & Huh, D. S. (2012). "Characterization and electrical properties of honeycomb-patterned poly(ε-caprolactone)/reduced graphene oxide composite film". *Polymer Composites,* 33 (12), pp. 2159-2168.

Thomas, J. J. (2007). "A New Approach to Modeling the Nucleation and Growth Kinetics of Tricalcium Silicate Hydration". *Journal of the American Ceramic Society,* 90 (10), pp. 3282-3288.

Thomas, J. J., Jennings, H. M. & Chen, J. J. (2009). "Influence of Nucleation Seeding on the Hydration Mechanisms of Tricalcium Silicate and Cement". *The Journal of Physical Chemistry C,* 113 (11), pp. 4327-4334.

Tilley, R. J. D. (2006). "*Crystals and Crystal Structures"*, Wiley.

Topçu, İ. B., Uygunoğlu, T. & Hocaoğlu, İ. (2012). "Electrical conductivity of setting cement paste with different mineral admixtures". *Construction and Building Materials,* 28 (1), pp. 414-420.

Tosun-Felekoglu, K. & Felekoglu, B. (2013). "Effects of fiber–matrix interaction on multiple cracking performance of polymeric fiber reinforced cementitious composites". *Composites Part B: Engineering,* 52 (0), pp. 62-71.

Tydlitát, V., Matas, T. & Černý, R. (2014). "Effect of w/c and temperature on the early-stage hydration heat development in Portland-limestone cement". *Construction and Building Materials,* 50 (0), pp. 140-147.

Ulm, F.-J., Pellenq, R. J.-M. & Vandamme, M. (2010). "*Computational Modelling of Concrete Structures: Chapter 6: From atoms to concrete structures",* London, Taylor and Francis Group.

Wen, S. & Chung, D. D. L. (2001a). "Cement-based controlled electrical resistivity materials". *Journal of Electronic Materials,* 30 (11), pp. 1448-1451.

Wen, S. & Chung, D. D. L. (2001b). "Effect of carbon fiber grade on the electrical behavior of carbon fiber reinforced cement". *Carbon,* 39 (3), pp. 369-373.

Wu, Z.-Q. & Young, J. F. (1984). "The hydration of tricalcium silicate in the presence of colloidal silica". *Journal of Materials Science,* 19 (11), pp. 3477-3486.

Zeng, Q., Li, K. & Fen-Chong, T. (2015). "Heterogeneous nucleation of ice from supercooled NaCl solution confined in porous cement paste". *Journal of Crystal Growth,* 409 (0), pp. 1-9.

Zhang, L., Wang, Y., Wei, Y., Xu, W., Fang, D., Zhai, L., Lin, K.-C. & An, L. (2008). "A Silicon Carbonitride Ceramic with Anomalously High Piezoresistivity". *Journal of the American Ceramic Society,* 91 (4), pp. 1346-1349.